Burnthrough Modeling of Marine Grade Aluminum Alloy Structural Plates Exposed to Fire

Christian Mark Rippe

Dissertation submitted to the faculty of the Virginia Polytechnic Institute and State University in partial fulfillment of the requirements for the degree of

Doctor of Philosophy
In
Mechanical Engineering

Brian Y. Lattimer
Scott W. Case
Thomas E. Diller
Norman E. Dowling
Robert L. West

September 1, 2015
Blacksburg, VA

Keywords: aluminum, fire, burnthrough, melting, creep rupture, numerical model, finite element, design equations

Burnthrough Modeling of Marine Grade Aluminum Alloy Structural Plates Exposed to Fire

Christian Mark Rippe

Abstract

Current fire induced burnthrough models of aluminum typically rely solely on temperature thresholds and cannot accurately capture either the occurrence or the time to burnthrough. This research experimentally explores the fire induced burnthrough phenomenon of AA6061-T651 plates under multiple sized exposures and introduces a new burnthrough model based on the near melting creep rupture properties of the material.

Fire experiments to induce burnthrough on aluminum plates were conducted using localized exposure from a propane jet burner and broader exposure from a propane sand burner. A material melting mechanism was observed for all localized exposures while a material rupture mechanism was observed for horizontally oriented plates exposed to the broader heat flux. Numerical burnthrough models were developed for each of the observed burnthrough mechanisms. Material melting was captured using a temperature threshold model of 633°C. Material rupture was captured using a Larson-Miller based creep rupture model.

To implement the material rupture model, a characterization of the creep rupture properties was conducted at temperatures between 500 and 590°C. The Larson-Miller curve was subsequently developed to capture rupture behavior. Additionally, the secondary and tertiary creep behavior of the material was modeled using a modified Kachanov-Rabotnov creep model. Thermal finite element model accuracy was increased by adapting a methodology for using infrared thermography to measure spatially and temporally varying full-field heat flux maps. Once validated and implemented, thermal models of the aluminum burnthrough experiments were accurate to 20°C in the transient and 10°C in the steady state regions.

Using thermo-mechanical finite element analyses, the burnthrough models were benchmarked against experimental data. Utilizing the melting and rupture mechanism models, burnthrough occurrence was accurately modeled for over 90% of experiments and modeled burnthrough times were within 20% for the melting mechanism and 50% for the rupture mechanism. Simplified burnthrough equations were also developed to facilitate the use of the burnthrough models in a design setting. Equations were benchmarked against models of flat and stiffened plates and the

burnthrough experiments. Melting mechanism burnthrough time results were within 25% of benchmark values suggesting accurate capture of the mechanism. Rupture mechanism burnthrough results were within 60% of benchmark values.

Dedication

For my wife, Renee. You have been solid ground to support me support me while I reach for my dreams and you have continuously helped me bear the weight of my academic pursuits.

Acknowledgements

There are so many people without whom I would never have been able to realize this dream:

Dr. Brian Lattimer, for the countless hours spent advising and mentoring me that have shaped me into the engineer I am today. I am immeasurably grateful for your investment into my life and engineering career.

Dr. Scott Case, for the invaluable knowledge that helped guide my research.

Drs. Diller, Dowling, and West, for their time and knowledge during my academic pursuits.

The EXTREME Lab members who have provided hours of both quantifiable assistance in running experiments and models as well as discussions that stimulate ideas and approaches I would not have conceived on my own (and occasionally remained on topic).

The staff of the Mechanical Engineering Department for all of the logistical assistance that made so much of this research possible.

The Office of Naval Research and the Naval Engineering Education Consortium for sponsoring this research.

Table of Contents

List of Figures

List of Tables

Nomenclature

Variable	Description	Units
A_1	Hyperbolic-Sine steady state creep model power law multiplier	s^{-1}
A_2	Hyperbolic-Sine steady state creep model hyperbolic law multiplier	Mpa^{-1}
A_s	Plate exposed surface area	m^2
B_1	Kachanov damage model power law multiplier	- -
C_1	Larson-Miller parameter fitting equation multiplier	- -
C_2	Larson-Miller parameter fitting equation constant	- -
C	Material constant used with the Larson-Miller Parameter	- -
C_{LC}	Lateral conduction modifier for design rules steady state temperature calculation	- -
c_p	Material specific heat capacity	J/(kg-K)
$c_{p,AA}$	Material specific heat capacity of aluminum alloy 6061	J/(kg-K)
$c_{p,SS}$	Material specific heat capacity of stainless steel 304	J/(kg-K)
D_1	Normalization constant for creep relaxation initiation design rule	MPa
d	Shortest plate span	m
E	Material elastic modulus	MPa
F	Fire heat release rate	kW
f	Burnthrough site life fraction	- -
G	Representative power law multiplier for creep above 500°C	$s^{-1}MPa^{-h}$
g	Acceleration due to gravity	m/s^2
H	Calibration parameter for stress relaxation design rule prediction at burnthrough site	
h	Representative power law exponent for creep above 500°C	- -
h_b	Convective heat transfer coefficient on unexposed surface of plate exposed to fire	$W/m(m^2-K)$
h_{eff}	Effective convective heat transfer coefficient including linearized radiation boundary condition	$W/m(m^2-K)$
h_f	Convective heat transfer coefficient on exposed surface of plate exposed to fire	$W/m(m^2-K)$
k	Material thermal conductivity	W/(m-K)
k_{AA}	Material thermal conductivity of aluminum alloy 6061	W/(m-K)
k_{SS}	Material thermal conductivity of stainless steel 304	W/(m-K)
L	Plate charactaristic length	m
L	Tensile specimen current unit length	m
L_f	Charactaristic flame length	m
L_i	Tensile specimen intial unit length	m
LMP	Larson-Miller Parameter for calculation of creep rupture time	- -
m	Larson-Miller parameter fitting equation exponent	- -
Nu	Nusselt number	- -
n	Hyperbolic-Sine steady state creep model exponential constant	- -
Pr	Prandlt number	- -

p	Rabotnov creep model damage parameter exponent	- -
Q	Creep activation energy	J/mol
Q_0	Exposure energy absorbed by a standard temperature surface exposed to fire	W
Q_{cond}	Total lateral conduction energy into discrete element	W
Q_{exp}	Total exposure energy into discrete element	W
Q_{rad}	Total radiative energy absorbed by discrete element from fire	W
q_0	Standard surface heat flux into surface exposed to fire	W/m^2
q_{CL}	Centerline heat flux	W/m^2
q_{peak}	Maximum heat flux into surface exposed to fire	W/m^2
q_t	Minimum detectable temporal heat flux fluctuation	$W/(m^2\text{-}s)$
q_{Delta}	Minimum detectable spatial heat flux fluctuation	$W/(m^2\text{-}m)$
R	Universal Gas Constant	J/(mol-K)
Ra	Rayleigh number	- -
r_q	Exposure Radius	m
S	Parameter error coefficient (note: variable units depends on respective parameter)	dependent
T	Current temperature state	K
T_0	Standard surface temperature	K
T_{gas}	Hot gas temperature at surface exposed to fire	K
T_i	Temperature of discretized element at current timestep	K
T_{i-1}	Temperature of discretized element at previous timestep	K
T_M	Material melting temperature	K
T_{NETD}	Noise equivalent temperature differential of infrared camera at measurement temperature	K
T_{SS}	Burnthrough site steady state temperature	K
T_{unif}	Instantaneous burnthrough site temperature of plate under uniform exposure	K
$T_{x,y}$	Instantaneous temperature of discretized element	K
$T_{x,y-\Delta}$ $T_{x,y+\Delta}$ $T_{x-\Delta,y}$ $T_{x+\Delta,y}$	Instantaneous temperature of surrounding discretized elements	K
T_∞	Ambient temperature	K
t	Current time	s
t_r	Creep rupture time	s
t_{relax}	Time to creep relaxation initiation for constant heat flux exposure	s
V	Volume of spacially discretezed element	m^3
z	Vertical distance above burner	m

Greek Letters

Variable	Description	Units
α	Plate span aspect ratio (shorter side to long side)	- -
β	Volumetric thermal expansion coefficient	K^{-1}
Δ	Spatial discretization length	m
δ	Plate thickness	m
η	Kachanov damage model damage parameter exponent	- -
ϵ	Parameter error estimation (note: variable unit depends on respective parameter)	dependent
ε	Current creep strain	- -
$\dot{\varepsilon}$	Instantaneous creep strain rate	s^{-1}
$\dot{\varepsilon}_{II}$	Steady state creep stratin rate	s^{-1}
ε_b	Surface emissivity of plate unexposed surface	- -
ε_f	Surface emissivity of plate exposed surface	- -
ε_r	Creep strain at rupture	- -
ε_{eng}	Engineering strain state	- -
ε_{true}	Cauchy true strain state	- -
λ	Kachanov-Rabotnov creep model rupture strain parameter	- -
ν	Kachanov damage model stress exponent	- -
ν	Material kinematic viscosity	m^2/s
ρ	Material density	kg/m^3
ρ_{AA}	Material density of aluminum alloy 6061	kg/m^3
ρ_{SS}	Material density of stainless steel 304	kg/m^3
σ	Material stress state	MPa
σ_{eng}	Engineering stress state	MPa
σ_i	Burnthrough site initial stress state due to gravitational loads	MPa
σ_{ll}	Larson-Miller parameter fitting equation lower stress limit	MPa
σ_{SB}	Stefan-Boltzmann constant	$W/(m^2K^4)$
σ_{true}	Cauchy true stress state	MPa
σ_{ul}	Larson-Miller parameter fitting equation upper stress limit	MPa
ω	Kachanov material damage parameter	- -

Chapter 1: Introduction

1.1 Research Motivations

Over the past several decades, aluminum alloys have become more frequently used in structural applications where minimizing structure weight is an important design aspect. This includes many sectors of transportation including marine structures where aluminum alloys are replacing traditional steel structures due to their lower density and better corrosion resistance. Today, many marine structures including ships and offshore platforms are constructed with nearly all aluminum as seen in Figure 1.

Figure 1. Modern high speed vessel constructed using aluminum hull and superstructure [73].

Although aluminum alloys offer many advantages over traditional steel, one drawback is aluminum's high temperature properties. Figure 2 contains the temperature dependent elastic modulus and yield strength for typical marine structural steel and aluminum. Each has been normalized to the room temperature value to highlight their temperature dependence. As can be seen, aluminum properties (primarily yield strength) begin to deteriorate at temperatures as low as 200°C and material yield strength has decreased to less than 50% of room temperature values at a temperature of 300°C. In contrast, typical steel materials do not undergo such a decrease until nearly 600°C.

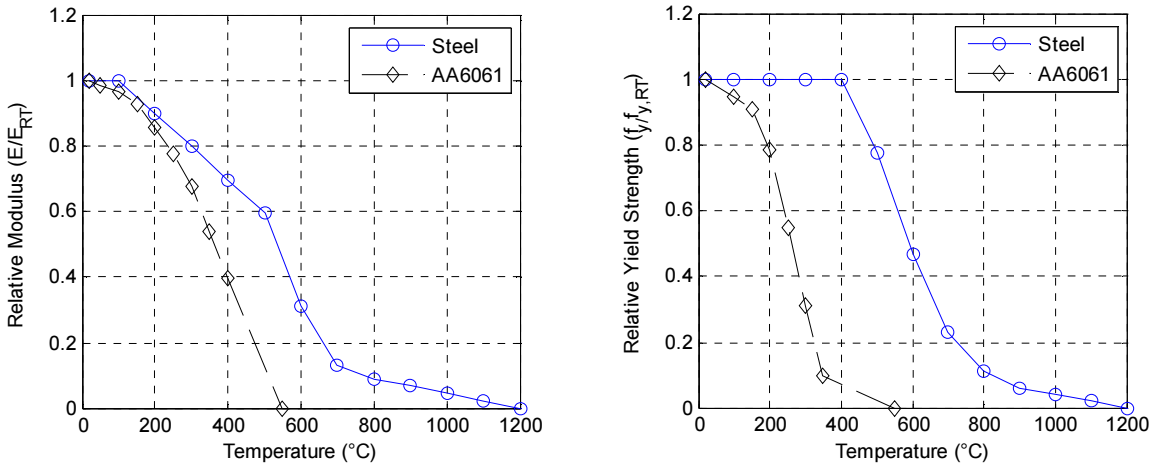

Figure 2. Temperature dependency of material stiffness and material strength for aluminum [34] and steel [74] normalized to room temperature values.

The ramifications of the high temperature performance of aluminum extends beyond a structure's ability to carry necessary loads. This performance also effects a structure's ability to contain localized fires and prevent fire propagation through a structure. One of the primary mechanisms for fire propagation through an aluminum structure is the direct penetration of panels. This is called fire induced burnthrough. Burnthrough occurs both for thicker structural plates as well as thin sheeting used in ventilation systems.

The research presented here explored fire induced burnthrough of aluminum panels. In particular, this research focused on a single alloy: AA6061-T651 plate. AA6061 is a precipitation hardened alloy commonly used in marine applications for its high corrosion resistance and good workability. This research explored fire induced burnthrough via the following tasks which are separated as chapters in this document:

1. Development and performance of experiments for fire induced burnthrough of aluminum panels having a range of thicknesses (ventilation duct to structural plate thicknesses)
2. Development of a high fidelity analytical creep model to predict both burnthrough occurrence and time to burnthrough in finite element simulation
3. Characterization of near melting temperature material properties for use in the burnthrough model

4. Development of a full-field heat flux measurement technique for increased accuracy of thermal models
5. Validation of the analytical burnthrough model against experimental results
6. Development of a simplified burnthrough model for use in performance based design of aluminum structures

1.2 Previous Research

The response of structures in fire has been well researched for several decades. ASTM standard E119 in particular outlines procedures for testing both the thermal and structural response of panels during a standard laboratory exposure [1]. Significant research has been conducted on all scales using this standard [2], [3]. Previous research typically used premixed gas fire furnaces to create uniform thermal exposures over the test specimen. The International Maritime Organization (IMO) has a similar standard for particularly addressing structural stability of fire exposed bulkhead and overhead compartments [4]. While these tests are useful in determining the burnthrough behavior of a specific construction, they do not explore the mechanisms of the burnthrough phenomenon.

Research specifically into burnthrough has generally been limited to experimental observation. This is includes research from many structural engineering sectors including traditional structures where experimental research into burnthrough resistance of metal roofing firewalling has been conducted [5], [6]. However, research in traditional structures generally utilizes traditional steel materials. Research into the burnthrough of aluminum structures is primarily found in the transportation sectors. Johnsson and Yang [7] conducted experiments on burnthrough times of motor coach cabins from exterior fires. Similarly, significant experimental research has been conducted in the aviation industry to investigate fire induced burnthrough of aircraft fuselages. Webster *et al.* [8] as well as Marker and Sarkos [9] conducted full-scale burnthrough tests of a transport category aircraft fuselage. Tran [10] conducted more in depth research on fuselage burnthrough by experimentally evaluating the burnthrough resistance of individual materials used in the structure. Similar research by Hansen and Frame [11] as well as Takahashi *et al.* [2] used fire exposure experiments to investigate the burnthrough characteristics of fire proofing materials. While these experimental observations of burnthrough time are often

useful for evaluating the safety response of these systems, they do not aim to explore burnthrough mechanisms.

While significant experimental research has been conducted in fire induced burnthrough, computational research into development of burnthrough models is nearly non-existent. Current software packages such as the Fire Dynamics Simulator (FDS) that are designed to model fire response only implement a simple temperature threshold model for determination of burnthrough [12], [13]. However, FDS documentation admits that temperature threshold methods are not a good predictor of fire induced burnthrough.

While fire induced burnthrough research is lacking, much of the current research in burnthrough of metals is being conducted by the pipeline industry. Over the past 20 years, welding onto active pipelines has become a common practice both for pipeline repairs and adding pipeline functionality. In pursuit of safe practices, significant experimental and numerical research has been conducted on welding induced burnthrough of pressurized pipelines. Initial work by Bruce *et al.* [14] experimentally investigated welding induced burnthrough of pipelines. Bruce [15] continued this work as well as others to experimentally explore the effects of geometry, loading, and welding parameters on welding induced burnthrough phenomenon [16]. Initial empirical rules were developed by Felix *et al.* [17] based on a temperature threshold model. While temperature threshold models are still common practice in recent research, they are admittedly very inaccurate and generally highly conservative [18]. To further support this, Liu *et al.* [19] numerically explored the effects of pipeline pressure on the thermal response of welded pipelines.

Beyond simple temperature threshold correlations, more complex numerical methods to predict weld induced burnthrough of pipelines has been introduced over the past 15 years. Research by Oddy and McDill [20] began to explore deformation and stress response of welded sections. Sabapathy *et al.* [21] worked on developing deflection based failure criteria for burnthrough using the predicted mechanical response of pipelines under welding conditions. Additionally, strain based models based on the high temperature elasto-plastic rupture strain of pipeline materials were explored by Boring *et. al* [22]. These failure deflection and rupture strain concepts were further explored by Als and Vatani [23] as well as Wahab *et al.* [24] who introduced more geometric, loading, and welding parameters into deflection based failure

models. The strain based failure models developed for pipeline burnthrough consider only the elastic and plastic response of the material as the heating cycle during welding only lasts a few seconds. Because of these short time scales, the effects of creep strains have been neglected in weld induced burnthrough research [22]. Additionally, pipeline burnthrough research has only been conducted on steel alloys commonly used in pipeline construction.

This research will explore the mechanisms of fire induced burnthrough on aluminum plates. The rupture strain based models developed for use in weld induced burnthrough of steel plates will be extended for use in fire induced burnthrough of aluminum plates. Since fire induced burnthrough occurs on a much longer time scales, inclusion of creep strains are used. The development and implementation of these models will require the quantification of the high temperature creep rupture behavior of AA6061 as well as the adaptation of a full-field heat flux mapping methodology for use in thermal finite element models.

Chapter 2: Burnthrough Experiments

A series of burnthrough experiments were conducted to investigate the burnthrough phenomenon and validate burnthrough models. In these experiments, AA6061-T651 plates were exposed to single sided fire exposure. Independent exposure variables that were explored included peak heat flux and exposure diameter. Effects of plate thickness and orientation were also experimentally investigated. The subsequent sections will contain the experimental details and results for burnthrough tests conducted using two different types of experimental setups.

2.1 Experimental setup

2.1.1 Jet Burner experiments

The first type of burner used in burnthrough experiments was a 76 mm diameter propane jet burner. This burner produced a pseudo-premixed high velocity flame to generate stagnation point standard heat fluxes on the order of 100 kW/m^2. The jet burner produced a rapid decline in heat flux with radial distance from the stagnation point and was a typical type of burner used in traditional burnthrough experiments [25]. Figure 3a shows the experimental setup for burnthrough of vertically oriented plates exposed to this burner. In this setup, plates were exposed to fire from the burner on one side while thermo-mechanical measurements were taken from the unexposed

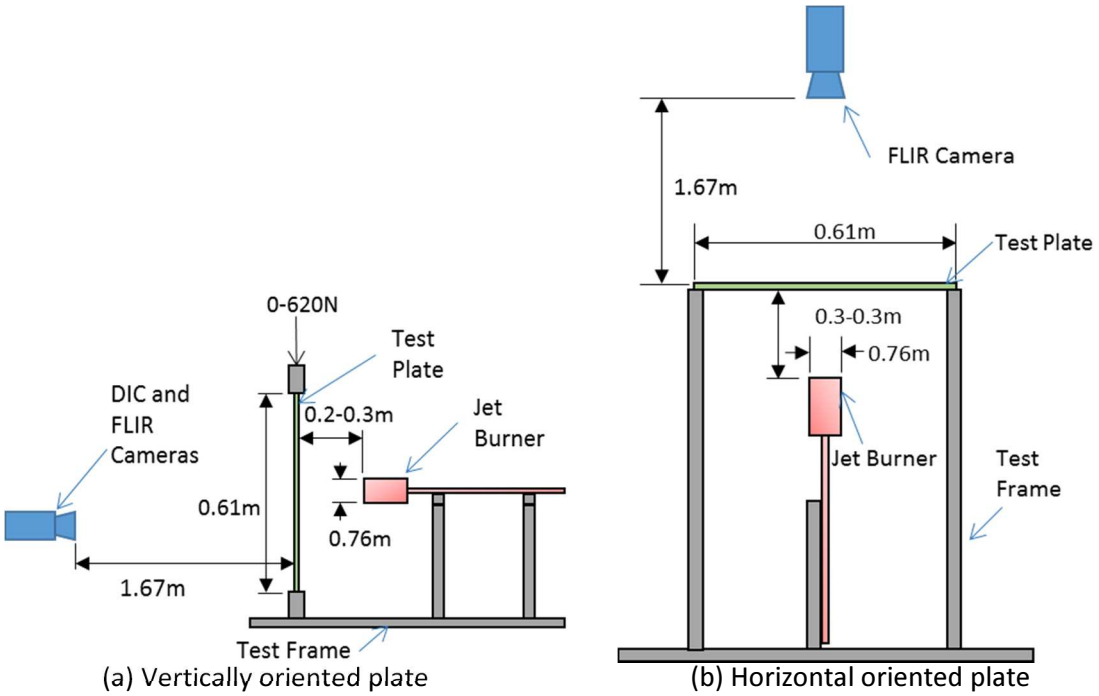

Figure 3. Experimental test apparatuses for burnthrough of vertically and horizontally oriented plates via localized exposure from a propane jet burner.

side. Test plates were simply supported in a pin-pin type configuration at the top and bottom. Support locations at the top and bottom were lined with a pressed ceramic fiber insulation to thermally isolate the test plate from the test frame.

Figure 3b contains the experimental setup for burnthrough of horizontally oriented plates. In this setup, plates were exposed to fire from underneath while thermal measurements were obtained from the top surface. Plates in the horizontal orientation were simply supported along two opposing edges while a single point support was placed in the center of the remaining two edges. Like the vertically oriented plates, plates in this configuration were also thermally isolated from the test frame by supports lined with pressed ceramic fiber insulation.

For all burnthrough experiments, 0.61 m by 0.61 m AA6061-T651 rolled plates with thicknesses ranging from 0.79 to 6.35 mm were used. Plates were coated with several optically thick layers of Rust-Oleum® flat black spray paint on both the exposed and unexposed sides. On the exposed side, the paint provided a high surface absorptivity which maximized the energy flow into the plate. For the unexposed side, the paint provided a suitable surface for full-field thermal measurements of the plate via infrared camera. Additionally, this provided a known surface emissivity for use in analytical models of the experimental exposures. Initial tests of vertical plates exposed to the jet burner were painted using a commercial pneumatic paint sprayer. However, it was found that the paint did not bond well to the test plates at temperatures above 500°C. Upon paint detachment on the unexposed side, thermo-mechanical measurements were lost, as will be discussed in subsequent sections. Remaining tests were painted using commercially available spray cans. This application method was found to have good performance in surface bonding and ductility at temperatures above 500°C.

In the vertical orientation, plates could be structurally loaded with up to 620 N of compressive load. This was achieved via hanging free weight from the top cross-head of the test apparatus. The purpose of applying structural loads to the plates was to determine what effect (if any) this would have on the measured burnthrough time. Structural loads were applied away from the expected burnthrough location to prevent localized fracture of the material due to applied load. Testing was performed with applied structural loads on 1.58 mm and 3.18 mm thick plates. The room temperature Euler buckling capacity was calculated to be 378 N and 3060 N for the 1.58 mm and 3.18 mm plates, respectively. For the 1.58 mm plate, applied compressive structural loads

were limited to 200 N to prevent global buckling failure of the plate at high temperatures. 620 N was the maximum applied compressive load for the 3.18 mm plate as this was the largest load capable of being applied by the test apparatus. Structural loads were not applied to 0.79 mm thick as the room temperature buckling capacity of these plates is only 47 N and the apparatus cross-head weighed approximately 120 N.

A FLIR SC655 IR camera was used with the software package ExaminIR to conduct the thermography of the plate. The SC655 uses uncooled microbolometer type sensors with a wavelength measurement range of 7.5 to 14 μm. Environmental losses between the measurement surface and camera were approximated and accounted for within the ExaminIR software for the given ambient conditions at the time of testing. The pixel resolution of the camera was 640 x 480 pixels which provided a raw spatial resolution of approximately 1.2 mm. Thermographs were generated at frequencies between 0.5 and 5 Hz depending on the expected duration of the particular experiment.

Although the IR camera was factory calibrated for temperatures between 373 and 923 K, an additional calibration of the camera was conducted between 320 and 755 K. In this calibration, a sample of 6.35 mm aluminum plate that was 12.7 mm by 50.8 mm was heated using an Ameritherm 5060LI induction heater. The surface of the sample was painted using the same paint and process as the larger plates. Surface temperature measurements of the plate were obtained via IR thermography as well as a mounted Type-K thermocouple. A comparison of the two measurements provided emissivity of the painted surface. The surface emissivity was found to vary between 0.95 and 0.99 as shown in Figure 4.

In addition to surface emissivity, this calibration was also used to measure the temperature dependent blackbody noise equivalent temperature differential (NETD) of the camera. A detector's NETD is a measure of the signal noise generated by the detector itself and is generally expressed as the temperature required to obtain a signal to noise ratio of one. The NETD of a detector can be experimentally obtained by calculating the standard deviation of the measured spatiotemporal temperature distribution of a uniform temperature object. NETD is proportional to surface temperature so measurements were taken at 298 K and 823 K. A NETD of approximately 0.3 K and 0.05 K was observed at a surface temperatures of 823 K and 298 K, respectively.

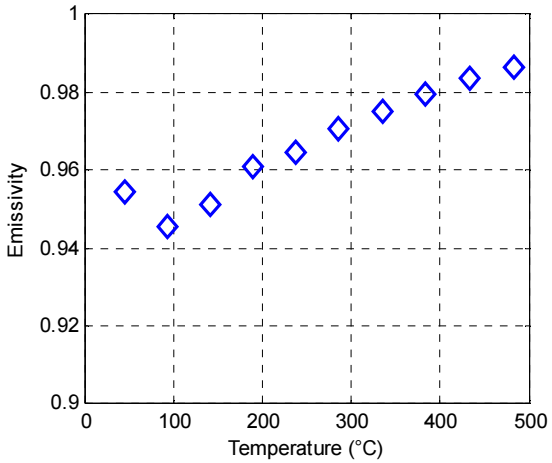

Figure 4. Measured surface emissivity temperature dependence for Rust-Oleum® high temperature flat black paint on AA6061.

For select vertically oriented tests, plate deformations were measured using a commercial three-dimensional digital image correlation (DIC) system from Correlated Solutions. DIC is a full-field deformation measurement technique that uses a stereoscopic pair of cameras to track a randomly seeded speckle pattern on a surface. An overview of DIC measurement techniques has been published by Sutton, *et al.* [26]. The cameras used in these experiments were a pair of 10.6 megapixel CCD digital cameras with a resolution of 4008 by 2642 pixels and images were recorded using Correlated Solutions' commercially available VicSnap software. The system was calibrated by capturing images of a 12x9 predefined grid of circular dots spaced 35 mm apart. The grid was translated and rotated within the camera field of view to obtain corresponding images from each camera. With the known dot pattern and spacing, calibration parameters were calculated within the VicSnap software. For the 0.61 m measurements surfaces used in the experiments, the minimum recommended speckle size (based on 4 pixel width) was 0.9 mm. A sample speckle pattern is shown in Figure 5 to have speckles between 1 mm and 6 mm. DIC images were taken at rates from 0.2 Hz to 5 Hz depending on the expected time to burnthrough.

For tests where DIC was implemented, the DIC system was coupled to the IR camera to obtain thermal measurements corresponding to displacement measurements. To do this, the DIC cameras and IR camera were triggered to simultaneously record images. Calibration of the coupled system was conducted using an anodized aluminum plate where the anodized material was removed to match the grid pattern used in the DIC calibration. Once the plate was heated, the difference in surface emissivity between the anodized and non-anodized surfaces provided measured thermal

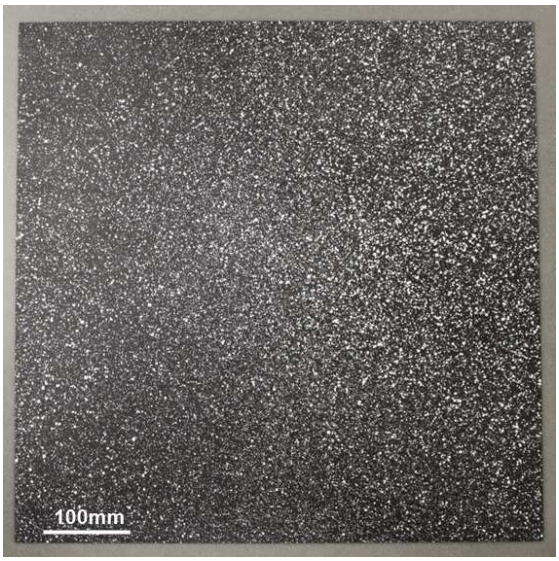

Figure 5. Example of randomly seeded contrasting speckle pattern used for DIC measurement of plates exposed to jet burner.

contrast for the IR camera. The visual contrast between the two surfaces simultaneously provided viable images for the DIC cameras. By capturing simultaneous images from all three cameras (2 DIC cameras and 1 IR camera), plate temperatures from the IR camera could be applied to deflection maps generated from the DIC cameras. The coupled analysis was performed using Correlated Solutions 3-D DIC analysis software Vic3D 7. DIC could not be utilized on horizontally oriented plates because of space constraints caused by the ventilation system above the samples in the test apparatus.

In addition to IR and DIC cameras, both the exposed and unexposed sides of the plate were monitored with standard 30 fps video cameras. These cameras were used to identify time to burnthrough and identify any anomalies that occurred over the duration of the experiments.

For all tests, propane flow into the burner was measured and controlled using an Alicat MC-100 mass flow controller controlled through a LabView interface. Fire exposures were varied either by adjusting the distance between the burner and the test plate or adjusting the heat release rate (HRR) of the flame via the propane flow rate. The flow controller has an accuracy of 0.20 standard liters per minute (slpm) which corresponds to HRR accuracy of 0.29 kW. Most tests conducted with the jet burner utilized a HRR of 20 kW. For these tests, burner distances of 152 mm to 305 mm were used to adjust the peak heat flux and radial heat flux attenuation. A HRR of 30 kW was used for thicker plates to achieve burnthrough. Tests using a HRR of 30 kW were only conducted at a burner distance of 152 mm.

2.1.2 Sand burner experiments

The second type of burner used in the burnthrough tests was a 305 mm by 305 mm square propane sand burner. The sand burner produces a buoyancy driven diffusion flame with stagnation point standard heat fluxes on the order of 60 kW/m^2. Unlike the jet burner, fires from the sand burner in the configuration shown in Figure 6 do not generate steep radial thermal gradients and heat a much larger area of the plate. Figure 6a includes the experimental apparatus for burnthrough of vertically oriented plates exposed to the propane sand burner. In this setup, plates were supported on screw tips at the bottom and top of the plate. This minimized the contact area between the plate and the test apparatus and thus produced thermal isolation of the test plate. A 0.61 m by 1.22 m ceramic fiber insulation board was placed just above the test sample flush with the exposed surface. This was needed because the flame heights in the experiments were significantly larger than the test plate heights and the surface provided proper fire dynamics for flames against a vertical surface. Because the sand burner produces lower peak heat fluxes, a second vertical surface made of ceramic fiber board was placed on the opposite side of the burner from the aluminum test plate. Once heated by the burner, this second surface provided additional radiative heat flux on the test plate to achieve burnthrough. Like the jet burner tests, IR thermography was conducted on the unexposed surface to measure plate temperature.

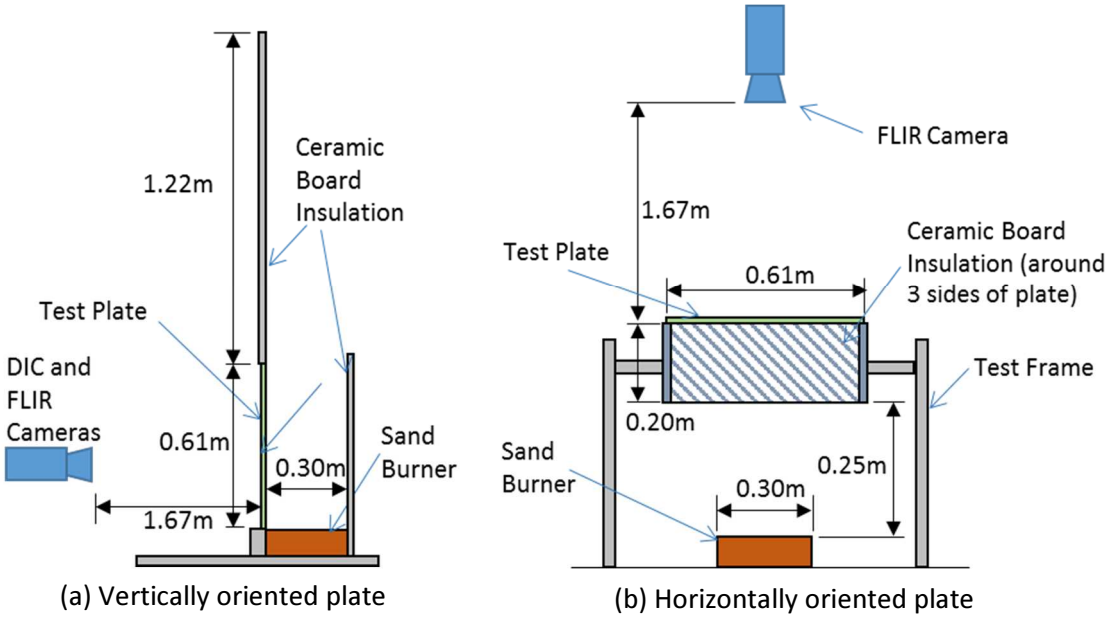

Figure 6. Test apparatuses for burnthrough of vertically and horizontally oriented plates exposed to sand burner.

Burnthrough tests were also performed on horizontally oriented plates exposed to the sand burner. In this test apparatus shown in Figure 6b, plates were exposed to the burner from underneath while thermography measurements were taken from the top of the plate. For this orientation, plates were supported on screw tips along the perimeter of the plate with a 102 mm spacing. 254 mm deep walls were place along three sides of the plate to maximize the heat flux into the test plate similar to the second wall on the vertical plate apparatus.

Just as for the jet burner tests, aluminum test plates exposed to the sand burner were made of 0.61 m by 0.61 m plate with thicknesses ranging from 0.79 mm to 6.35 mm. The exposed side of the plates were painted with the same Rust-Oleum® high-temperature high-emissivity spray paint to maximize the energy absorbed by the plate. For initial tests, the unexposed side of the test plates was painted in the same manner as the exposed side, but burnthrough could not be achieved with the sand burner. Data from these tests is still reported as they provide exposure scenarios in which burnthrough does not occur. In subsequent testing, the unexposed side of the plate was left primarily unpainted. This was done because the high emissivity of the paint generated too high of thermal losses from the unexposed side. Since unpainted aluminum has a surface emissivity of approximately 0.3, leaving the unexposed side of the plates unpainted decreased the radiative losses by approximately a factor of three. To obtain temperature measurements, nine 51 mm by 51 mm squares were painted in a grid pattern on the unexposed side. These painted sections were large enough to obtain accurate temperature measurements via IR thermography, but small enough to minimize the additional radiative losses. Additionally, because the unexposed side could not be painted, coupled DIC measurements could not be obtained for tests utilizing the sand burner.

For the sand burner tests, fire exposures were varied by changing the HRR of the fire. All vertically oriented plate tests were conducted at a fire size of 70 kW. Horizontally oriented plate tests were conducted at fire sizes ranging from 50 kW to 100 kW. The same Alicat mass flow controller implemented with the jet burner was also used for control and measurement of HRR for the sand burner.

2.2 Burnthrough Experiment Results

2.2.1 Jet burner experiment results

Observed time to burnthrough for vertically oriented plates exposed to the propane jet burner are seen in Table 1. These burnthrough times were obtained from visual video of the exposed and

Table 1. Experimentally measured burnthrough times for vertically oriented plates exposed to propane jet burner.

Thickness (mm)	HRR (kW)	Burner Distance (m)	Applied Load (N)	Burnthrough Time (s)
0.79	20	0.30	0	75
0.79	20	0.25	0	70
0.79	20	0.25	0	50
0.79	20	0.20	0	39
0.79	20	0.20	0	48
1.58	20	0.25	0	157
1.58	20	0.25	0	135
1.58	20	0.25	250	141
1.58	20	0.20	0	116
3.18	20	0.25	0	NA
3.18	20	0.20	0	NA
3.18	20	0.15	0	NA
3.18	30	0.15	0	238
3.18	30	0.15	500	235

unexposed surfaces. All of the burnthrough temperatures observed for vertically oriented plates exposed to the propane jet burner were within 625°C and 650°C. As expected, for any specific exposure, burnthrough times for thicker plates are longer than those for thinner plates. Burnthrough times are also directly proportional to the separation between the burner and the test plate due to the reduction in peak heat flux from the flame. Lastly, the presence of any applied structural load to the plate does not have any effect on the resultant burnthrough time.

Figure 7 contains a typical burnthrough surface for vertical plates exposed to the jet burner. For these tests, burnthrough appears to be initiated via melting of plate in the vicinity of the maximum

(a) Unexposed surface (a) Exposed surface

Figure 7. Burnthrough site for unexposed and exposed surface of vertically oriented plate following exposure to jet burner.

exposure. Molten material flows to the base of the exposure area where it solidifies leaving behind a thin layer of aluminum alloy that is bonded to the paint. Burnthrough of the plate was considered to be initiated when the molten material flowed away from the exposure center as any remaining material was only being held by the paint used on the plate's surfaces. For several tests, the paint on the unexposed surface (surface painted with contrasting random speckle pattern) detached from the plate prior to burnthrough as can be seen in Figure 7. This resulted in a loss of thermal and DIC measurements in the vicinity of burnthrough at this point in the test. Temperature measurements at the burnthrough location are seen in Figure 8 for all vertically oriented plate exposed to the jet burner. It is noted on the figure that for several tests, paint detachment occurred between 450°C and 500°C. Because of this, burnthrough initiation temperatures at the burnthrough site could not be obtained for these tests. However, the transient thermal results up to paint detachment were still used for thermal model validation as discussed in Chapter 6.

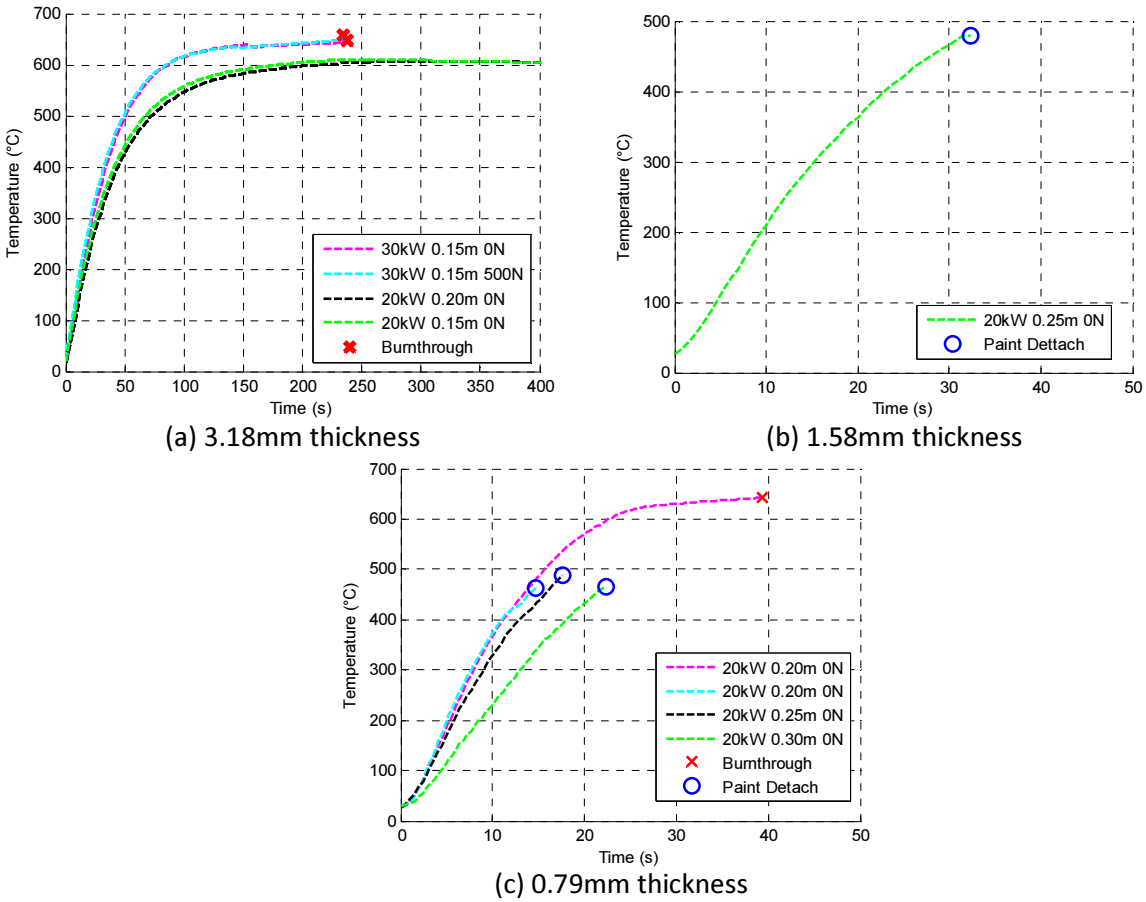

Figure 8. Measured temperature response of burnthrough initiation site for multiple thickness vertically oriented plates exposed to propane jet burner.

The use of the coupled thermal and DIC measurement system allowed for measurement of the time-varying full-field temperature and displacement mapping of select tests. Figure 9 contains these full-field maps for a 3.18 mm plate with no structural load applied just before the onset of burnthrough. Here, the plate globally displaces toward the jet burner. This displacement trend was seen in all tests for this burner and orientation. Additionally, the plate locally displaces away from the burner in the vicinity of the burnthrough initiation site. The temporal progression of the out-of-plane displacement can be seen in Figure 10 for the burnthrough initiation site and a location away from this site. It can be seen that while the plate maintains the trend of displacements towards

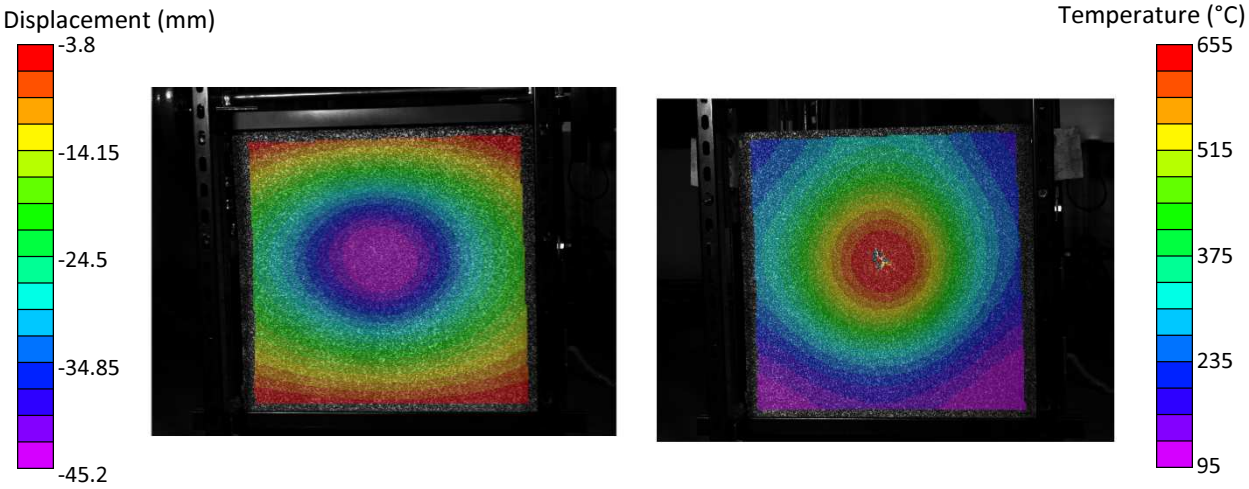

Figure 9. Coupled DIC and IR measurements just prior to burnthrough initiation of vertically oriented 3.18mm plate exposed to jet burner.

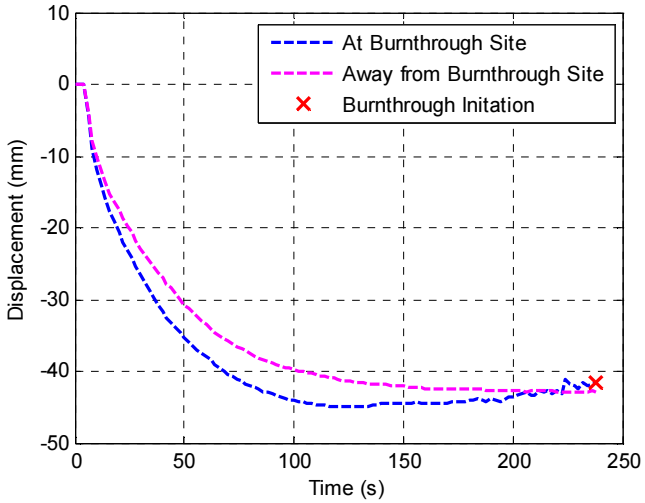

Figure 10. Out of plane displacement of vertically oriented 3.18*mm* thick plate exposed to jet burner at burnthrough initiation site and 150*mm* away from burnthrough site (negative displacement towards burner).

the heater for the duration of test, only the burnthrough initiation site sees a reversal of this trend at the onset of burnthrough. The cause of this reversal is discussed in Section 2.3.

The effect of applied structural load on the displacement response of a 3.18 mm thick plate are seen in Figures 11 and 12. Figure 11 contains out of plane displacement trend for the burnthrough initiation site. It can be seen that the structural load does not have any noticeable effect at the beginning of heating but as the exposure duration increases, the structural load causes an increase in displacement. This increased displacement is global across the entire width of the plate as seen in Figure 12. Here, the displacement gradient between the center and edges of the plate is a result of the thermal strains caused by localized heating while the global displacement is indicative of the onset of plate buckling failure. However, burnthrough was achieved and the experiment terminated before any plates experienced a buckling failure.

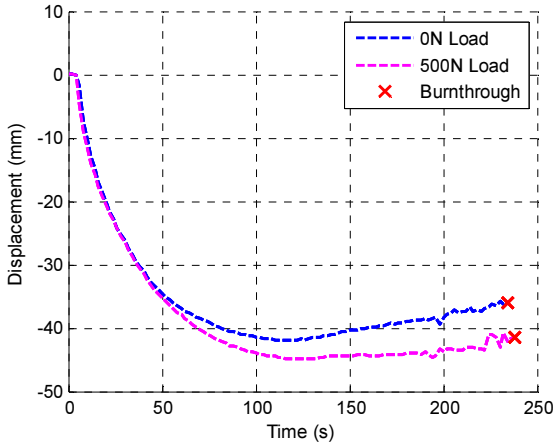

Figure 11. Burnthrough site out of plane deformation for 3.18 mm plate exposed to jet burner with and without applied structural load (negative displacement towards burner).

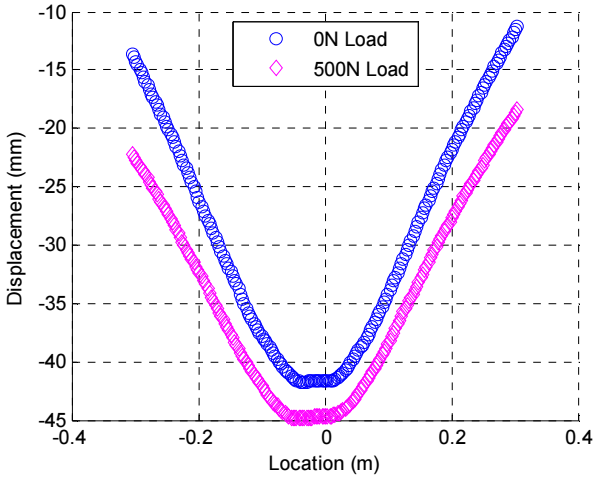

Figure 12. Horizontal centerline displacement profile for vertically oriented 3.18 mm plate exposed to jet burner with and without structural load (negative displacement towards burner).

Burnthrough times for horizontally oriented plates exposed to the propane jet burner are seen in Table 2. The trends are the same as those observed for the vertically oriented plates provided in Table 1. Also, observed burnthrough temperatures were again between 625°C and 650°C. Figure 13 contains images of the burnthrough site for the horizontally oriented plates. Like the vertically oriented plates, burnthrough appeared to occur via a melting mechanism as molten material detached from the horizontally oriented plates. Within the flow impingement area, localized deflections of the plate away from the burner occurred due to the force of the propane jet. Temperature measurements at the burnthrough location for the horizontally oriented plates are seen in Figure 14. Paint detachment did not occur for any of the horizontally oriented plates because the painting method was altered as discussed in the previous section. Temperature measurements are recorded until burnthrough initiation except for the 6.35*mm* plate where burnthrough did not occur.

Table 2. Experimentally measured burnthrough times for horizontally oriented plates exposed to propane jet burner.

Thickness (mm)	HRR (kW)	Burner Distance (m)	Burnthrough Time (s)
0.79	20	0.25	56
0.79	20	0.2	47
1.58	20	0.2	135
1.58	30	0.15	53
3.18	30	0.15	132
6.35	30	0.15	NA

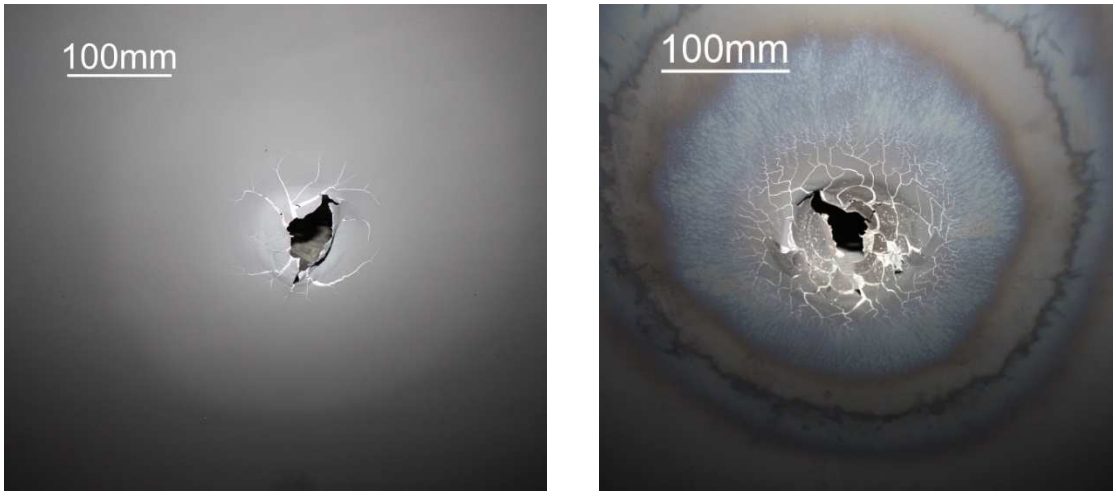

(a) Unexposed surface (b) Exposed surface

Figure 13. Burnthrough site for unexposed and exposed surface of horizontally oriented plate exposed to jet burner.

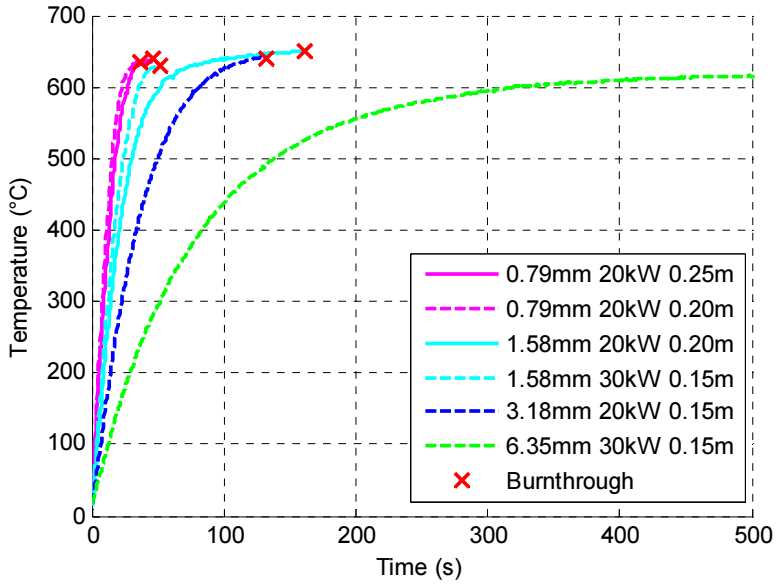

Figure 14. Burnthrough site temperature response for horizontally oriented plates exposed to jet burner.

Measured burnthrough time as a function of burner distance for jet burner exposures is shown in Figure 15 for both plate orientations. For plates exposed to the jet burner, plate orientation does not appear to have any effect as 0.79 mm plate tests have nearly identical burnthrough times. However, thicker plates have variations of burnthrough times that are both longer and shorter for horizontal plates compared to vertical plates.

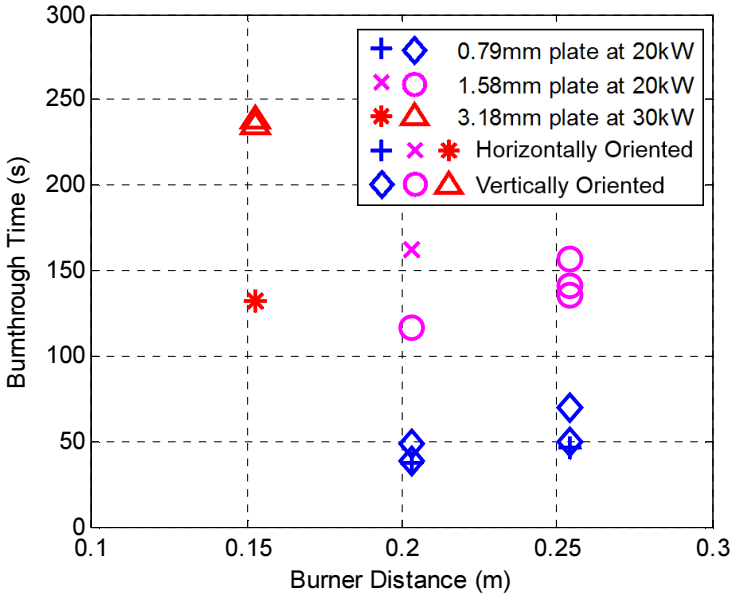

Figure 15. Observed burnthrough times for AA6061 plates exposed to propane jet burner under vertical and horizontal orientations.

2.2.2 Sand burner experiment results

Burnthrough times for both horizontally and vertically oriented plates exposed to the propane sand burner are seen in Table 3. Like the jet burner experiments, these times were obtained from visual inspection of the unexposed surface. Measured plate temperatures of the vertically oriented plate at burnthrough were above 600°C. However, measured burnthrough temperatures of the horizontally oriented plates were between 550°C and 590°C. The visual surface evolution of a vertical plate exposed to a sand burner is shown in Figure 16. For these tests, the burnthrough

Table 3. Experimentally measured burnthrough times for plates exposed to propane sand burner.

Orientation	Thickness (mm)	HRR (kW)	Burnthrough Time (s)
Horizontal	0.79	70	NA*
Horizontal	1.58	40	NA
Horizontal	1.58	50	237
Horizontal	1.58	60	203
Horizontal	1.58	70	198
Horizontal	3.18	50	445
Horizontal	3.18	60	419
Horizontal	3.18	70	439
Horizontal	6.35	100	NA
Horizontal	6.35	120	685
Vertical	0.79	70	285

*Unexposed side of plate painted with high emissivity paint

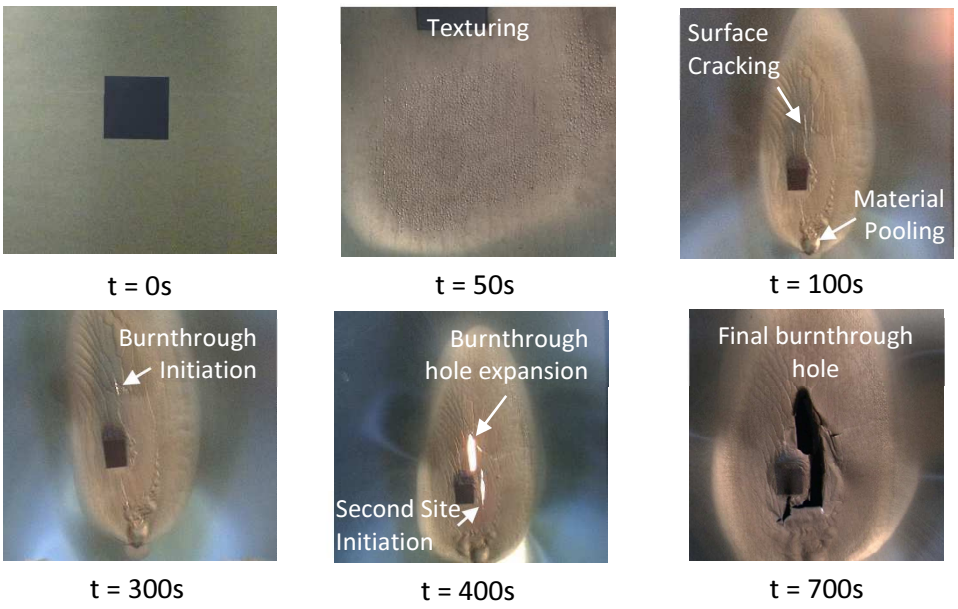

Figure 16. Burnthrough site evolution from unexposed surface of vertically oriented 0.79*mm* thick plate exposed to sand burner.

mechanism appears to initialize with the same melting phenomenon apparent by the pooling of material below the burnthrough site. Physical rupture of the plate occurs much later along the upper edges of the areas affected by melting. However, visual surface damage initiates well before the onset of burnthrough. Because the unexposed side of the burnthrough initiation site could not be painted for these tests, temperature measurement directly at the burnthrough initiation site are not available but were taken in the vicinity at the black patch seen in Figure 16. Temperature measurements in the burnthrough vicinity are shown in Figure 17 for tests where burnthrough was and was not achieved. For the unpainted plate for which burnthrough occurred, material melting occurred at the end of the thermal transient region. However, the edges of the molten region is significantly less defined than in plates exposed to the jet burner. Again, burnthrough in this configuration was considered to occur when molten material flowed away from burnthrough site just as in the jet burner tests.

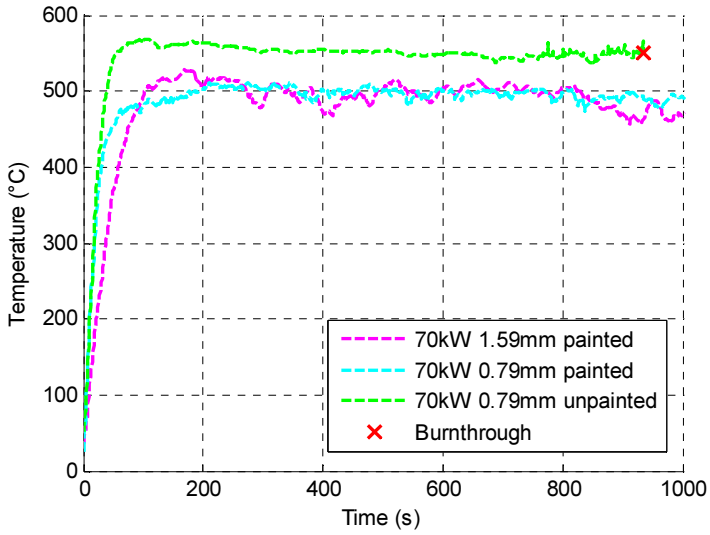

Figure 17. Measured thermal response of vertically oriented plates exposed to propane sand burner. Note: Burnthrough only occurred for exposure of plate with unpainted unexposed surface.

Figure 18 contains the burnthrough site evolution for horizontally oriented plates exposed to the sand burner. Like the vertically oriented plates, the appearance of visual surface damage occurs over 250 s before burnthrough initiation. However, no evidence of molten material was observed for any tests run in this configuration. Temperature measurements in the vicinity of the burnthrough site are shown in Figure 19. Since the unexposed side of the plates could not be fully painted, temperature data at the burnthrough initiation site could not be acquired for most tests. Thus, burnthrough times were recorded for more tests than temperature measurements were acquired.

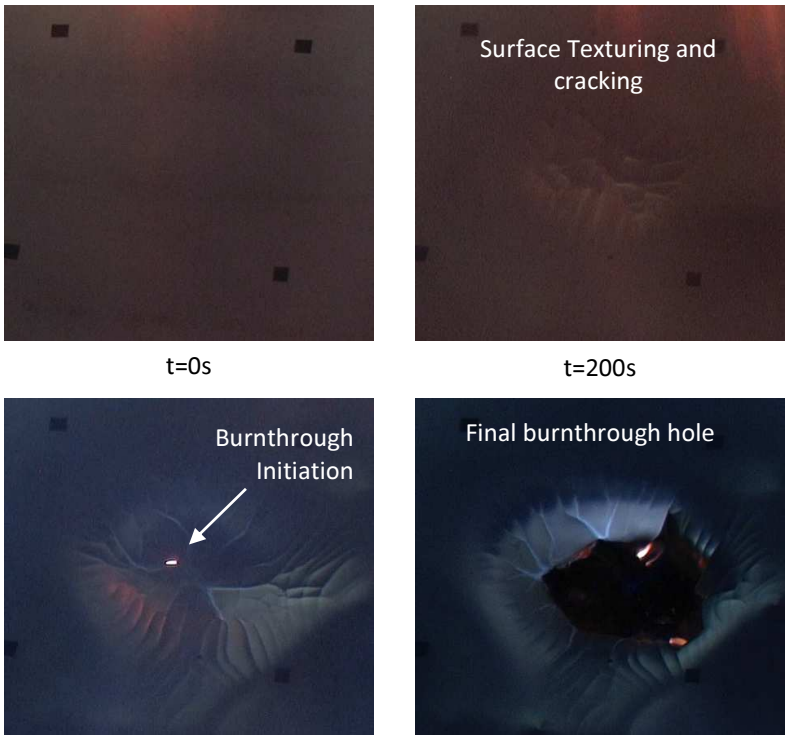

Figure 18. Burnthrough site evolution for horizontally oriented 3.18 mm thick plate exposed to 70 kW fire from sand burner.

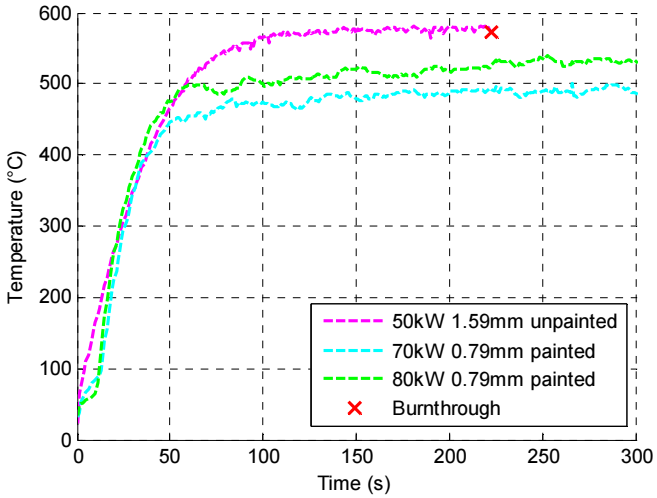

Figure 19. Measured thermal response of horizontally oriented plates exposed to propane sand burner. Note: Temperatures were not measured directly at burnthrough initiation site because flame dynamics prevented accurate predictions of site location.

2.3 Discussion

Based on the burnthrough results from the jet burner tests, it appears that burnthrough times can be related to a plate temperature threshold. For all of these tests, temperature measurements at the

burnthrough initiation site were between 625°C and 650°C. For the jet burner exposures, burnthrough times were not affected by the orientation of the plate. As seen in Tables 1 and 2, burnthrough times for identical plates under identical exposures with different orientations had nearly identical burnthrough times. Additionally, increases in the peak heat flux applied to the plate (via decreasing the separation distance between the plate and burner) caused a reduction in burnthrough time which is expected due to increased energy absorbed by the plates. As the plate thickness is increased, the burnthrough time was increased through two different mechanisms. First, the increased thickness resulted in a directly proportional increase in the thermal mass of plate. This would suggest that burnthrough times would also be directly proportional to plate thickness. Additionally, as plate thickness is increased lateral conduction away from the burnthrough site due to the radial heat flux gradient and subsequent temperature gradient also increased the expected burnthrough time. The combined effects of thermal mass and lateral conduction are seen in Tables 1 and 2 where burnthrough times for the 1.58mm plates are approximately 2.5 times longer than times for the 0.79*mm* plates under identical exposures for both horizontally and vertically oriented plates. All of these effects of orientation, heat flux, and plate thickness on the burnthrough initiation time using the jet burner support a thermally based burnthrough mechanism.

All tests of vertically oriented plates conducted using the jet burner exhibited the same displacement trends. Upon application of heat, plates would displace towards burner. The direction of displacement is due to the slight thermal gradients through the thickness of the plates. Because the exposed side of the plates is at a slightly higher temperature, through thickness thermal expansion gradients cause small bending moments within the plate which, in turn, cause the deflection. However, these thermal gradients are small and do not account for the amount of deflection observed in the tests. Much of the deflection is caused by in-plane thermal gradients within the plate. This is because as the center of the plate is heated, it thermally expands. However, the perimeter of the plate is still relatively cool and constrains the expansion of the plate center. Because of this, the thermal expansion at the plate center generates out of plane deflection as seen in Figure 12.

Another phenomenon observed during the jet burner burnthrough tests, was a reversal of displacement at the flame impingement point just prior to burnthrough initiation. This point also

corresponds to the burnthrough initiation site. This reversal of displacement can been seen in Figure 11 for tests with and without applied structural loading. For both cases, out of plane deflection of the burnthrough initiation site increases towards the burner but eventually reaches a peak. This reversal of deflection is attributed to the force of the impinging flame on the plate in the near zero stiffness region of the material just prior to burnthrough. This reversal trend only occurs within an approximately 25 mm radius of the flame impingement point as this is where material stiffness and flow pressure requirements are adequate. This is seen in Figure 10 where the displacement of a location 150 mm away from the burnthrough initiation continues to increase towards the burner for the entire test duration.

Figures 11 and 12 contains plots of the effects of applied compressive structural load on the mechanical response of the plates. Initial out of plane deflections are approximately equal for exposures with and without structural load. This is expected as the applied load is approximately 20% of the room temperature buckling strength of the plate which causes minimal out of plane deflection. However as the plates begin to undergo thermally induced deflection, the applied structural load begins to affect the out of plane response. This is because as the plate is heated, thermal softening causes a decrease in plate stiffness and buckling strength. Additionally, as out of plane deflections of the burnthrough site increase, the structural load magnifies these displacements due to second order effects. As seen by the burnthrough times in Table 1, applied structural loads have no effect on the burnthrough behavior of plates exposed to the jet burner. This is expected as the burnthrough mechanism for these exposures appear to be strictly thermally driven process.

Observations from the horizontally oriented plates exposed to the sand burner present a different type of behavior. In these tests, no material melting was observed at the burnthrough location. Instead, mechanical damage and fracture appear to occur as seen in Figure 18. Additionally, these failures tended to occur at lower temperatures than observed from the jet burner exposure tests. Figure 20 contains a temperature comparison between a 3.18 mm thick horizontally oriented plate exposed to the jet burner and a 1.58 mm thick horizontally oriented plate exposed to the sand burner. For this case, the observed temperatures from the jet burner exposure exceed those from the sand burner exposure by over 20°C. However, burnthrough of the plate exposed to the sand burner occurs in approximately 300 s while the plate exposed to the jet burner does not burn

through even after 1800 s of exposure. It is this thermal discrepancy that is not captured by traditional temperature threshold models. Additionally, burnthrough initiation of horizontally oriented plates exposed to the sand burner occurred below the material solidus temperature. This suggests a range of burnthrough initiation temperatures that span from 550°C up to 650°C. With this large thermal span, the use of simple temperature threshold criteria can results in predictions that are both unconservative and overly conservative depending on the exact temperature chosen. Also, burnthrough initiation of horizontally oriented plates exposed to the sand burner occurs beyond the establishment of thermal steady state which is a phenomenon that could not be captured by temperature threshold model.

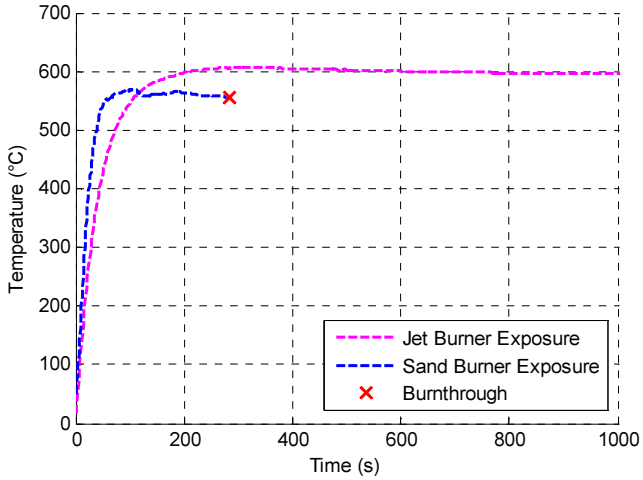

Figure 20. Comparison of thermal response for horizontally plates exposed to jet and sand burner.

2.4 Burnthrough Experiment Conclusions

In this study, a series of burnthrough tests were designed and conducted to experimentally investigate the burnthrough phenomenon in aluminum alloy plates exposed to fire. These experiments consisted of exposures to a propane jet burner which produced localized high heat fluxes and a propane sand burner which produced broader, lower heat fluxes. This study investigated the effects of plate thickness, peak heat flux, and structural load on the occurrence of burnthrough and the burnthrough initiation time. Material melting at the flame stagnation point was experimentally observed to be the primary burnthrough mechanism for localized exposures from the jet burner. This was observed for all plate thickness, plate orientations, and applied structural loads. The melting mechanism appeared to be based solely on the associated thermal process. Because of this, plate orientation and applied structural load did not have any observed

effects on the burnthrough initiation time. Additionally, plate temperatures at burnthrough initiation were observed to be between 625°C and 650°C suggesting that a thermally based model can adequately capture these burnthrough occurrences. This is supported by burnthrough times that are approximately proportional to thermal mass.

Larger diameter exposures from the propane sand burner did not undergo a melting burnthrough but instead exhibited a thermo-mechanical rupture burnthrough mechanism. While the melting mechanism was observed to occur at temperatures above 625°C, observed plate temperatures of horizontally oriented plates exposed to the sand burner were between 560°C and 600°C at the burnthrough initiation site. This suggested a thermo-mechanical burnthrough mechanism that cannot be entirely captured by a solely thermal based model. In the subsequent chapters, the selection and development of numerical models for predicting both the melting and thermo-mechanical rupture burnthrough mechanism is discussed.

Chapter 3: Burnthrough Mechanisms

Experimental observation discussed in the previous chapter led to the inclusion of two different possible burnthrough mechanisms: a material melting mechanism and a thermo-mechanical rupture mechanism. For each of these mechanisms, analysis rules for the onset of burnthrough were developed and implemented into numerical models for predicting both the occurrence of burnthrough and the time to burnthrough.

3.1 Melting Mechanism

The first burnthrough mechanism observed during experiments was a material melting mechanism. This mechanism was apparent for the smaller exposure diameter generated by the propane sand burner for plates in both the horizontal and vertical orientations as well as vertically oriented plates under the larger exposure diameter of the propane sand burner. The phenomenon of aluminum melting under experimentally controlled conditions is well researched between friction stir weld and aluminum melting furnace research [27], [28]. Metallic alloys in general do not have a specific melting temperature as alloying elements within the material causes gradual phase changes over a range of temperatures. For aluminum alloys, the range is generally between a solidus temperature of 580°C and a liquidus temperature of 650°C. Figure 21 contains specific heat capacity measurements for AA6061-T651 generated using differential scanning calorimetry. Here, the phase change between solid and liquid is seen from the large increase in apparent specific heat due

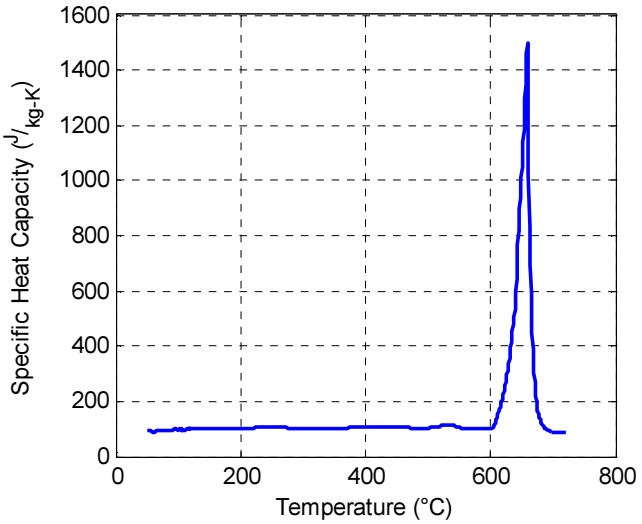

Figure 21. Specific heat capacity of AA6061-T651.

to the latent heat required for the material phase change. For this particular alloy, the solidus and liquidus temperatures were measured to be approximately 600°C and 670°C, respectively.

The specific melting temperature of the material is defined by when the material can no longer hold its original form was measured as 633°C. This number is supported by research conducted by Bowyer *et al.* [29] who found a melting temperature of 640°C for similar test conditions. For numerical models developed in this research a melting temperature of 633°C was used to signal the occurrence of burnthrough by melting. This temperature was assumed to be independent of any mechanical state associated with the burnthrough site. However, research by Bowyer does suggest that the development of an oxide layer on the surface of the aluminum does generate a small mechanical dependency with melting temperatures. These effects have been neglected in this research.

3.2 Thermo-mechanical Rupture Mechanism

The second burnthrough mechanism observed experimentally occurred in horizontally oriented plates exposed to the larger diameter fire of the propane sand burner. This thermo-mechanical rupture mechanism occurred at temperatures below the measured melting temperature and even occurred at temperatures below the measured solidus temperature for this alloy. Additionally, this mechanism was observed within the thermal steady-state region of the material suggesting that it cannot be captured using a solely thermally based mechanism. The thermo-mechanical rupture mechanism was observed to be a function of both exposure time and exposure temperature which lead to the application of a creep based rupture mechanism as seen in Figure 22.

Several different appraches have been developed during the 1950's for modeling the relationships between the creep rupture time, applied stress, and temperature of materials. Larson and Miller [30] developed a material specific relationship to predicting rupture of metallic materials. Similar relationships were also developed by Manson and Haferd [31] as well as Sherby and Dorn [32] using different basic assumptions. In this research the Larson-Miller relationship was used to predict creep rupture. The Larson-Miller relationship involves the calculation of a temperature independent Larson-Miller parameter (LMP). The LMP is derived from the steady state creep rate equation

$$\dot{\varepsilon}_{ss} = f(\sigma)e^{-Q/RT} \tag{1}$$

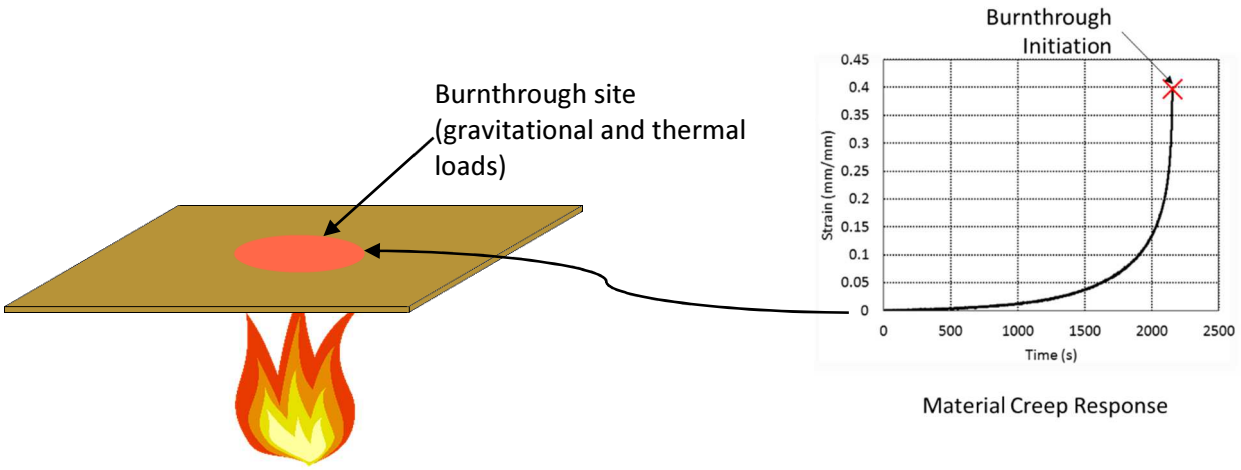

Figure 22. Proposed thermo-mechanical rupture mechanism for horizontally oriented (overhead) plate exposed to fire from underneath.

By integrating Eq. (1), a temperature-compensated time can be calculated as

$$\theta = \frac{\varepsilon_{ss}}{f(\sigma)} = te^{-Q/RT} \tag{2}$$

The LMP is derived from Eq. (2) by evaluating the equation at the rupture point assuming a constant temperature-compensated time at rupture. Applying this, Eq. (2) can be rewritten as

$$LMP = T[log_{10}(t_r) + C]$$

where

$$LMP = Qlog_{10}(e)/R \tag{3}$$

$$C = log_{10}(\theta_r)$$

and T is the test temperature in Kelvin and t_r is the creep rupture time in seconds. Additionally, it is assumed that the LMP is only a function of applied stress state. Using data from a series of uniaxial tensile creep tests, a LMP curve can be generated for AA6061 as discussed in Chapter 4.

One difficulty when working with the Larson-Miller parameter is that the relationship only exists for constant temperature and stress conditions. During a realistic thermal exposure, spatial and temporal temperature gradients within structural plates generate similar spatial and temporal stress gradients. Thus, a method for predicting creep rupture times under varying temperature and stress conditions needs to implemented in conjunction with the traditional Larson-Miller relationship. Here, the Palmgren-Miner damage accumulation model was implemented to monitor the progress

of a particular location to a burnthrough state through the use of a life fraction variable. This approach naturally leads to use in a time-discretized numerical model of the creep rupture mechanism. In this type of analysis, the life fraction evolution is calculated on a discrete time step assuming constant temperature stress conditions as

$$\Delta f = {\Delta t}/{t_r(\sigma, T)} \tag{4}$$

where failure is defined when $f \geq 1$.

To accurately implement the creep rupture based burnthrough model into numerical simulations, accurate predictions of the material's thermal and stress response are needed as well as a characterization of the creep rupture properties at burnthrough conditions. Experimental measurement and numerical modeling of the full creep response of the material under near burnthrough conditions is discussed in Chapter 4. Accuracy of the thermal response at the burnthrough site was increased through the development of an original heat flux mapping methodology along with integration of the methodology into the Abaqus framework.

Chapter 4: High Temperature Creep Behavior

4.1 Introduction and Background

In order to implement the thermo-mechanical rupture burnthrough mechanism, the characterization of the creep behavior of AA6061 is necessary at the temperature and stress levels observed during burnthrough. In particular, measurement of the creep rupture time needs be conducted. Observed thermal measurements from propane sand burner tests suggest this occurs in excess of 550°C as discussed in Chapter 2. Preliminary finite element modeling of the burnthrough phenomenon suggested stress levels at the burnthrough initiation site are below 10 MPa at these temperatures. A more detailed discussion of this evolution is found in Section 6.3.2. The mechanical behavior of AA6061 is not well researched in this temperature and stress range as structural components at these temperature have no significant structural capacity and the microstructural evolution is relatively stagnant.

Creep characterization of AA6061 at lower temperatures and high stresses has been thoroughly researched. Data from Kaufman [33] contains steady state strain rates and rupture times for low temperature creep tests with rupture times ranging from 360 s to 3,600,000 s. This data is for experiments conducted at stresses ranging from 10 MPa to 310 MPa and temperatures from 25°C to 315°C. Allen [34] conducted tensile creep tests of AA6061 at stresses ranging from 12 MPa to 220 MPa and temperatures ranging from 200°C to 400°C. The temperature and stress range that exists during burnthrough is not captured by the data and initial models based on an extrapolation of the higher stress data was highly inaccurate.

At temperatures above 500°C, AA6061 becomes fully recrystallized. Research by Summers [35] found that the recrystallized grain structure of the material was equiaxed with an average grain size of 48 μm. Frost and Ashby [36] generated creep deformation mechanism maps for commercially pure aluminum at average grain sizes of 10 μm and 1000 μm. These maps suggest the same power law creep mechanism is present at the temperature and stress levels tested by Kaufman [33] and Allen [34]. However, at temperatures above 550°C, dynamic recrystallization of the material occurs during creep testing. Additionally at stresses below 10 MPa, lattice diffusion becomes the dominant creep deformation mechanism in aluminum [36]. Because of both of these changes in the creep deformation mechanism, it is expected that an extrapolation of data from

Kaufman [33] and Allen [34] will not accurately capture the creep response at temperature and stress levels seen at burnthrough.

4.2 High Temperature Creep Experiments

4.2.1 Experimental setup

To obtain creep property data in the relevant temperature and stress ranges, a series of uniaxial tensile creep tests were conducted. These tests were conducted in accordance with ASTM standard E139 [37]. These tests were performed at temperatures between 500°C and 580°C and at stresses from 0.5 MPa to 5.0 MPa. Test articles were fabricated from 6.35 mm thick aluminum rolled plate. Rectangular dogbones of 12.7 mm width and 50.8 mm reduced section length were used. One side of the test specimens were coated with several optically thick layers of the Rust-Oleum® high-temperature spray paint discussed in Section 2.1.1 for IR temperature measurement. The opposite side of the test specimen was painted for use with a laser extensometer as discussed below.

A diagram of the experimental test setup is shown in Figure 23. Test specimens were suspended from the cross-head of a servo-hydraulic load frame by a 6.35 mm diameter hole drilled through the upper grip region of the specimens. Specimens were supported in bearing rather than gripped as bearing supports better thermally isolated the specimens. This created less thermal gradient along the length of the specimens. Stresses were applied to the specimens by free hanging weights

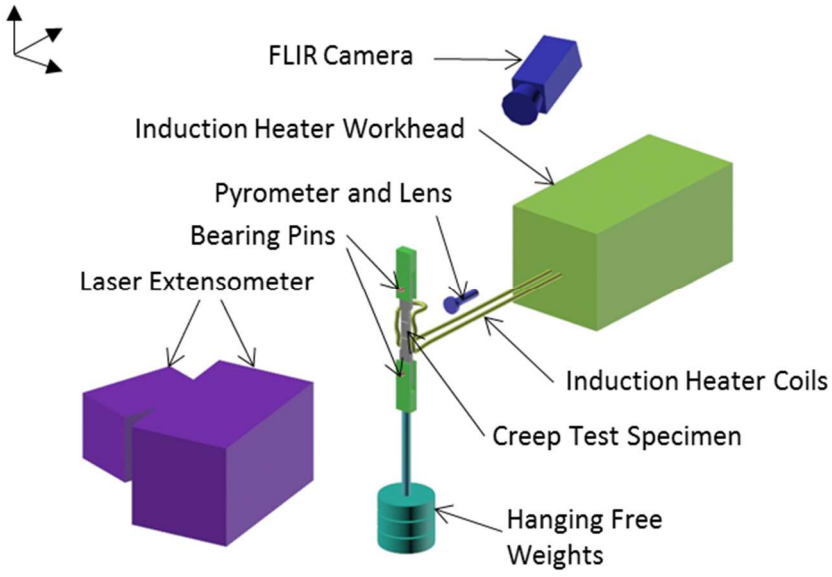

Figure 23. Test apparatus for high temperature creep tests.

attached in bearing via a 6.35 mm diameter through hole in the lower grip region of the sample. Loads between 45 N and 450 N were applied to the samples in 45 N increments. Because of the small loads used in these tests, the use of the servo-hydraulic load frame for applying the loads was not possible as the frame could not accurately maintain such low load levels. Instead, hanging weights were used to apply the load to ensure constant load through the duration of the tests. The lower moveable cross-head of the servo-hydraulic load frame was used to support the weights prior to testing and during sample heating. By lowering the crosshead, this method produced an instantaneous and repeatable application of the applied load.

Creep test specimens were heated using an Ameritherm 5060LI induction heater. Induction heaters provide heat to metallic specimens by running high electrical currents through copper coils near the specimen. The localized magnetic field generated by the current induces electrical currents in the specimen. These currents in the specimen cause ohmic heating of the specimen due to its electrical resistivity. The induction heater was used because it provides visual access to the specimen during testing for IR and laser extensometer measurements. It also provides control over thermal gradients within the sample through the use of proper coil design. The induction heater was controlled using a Micro-Epsilon optical pyrometer with a spectral measurement range of 8-14 μm and a measurement spot diameter of 6mm. The pyrometer was focused to a 1mm spot size on the center of the specimen gauge length using and IR lens. The full-field specimen temperature profile was measured using the same FLIR SC655 IR camera as discussed is Section 2.1.1. A sample measured temperature profile is shown in Figure 24. As can be seen, thermal gradients along the gauge length were within 3°C. For high temperature testing, test specimen were heated to temperatures between 500°C and 585°C at nominal 5°C increments. However, test temperatures used in the creep analysis were derived from test temperature measurements at the rupture site as measured by the IR camera for each test. This provided a higher degree of accuracy in developing the creep strain and rupture models.

Transient creep strains were measured using a Fiedler Optoelekronik laser extensometer. The extensometer has a measurement range of 51 mm with an accuracy of 0.1 mm. Test specimens were painted with perpendicular lines 1.5 mm wide and 25 mm apart for measurement by the extensometer. This allowed for strain measurements up to 100% with an accuracy of 0.4%. Strain

measurements were recorded at a frequency of 5 Hz. Subsequent to testing, strain measurements were passed through a 0.1 Hz discrete Laplace filter to remove any noise from the measurement.

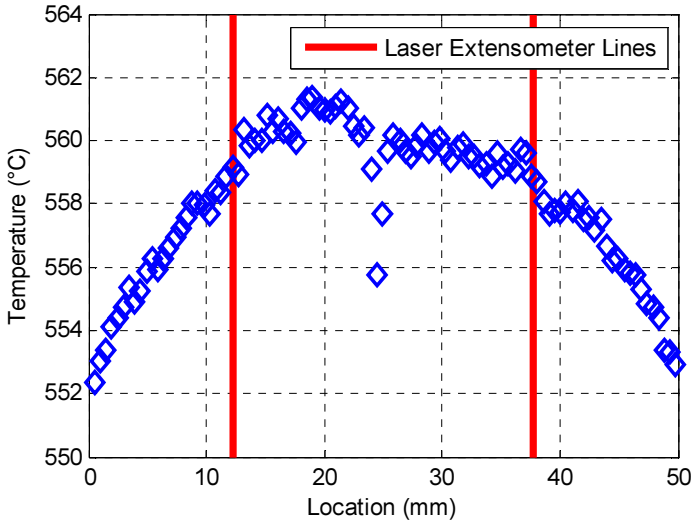

Figure 24. Experimentally measured typical thermal gradient along gauge length of creep specimen for high temperature creep tests.

For all tests, samples were heated at 50°C/m to the test temperature. Temperatures were held for 600 s before loading was applied. Although recommended thermal soak times for creep testing are longer than this, research by Summers [35] suggests that microstructural evolution occurs at temperatures well below 500°C and thus 600 s was deemed sufficient for the material structure to reach an equilibrium state. After the hold period, tensile loads were applied near instantaneously as described above. Strain data recording was initiated prior to specimen heating and continued through to creep rupture.

4.2.2 Experimental creep rupture results

Creep rupture time results from Kaufman [33], Allen [34], and the experiments described in the previous section are seen in Figure 25. Rupture times are shown in the form of the Larson-Miller parameter as calculated by Eq. (3). In order to calculate temperature compensated rupture times from the experimental data, material activation energy is needed. Activation energy was calculated from steady state creep strain rates as discussed in the subsequent sections. Additionally, the value of the constant C is necessary to calculate the LMP from the experimental rupture data. The value of C was calculated for each creep experiment from the high temperature tests and each of the tests conducted by Allen. The average of each experimental value was taken to produce a single number for use in the creep model. This average was calculated to be 13.0 with a standard deviation of

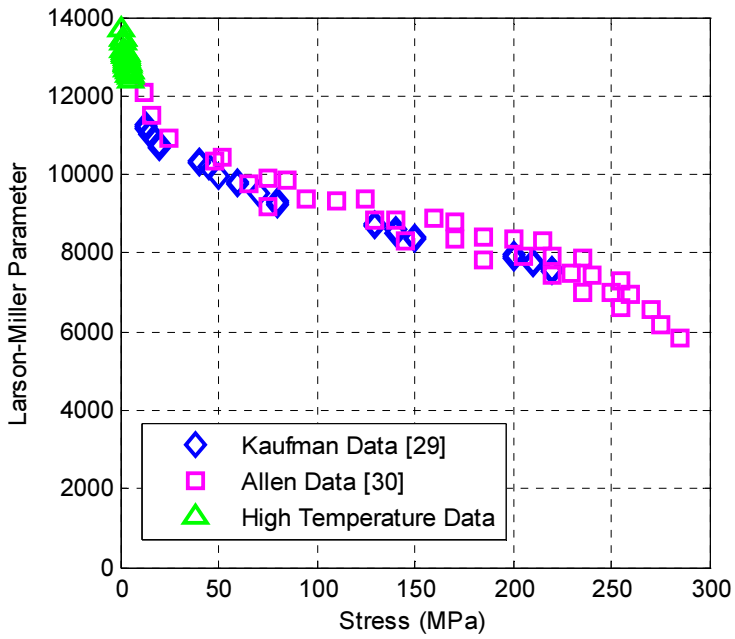

Figure 25. Experimental Larson-Miller Parameter data from multiple sources of previously published literature for AA6061-T651. Experimental temperatures range from 100°C to 400°C.

3.2. Creep rupture data from all three experimental sources converges well in the LMP domain and an expected inverse proportionality was observed between applied stress and LMP. Development of an analytical model for the creep rupture results is discussed in the subsequent section.

4.3 Creep Modeling Approach

The creep response of the material was modeled using a modified Kachanov-Rabotnov creep law. This creep law is applicable to materials that exhibit no primary creep region and is controlled in three parts: the secondary creep rate, the creep rupture strain, and the creep rupture time. The secondary creep rate of each alloy was modeled using a hyperbolic-sine law. This creep rate law takes the form

$$\dot{\varepsilon}_{II} = A_1[sinh(A_2\sigma)]^n e^{-Q/RT} \tag{5}$$

where A_1, A_2, and n are fitting constants, Q is the material activation energy for the appropriate creep mechanism, R is the universal gas constant (8.314 *J/mol-K*), and σ and T are the current stress and temperature state, respectively. A multivariable, non-linear regression was used to calculate the fitting constants and activation energy using all of the experimental creep results.

The tertiary creep behavior of the material was modeled using a Kachanov based damage model. In the traditional form, the Kachanov damage model was included into a creep model by Rabotnov using a power law steady state creep law in conjunction with the multiplicative damage term to capture the unstable tertiary creep range [38], [39]. This Kachanov-Rabotnov (K-R) creep model prescribes the instantaneous creep strain rate as

$$\dot{\varepsilon} = \frac{B_1 \sigma^h}{(1-\omega)^p} \tag{6}$$

where $B_1\sigma^h$ is the power law steady state portion and $(1-\omega)^p$ is the damage term. In this research a modification to the traditional K-R model was made to replace the steady state power law creep with the hyperbolic sine creep model. To apply this modification, the traditional K-R creep model was generalized to include a single secondary creep rate term as

$$\dot{\varepsilon} = \frac{\dot{\varepsilon}_{II}}{(1-\omega)^p} \tag{7}$$

In order to solve Eq. (7) for the instantaneous creep strain, the evolution of the damage parameter ω must be known. This relationship is defined by the second equation in the Kachanov damage model. Here, the rate of change in the damage parameter as

$$\dot{\omega} = \frac{B\sigma^v}{(1-\omega)^\eta} \tag{8}$$

for any given stress level. In order to utilize Eq. (8), an explicit equation for the time evolution of the damage parameter is necessary. Once that is obtained, it can be inserted into Eq. (7) to determine temporal response of the creep strain. Using separation of variables, Eq. (8) can be integrated as

$$\int_0^\omega (1-\omega)^\eta d\omega = \int_0^t B\sigma^v dt \tag{9}$$

to solve for the damage parameter. Solving the definite integral, the damage parameter was calculated to be

$$\omega = 1 - [1-(1+\eta)B\sigma^v t]^{\frac{1}{\eta+1}} \tag{10}$$

The equation can be framed in terms of the rupture time using the known boundary condition that at $t = t_r$, the damager parameter $\omega = 1$. Applying this condition to Eq. (10) yields

$$\omega = 1 - \left(1 - \frac{t}{t_r}\right)^{\frac{1}{\eta+1}} \tag{11}$$

as an explicit form for the damage parameter. Inserting Eq. (11) into Eq. (7) yields a time dependent equation for the instantaneous creep rate as

$$\dot{\varepsilon} = \frac{\dot{\varepsilon}_{II}}{\left(1-\frac{t}{t_r}\right)^{\frac{m}{\eta+1}}} \tag{12}$$

Equation (12) can then be integrated with respect to time using separation of variables to solve for instantaneous creep strains as

$$\varepsilon = \dot{\varepsilon}_{II}\, t_r \lambda \left[1 - \left(1 - \frac{t}{t_r}\right)^{1/\lambda}\right] \qquad \text{where } \lambda = \frac{\eta+1}{-m+\eta+1} \tag{13}$$

where λ is a fitting constant. To determine the value for λ, the known boundary condition of $\varepsilon = \varepsilon_r$ when $t = t_r$ was used. By applying this boundary condition to Eq. (13), an explicit formulation of λ was found to be

$$\lambda = \frac{\varepsilon_r}{\dot{\varepsilon}_{II}\, t_r} \tag{14}$$

Assuming a constant value for λ, this value was calculated for each experiment conducted in this study as well as data from Allen [34]. The average value of λ was found to be 17.7 with a standard deviation of 3.3 for AA6061.

The last parameter necessary for modeling the creep curves using the modified K-R creep model is the creep rupture time. As discussed in Chapter 3, a relationship between the temperature and stress state as well as the creep rupture time can be generated through the use of the LMP. Once the stress dependent LMP is calculated for a given material, the rupture time can be calculated by rearranging Eq. (3) as

$$t_r = 10^{\frac{LMP}{T} - C} \tag{15}$$

for any particular temperature and stress combination. Using the high temperature data from Allen [34], the lower temperature data from Kaufman [33], and the low stress, high temperature data shown in the previous section, a Larson-Miller curve was generated for AA6061. Non-linear regression was used to produce an analytical fit of the data in the form

$$LMP = C_1 \operatorname{atanh}\left[\frac{2}{\sigma_{ul}-\sigma_{ll}}\left(\sigma - \frac{\sigma_{ul}+\sigma_{ll}}{2}\right)\right] + C_2 \tag{16}$$

where C_1, C_2, σ_{ul}, and σ_{ll} are fitting parameters. Finally, by substituting Eq. (16) in for the LMP in Eq. (15) and subsequently substituting Eq. (15) in for t_r in Eq. (13), a final expression for the instantaneous strain at any given time can be written. However, for clarity this explicit equation has not been written out.

4.4 Results and Discussion

4.4.1 Modified Kachanov-Rabotnov Creep Model

The results of the non-linear regression hyperbolic-sine steady state creep rate model according the Eq. (3) are shown in Table 4. A comparison of the experimentally measured secondary creep rates by Allen [34] and the predicted values from the hyperbolic-sine law are shown in Figure 26 for all of the temperature and stress levels tested by Allen. It can be seen that the predicted creep rates match well with the experimental data from Allen. Although not shown, creep rate predictions were also generated for the low stress experiments conducted during this research. The fit generally under-predicted data at these stresses. It is not surprising that a single creep model cannot capture both the high and low stress data as the creep mechanism is different for these two regimes [36]. However, preliminary modeling efforts showed that predicted burnthrough times were insensitive to this difference. Because of this, predictions from the Allen data were used in the burnthrough models. Using the non-linear fit of experimental data from Allen [34], a creep activation energy of 205 kJ/mol was calculated for AA6061-T651. Maljaars *et al.* [40] measured

Table 4. Hyperbolic sine steady state creep rate model parameters.

Parameter	Value
A (s^{-1})	2.91×10^{11}
B (Mpa^{-1})	0.0404
n	1.74
Q (kJ/mol)	204

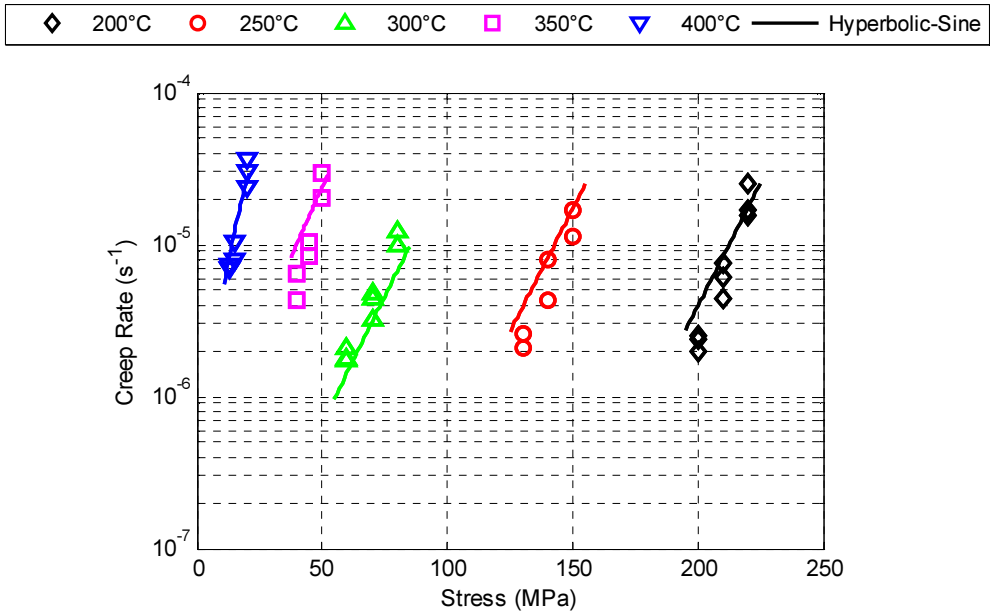

Figure 26. Comparison of steady state creep rates experimentally measured by Allen [34] and calculated from the modified K-R creep model.

the creep activation energy for similar alloy AA6060-T66 in similar stress and temperature states using a stepwise temperature experiment. Maljaars reports the activation energy to be 195 kJ/mol which is within 5% of that calculated during this study. This small difference can be attributed to the similar but different alloy used by Maljaars.

Results from the non-linear regression of the LMP curve according to Eq. (16) are seen in Table 5. Using these parameters, the analytical expression for the LMP is seen in Figure 27 compared to the experimental data from all three sources: Kaufman, Allen, and this research. The analytical fit generally predicts the experimental LMP values within 5%. However, data from this research and from Allen are predicted better than that from Kaufman. This does not present significant effects on this research as the temperature region reported in Kaufman is below 315°C. For burnthrough prediction, the accuracy of the LMP fit below 5 MPa is the most important region. At stresses near 5 MPa, the analytical LMP fit generally under-predicts experimental data by

Table 5. Material Larson-Miller parameter model constants.

Parameter	Value
C_1	-1853
σ_{ul} (Mpa)	298
σ_{ll} (Mpa)	-0.76
C_2	8611

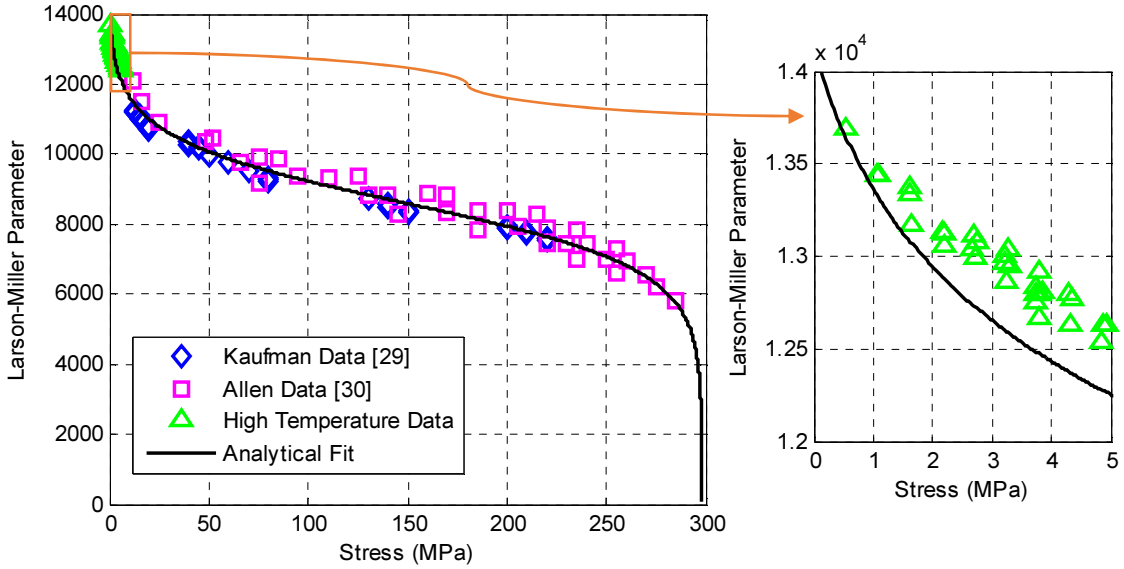

Figure 27. Experimentally calculated Larson-Miller parameter values compared to analytical inverse hyperbolic tangent model up to 300 MPa.

approximately 3%. As stresses are decreased to 1 MPa, this under-prediction drops to less than 1%.

Using Eqs. (13), (15), and (16) predictions of the secondary and tertiary creep response from data collected by Allen were calculated. A comparison between the predicted and experimentally measured creep responses is shown in Figure 28 for creep curves measured by Allen [34]. A comparison of the high temperature data obtained during this research is shown in Figure 29. The modified K-R model successfully captures the general shape of the experimentally observed tertiary region at both the lower and higher temperature regimes. Also, the largest errors are from the rupture time predictions. This error is large because the power relationship between the LMP and the rupture time makes the predictions very sensitive to errors in the LMP prediction. At stresses between 1 MPa and 5 MPa, the K-R model under-predicts rupture time by up to 30%. This is because of the under-prediction of the LMP at these stresses as seen in Figure 27. For this alloy, the prediction of rupture strain is generally higher than experimentally observed. Because of the high degree of ductility in the creep behavior of these alloys, capturing the experimental rupture point can be difficult. This is one of the primary reasons a prediction of rupture time has been implemented to predict the occurrence of burnthrough instead of a prediction of rupture strain.

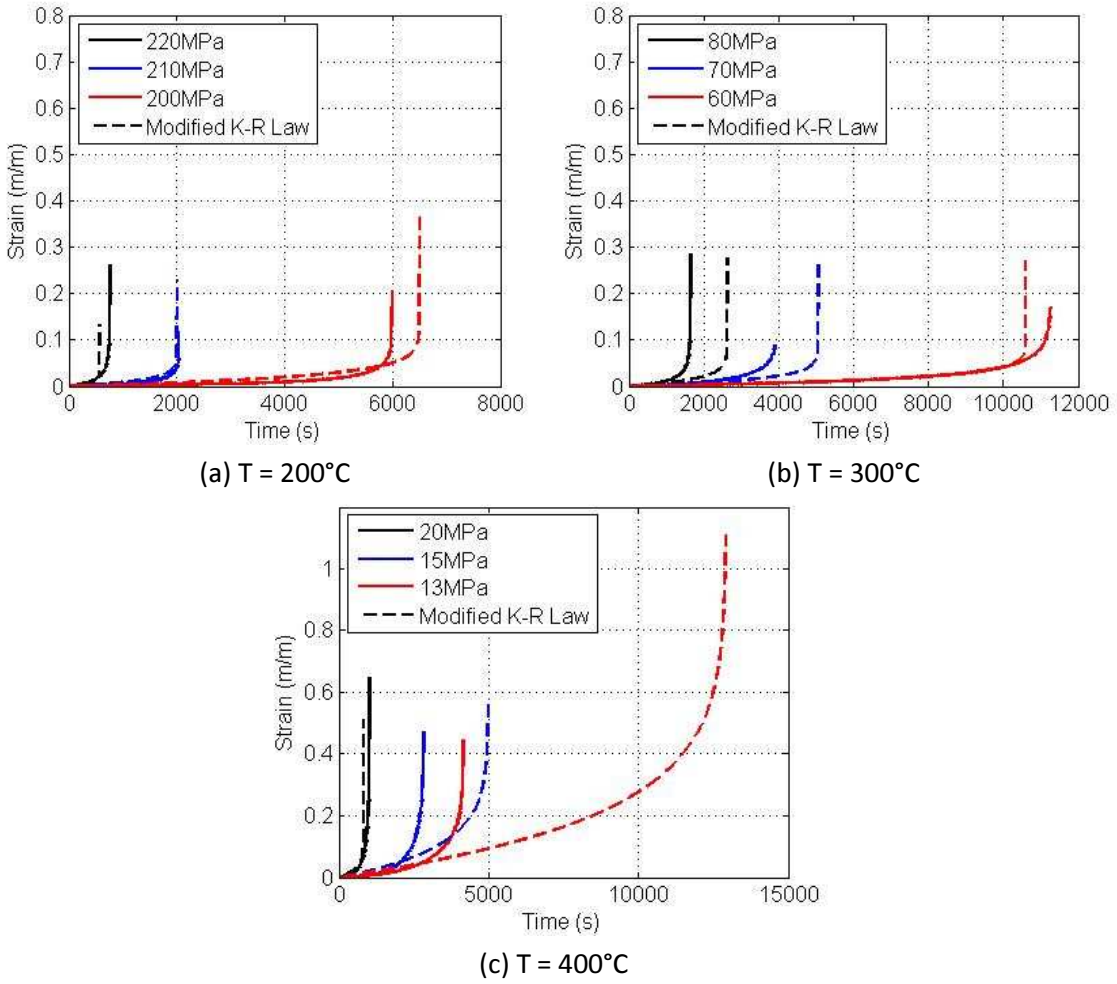

Figure 28. Comparison of experimentally measured creep response at 200°C, 300°C, and 400°C to full creep curves generated using modified K-R creep model.

4.4.2 Abaqus Implementation

The modified K-R creep model was implemented into the Abaqus 6.10ef framework using Microsoft's Visual Studio 2008 and Intel's Professional Visual Fortran Compiler 11. This was achieved via the CREEP user sub-routine. This routine was used to calculate the discrete instantaneous change in creep strain over the duration of the current timestep. By taking the derivative of Eq. (13), and applying the strain rate over a discrete time interval Δt, the instantaneous strain increment is calculated as

$$\Delta\varepsilon = \dot{\varepsilon}_{II}\,\Delta t\left(1 - {}^{t}/_{t_r}\right)^{{}^{1}/_{\lambda^{-1}}} \tag{17}$$

However, the presence of the current time t in Eq. (17) poses a problem because it inherently assumes a constant stress and temperature history. To account for variable stress and temperature

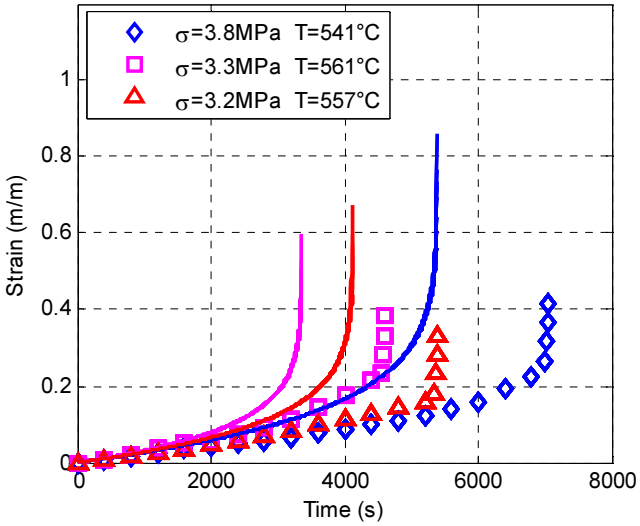

Figure 29. Comparison of experimentally measured creep response and modified K-R creep model at temperatures above 550°C and stresses below 5 Mpa.

conditions, a Miner's rule approach was adopted such that the life fraction at timestep j in the analysis is given by

$$f = \frac{t}{t_r} = \sum_{i=1}^{j} \frac{\Delta t_i}{t_{r,i}} \tag{18}$$

where $t_{r,i}$ is the rupture time associated with the temperature and stress condition applied for a particular timestep. By combining Eq. (17) and (18), an implementable form of the instantaneous creep increment is given by

$$\Delta\varepsilon = \dot{\varepsilon}_{II}\, \Delta t (1-f)^{1/\lambda - 1} \tag{19}$$

for any timestep in the analysis.

Since the creep routine was implemented in an implicit fashion, the derivative of the strain increment with respect to the current amount of strain as well as the derivative with respect to the current stress level are necessary. The stress derivative of the strain increment was calculated as

$$\frac{d\Delta\varepsilon}{d\sigma} = A_1 A_2 \cosh(A_2\sigma)^n e^{(-Q/RT)} \Delta t (1-f)^{1/\lambda - 1} \tag{20}$$

It should be noted that this derivative does not consider a stress dependent rupture time because of the implementation of the life fraction variable. Although the instantaneous creep strain is a

function of stress through the rupture time, the current life fraction of the integration point is only a function of the temperature and stress history. It is not a function of the current temperature and stress state. Thus, the stress derivative of the strain increment is solely the stress derivative of the steady state strain increment magnified due to the current life fraction.

The calculation of the strain derivative was accomplished through the chain rule using the damage parameter as an intermediate variable. Through this method, the strain derivative of the strain increment was calculated to be

$$\frac{d\Delta\varepsilon}{d\varepsilon} = \frac{d\Delta\varepsilon}{d\omega}\frac{d\omega}{d\varepsilon} = \frac{\Delta t}{t_r}\left(1/\lambda - 1\right)(1-f)^{1/\lambda - 2}\left(1 - \frac{\varepsilon}{\lambda t_r \dot{\varepsilon}_{II}}\right)^{\lambda - 1} \tag{21}$$

for any analysis timestep. Using Eq. (19), (20), and (21) Abaqus is able to calculate the discrete creep strain increment for any timestep in an implicit analysis.

4.5 High Temperature Creep Conclusions

A creep characterization of AA6061-T651 was conducted using data found in literature as well as additional creep rupture time data from temperatures above 500°C and stresses below 10 MPa. This characterization was necessary for this research for two reasons: quantification of creep rupture behavior at temperatures observed during burnthrough and accurate prediction of stress response at the burnthrough site. To accomplish this, a series of uniaxial tensile creep tests were conducted at temperatures above 500°C and stresses between 0.5 MPa and 5 MPa. Creep rupture time data from these tests was combined with data from literature at temperatures between 100°C and 400°C and stresses between 12 MPa and 285 MPa. Using this combined data, Larson-Miller parameter values were calculated and an analytical fit was developed for predicting creep rupture times at all temperatures and stresses. The analytical fit was generally able to predict experimental LMP values within 5%. Below 5 MPa, the fit was within 3% of data and continued to converge to less than 3% error at 1 MPa.

To increase the accuracy of the predicted stress response at the burnthrough site, a model of the secondary and tertiary creep response of the material was developed. The model was based on the Kachonov-Rabotnov creep model. The model developed here utilized a hyperbolic-sine secondary creep model along with an Arrhenius kinetics temperature dependency. The tertiary creep effects were included using the Kachanov damage model. The modified K-R creep model was compared

to experimental data obtained by Allen [34]. The general shape of the creep curves was captured well by the creep model. The most significant error in the creep model was the rupture time prediction as it is sensitive to errors in the LMP due to the power law relationship between them.

The modified K-R creep model as then implemented into the Abaqus framework through a user subroutine. To accomplish this, an expression of the instantaneous creep strain increment for any temperature and stress history was developed. Because the existing model was developed for constant stress and temperature, a Palmgren-Miner rule was adopted for use in finite element analyses. Lastly, select derivatives of the creep strain increment expression were calculated to utilize the implicit creep solver within the Abaqus framework.

Chapter 5: Heat Flux Measurement

5.1 Introduction and Background

Initial burnthrough models conducted during this research suggested that both the occurrence of burnthrough and the time to burnthrough are sensitive to the burnthrough site temperature. In order to accurately model the thermal response of the plate, accurate heat flux models of the fire exposures are necessary. Traditional techniques for measuring exposure heat flux on a surface involve mounting an air-purged or water-cooled gauge on or within a surface. Significant research over the past 20 years has introduced several different new types of heat flux sensors that primarily focus on obtaining measurements at places that are not possible with traditional gauges [41]–[44]. Additionally, research into the use of imbedded temperature measurements along with inverse heat transfer analysis to calculate surface heat flux at point locations has also been heavily researched [45]–[49].

The primary difficulty with developing heat flux profiles of the fire exposures in this research is not difficulty in mounting traditional gauges but instead with the high degree of temporal and spatial variation in the surface heat fluxes. Because of this, single point measurements are not sufficient to capture the heat flux profile or predict the plate's thermal response. Traditionally, full-field heat flux measurements would be made using an array of single point measurement sensors [50]–[53]. However, this methodology can be quite expensive from purchasing and maintaining a large number of sensors and it can be very time consuming to setup such an extensive array. Because of these limitations, spatial resolution possible with sensor arrays is quite low (>10 cm). Preferable to this is the use of temperature based heat flux measurements using an inverse heat transfer analysis. Dillon [54] utilized a temperature array based method utilizing thermocouple measurements on a metal plate to develop heat flux profiles. Although not expensive, this method is still quite time consuming and spatial resolutions are still limited to approximately 2.5 cm.

In recent years, infrared (IR) thermography has been introduced as a method for obtaining high spatial resolution, full-field temperature measurements. On a small scale, IR thermography of thin stainless steel foils less than 75 μm thick has been implemented to obtain full-field measurements of local convective heat transfer coefficient [55]–[58], jet impingement fluxes [59], and fluidized bed fluxes [60]. In addition to its ease of implementation the advantage to using IR thermography

at intermediate scales is the ability to obtain spatial resolutions on the order of 1 mm. IR thermography is also a non-intrusive measurement technique so temperature measurements can be obtained without affecting fire performance. One primary disadvantage with IR thermography is the need for a clear view of the measurement surface. However, for the experimental setups described in Chapter 2, that is not a concern.

As part of this research, a method was developed for use of IR thermography to measure full-field transient heat fluxes from fires to nearby surfaces via an inverse heat transfer analysis using the unexposed surface temperature. The method was used to measure heat fluxes into both stainless steel and AA6061-T651 plates. Heat fluxes from the stainless steel plates were validated against data from traditional measurement techniques for exposures from radiant panels as well as horizontally oriented plates exposed to the propane sand burner described in Section 2.1.2. Finally the effects of spatial and temporal resolution on the accuracy of the measurement were also investigated. This allowed for optimal measured heat flux profiles to be utilized in thermal models for predicting burnthrough.

5.2 Experimental Setup

In this research, two sets of experiments were conducted to validate the inverse heat transfer method for measuring full-field heat flux maps. This included tests with a radiant heater exposure onto a vertical plate as well as fires in direct contact with vertical and horizontal plates.

5.2.1 Radiant Panel Tests

The first set of experiments consisted of a 0.97 mm thick vertically oriented stainless steel plate exposed on one side to a radiant heater as shown in Figure 30. Experiments were conducted at heater panel temperatures of 500°C, 600°C and 700°C. The heater panels used in these experiments measured 0.61 m by 0.61 m and had a surface emissivity of approximately 0.7 at the temperatures used in this study. The measurement surface of the plate was 0.61 m by 0.61 m. For all the tests, both sides of the plate were painted with the same high emissivity paint used in the burnthrough experiment. The temperature dependent emissivity of the paint can be found in Section 2.1.1 in Figure 4. Again, this was done to allow for higher accuracy in quantifying the emissivity of the plate surfaces. For the exposed surface, this also maximized the amount of energy absorbed by the plate from the fire. For the unexposed surface, this provided a suitable surface for

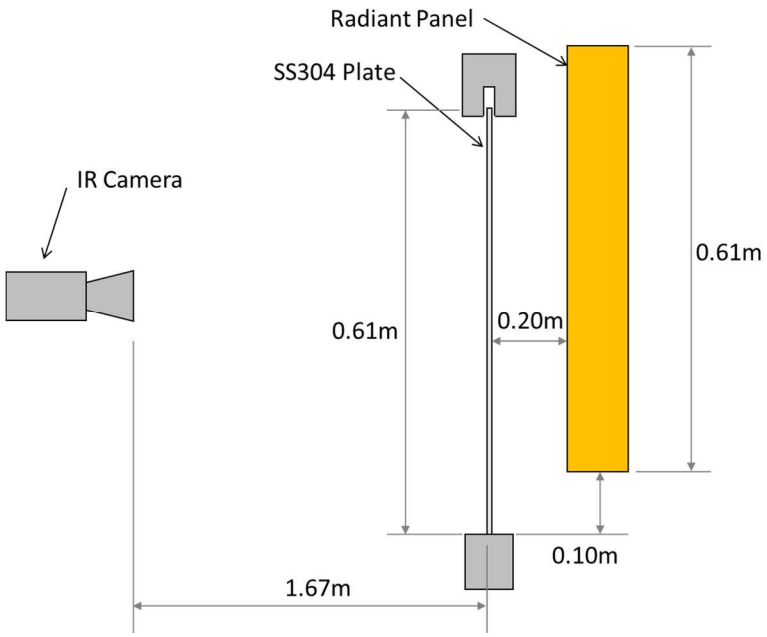

Figure 30. Single sided radiant heater panel exposure of SS304 plate with IR thermography measurement of unexposed surface.

the IR thermography measurements. The stainless steel plate was exposed to the heater panels long enough for steady state conditions to occur.

The same FLIR SC655 IR camera was used with the software package ExaminIR to conduct the thermography of the plate. The camera was calibrated for use between 373 K and 923 K with an NETD of 0.05 K at 298 K. Because the plates used in the heat flux mapping were of the same size as those used in the burnthrough tests, this provided a raw spatial resolution of approximately 1.2 mm (1.4 mm^2). An IR measurement frequency of 5 Hz was used for all test conducted using the radiant heater. Prior to the measurement, the camera was focused onto the measurement surface to ensure high quality images. The thermographs were also filtered using a double pass Wiener filter prior to the inverse analysis. The use of filters on the measured thermographs is further discussed in Section5.5. IR measurements were taken for 30 s prior to exposure to measure ambient temperatures and continued through cooling of the plate after the exposure.

To validate the exposure fluxes from the inverse method, separate tests were conducted using a water-cooled Schmidt-Boelter heat flux gauge (HFG) to measure the standard heat flux. The HFG was mounted into a 3.18 mm thick AA6061-T651 plate so that the measurement surface was flush with the exposed side of the plate. HFG tests were run separately from the inverse method tests because the presence of the cooled HFG would introduce an unquantified energy sink into the plate

which cannot easily be accounted for in the inverse analysis. Heat flux measurements were taken at the plate center for tests conducted with the radiant heater panels. These heat flux measurements were then compared to the standard heat flux measurements obtained using IR thermography with the SS304 plate. The gauge used was a Medtherm GTW-7-32-485A water cooled gauge calibrated between 0 kW/m^2 and 35 kW/m^2. HFG data was recorded using a National Instruments cDaQ-9174 with a NI-9205 16bit voltage card. This supplied a heat flux resolution of 0.002 kW/m^2. The measurements were taken at a rate of 500 Hz and filtered to 5 Hz to eliminate electrical interference. For all tests, Schmidt-Boelter gauge data was collected for 300 s of exposure.

5.2.2 Fire Tests

The second series of experiments consisted of a test plate with one surface exposed to a fire from the propane sand burner using the nearly identical experimental apparatuses as used in the burnthrough tests. Heat flux mapping tests were conducted on both horizontally and vertically oriented plates. The exact experimental test setup for horizontally oriented plates is seen in Figure 31a. The same 0.3 m by 0.3 m square propane sand burner described in Section 2.1.2 was used to generate the fire. For the heat flux mapping experiments, the test plate was positioned 0.61 m above the top of the burner and was supported on screw tips to minimize thermal losses to the frame. Fire sizes ranging from 20 kW to 40 kW were used in the horizontal configuration. The

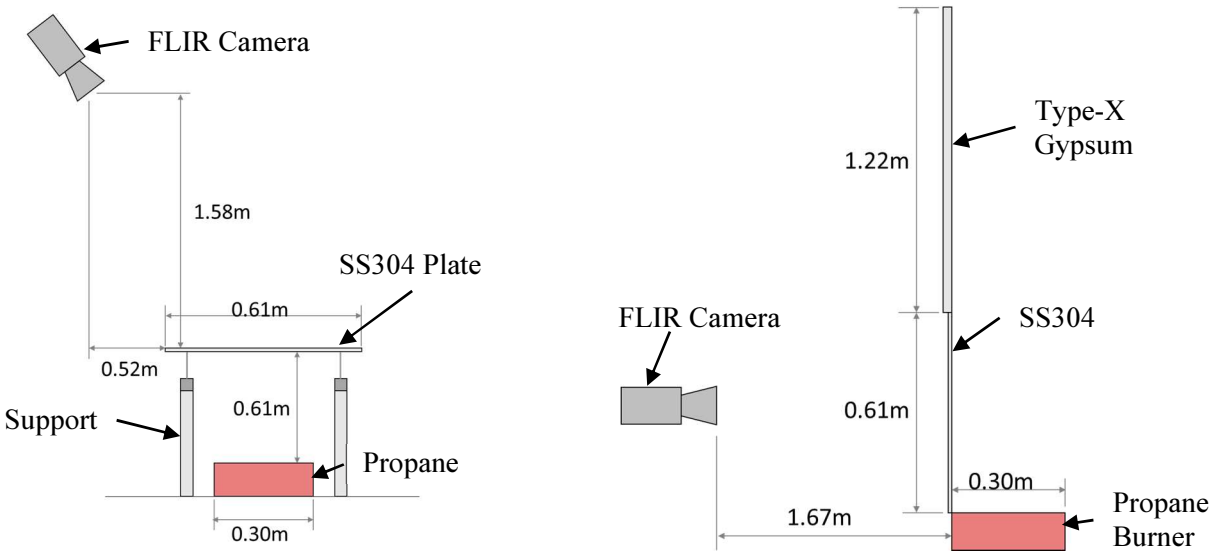

Figure 31. Experimental test apparatus for measuring heat fluxes on a horizontally and vertically oriented surface exposed to diffuse propane flame.

experimental setup for vertically oriented plates exposed for heat flux mapping is seen in Figure 31b. Fire sizes ranging from 50 kW to 100 kW were used in the heat flux mapping experiments. For the fire exposure experiments, measurement plates made of SS304 and AA6061 sheet were used. SS304 plates were used for fire exposures in both the horizontal and vertical configurations while the AA6061 plates were only used in the horizontal orientation.

Because of ventilation requirements, the FLIR camera could not be placed directly over the test plates in the horizontal orientation. This created skewed thermographs of the test article that were then rectified using a basic linear rectification model implemented within MATLAB before calculating the exposure flux. To investigate the effects of grid size and plate material, the spatial resolution of the temperature map was reduced through a Gaussian averaging scheme. Using this scheme, the pixel resolution of the temperature map was reduced to 52 by 70 which provided an 11 mm grid size (120 mm^2). The spatial resolution was then further reduced to 25 by 33 pixels which provided a 23 mm grid size (530 mm^2). This averaging scheme was used to allow for the analysis of identical test data at multiple resolutions. This eliminated errors associated with the random nature of the fire dynamics from the sand burner. Most tests were conducted using a frequency of 1 Hz as rapid changes in the heat flux profile were not expected and increasing the temporal resolution will increase uncertainty in the heat flux measurement. Select tests were performed at 5 Hz and 13 Hz to investigate these uncertainties.

Schmidt-Boelter HFG measurements were taken on horizontal plates exposed to the sand burner using the same method described previously in the radiant heater panel tests. For tests conducted with the sand burner, the gauge was placed at the plate center as well as the center of each quadrant of the plate which provided five measurement locations. For each test conducted using the propane burner, heat flux or thermography measurements were collected for 30 seconds prior to igniting the burner. For tests with the Schmidt-Boelter HFG, the burner was run for 300 seconds. For tests using the IR camera, the burner was run until the plate reached thermal steady-state conditions (300-600 s). After the burner was cutoff, measurement data was collected for an additional 60 seconds during cool down. For the thermography tests, this period was used to help determine the accuracy of the convective boundary conditions on the plate surfaces. Since IR thermographs were taken at rates of 1 and 5 Hz, this provided between 300 and 3000 thermographs for each test.

5.3 Method and Analysis

5.3.1 Inverse heat transfer analysis

In the inverse heat transfer analysis, the total heat flux into an exposed surface is calculated through an energy balance of a discretized element of a plate. Figure 32 contains the energy balance for exposed discretized elements. This energy balance can be expressed as:

$$Q_{exp} + Q_{cond} - \varepsilon_b \Delta^2 \sigma_{SB}\left(T_{x,y}^4 - T_\infty^4\right) - h_b \Delta^2 \left(T_{x,y} - T_\infty\right) = \rho \delta \Delta^2 c_p \frac{T_i - T_{i-1}}{\mathrm{t}} \tag{22}$$

where Q_{exp} is the total energy absorbed by the exposed surface defined as

$$Q_{exp} = \varepsilon_f Q_{rad} - \varepsilon_f \Delta^2 \sigma_{SB} T_{x,y}^4 + h_f \Delta^2 \left(T_{gas} - T_{x,y}\right) \tag{23}$$

where Q_{rad} is the irradiation from the fire exposure. One problem with this total heat transfer term is that changing surface temperature causes time-varying heat transfer for constant exposures. To avoid this, exposures are often measured as a standard heat transfer which is the net heat transfer to a surface that is maintained at the standard temperature condition (T_0=298K). The standard heat transfer is preferred because the constant temperature of the surface eliminates the time dependent effects for constant exposures. Also, the standard heat flux is directly measured by Gardon and Schmidt-Boelter heat flux gauges (HFGs) when these devices are cooled to the standard temperature. Using an energy balance on a surface maintained at the standard temperature, the energy into a surface can be calculated as

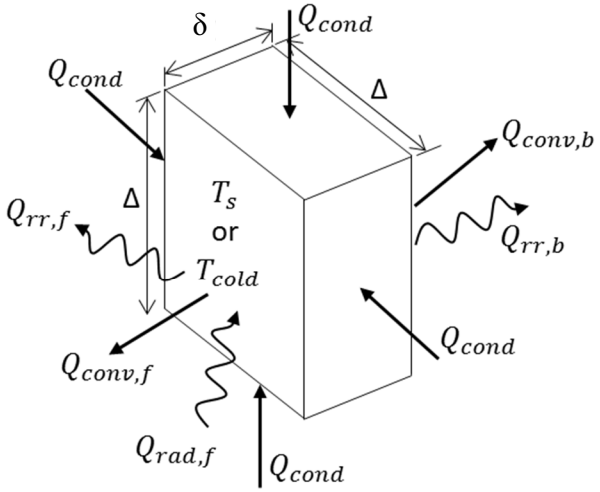

Figure 32. Energy balance for inverse heat transfer analysis of spatially discrete element.

$$Q_0 = \varepsilon_f Q_{rad} - \varepsilon_f \Delta^2 \sigma_{SB} T_0^4 + h_f \Delta^2 \left(T_{gas} - T_0\right) \tag{24}$$

The relationship between the calculated standard heat transfer and heat transfer to a surface heated to T_s can be obtained by combining Eqs. (23) and (24) to eliminate the absorbed irradiation.

$$Q_{exp} = Q_0 - \varepsilon_f \Delta^2 \sigma_{SB} \left(T_{x,y}^4 - T_0^4\right) - h_f \Delta^2 \left(T_{x,y} - T_0\right) \tag{25}$$

The conduction term in Eq. (22) is calculated through an implicit finite difference discretization of Fourier's law between the element and surrounding elements. In this analysis, an implicit relationship between the spatial temperature gradient and the conduction flux is used. However, since the analysis is being done in an inverse setting, this provides an explicit form for the conduction heat transfer. The expression of Fourier's law was further simplified in this analysis since the discretized spatial differentials are a unity value for square discretizations in plane. Finally, the standard heat flux onto the surface at a single element can be found by combining Eqs. (22) and (25), adding the explicit conduction calculation, and dividing by the exposed surface area

$$q_0 = \frac{k\delta}{\Delta^2}\left(T_{x-\Delta,y} + T_{x+\Delta,y} + T_{x,y-\Delta} + T_{x,y+\Delta} - 4T_{x,y}\right) + \varepsilon_b \sigma_{SB}\left(T_{x,y}^4 - T_\infty^4\right) + h_b\left(T_{x,y} - T_\infty\right) + \varepsilon_f \sigma_{SB}\left(T_{x,y}^4 - T_0^4\right) + h_f\left(T_{x,y} - T_0\right) + \rho\delta c_p \frac{T_i - T_{i-1}}{\mathrm{t}} \tag{26}$$

Eq. (26) can be applied on each pixel (or group of pixels) of a thermal image to produce a spatially varying heat flux map. The inverse heat transfer analysis was implemented in MATLAB for this study. Temperature dependent thermal properties of the plate were used to increase the accuracy of the analysis.

One of the primary difficulties with implementing this method is the need for the local convective heat transfer coefficient at each pixel in the analysis. Since fires produce a non-uniform exposure heat flux distribution, local convection coefficients have to be approximated through correlations from simplified exposure scenarios. For this study, a spatially and temporally constant convection coefficient was implemented based on natural convection over an isothermal flat plate at 573 K. This temperature was selected based on the experimentally observed plate temperatures. Convective heat transfer coefficients were taken from correlations bay Sparrow *et al.* [61] for the horizontal plate and Churchill and Chu [62] for the vertical plate. For a horizontal plate, this was calculated as

$$h = Nu * k/L$$

where

$$Nu = 0.15Ra^{\frac{1}{3}}$$

$$Ra = \frac{g\beta(T-T_\infty)L^3}{\nu\alpha} \tag{27}$$

$$\beta = -\frac{1}{\rho}\frac{\rho_\infty - \rho_s}{T_\infty - T_s}$$

$$L = \frac{A_s}{P}$$

One should note that this relationship for Nusselt number is only valid for Rayleigh numbers greater than $1*10^7$. For a vertical plate, the convection coefficient was calculated using the same equations except the correlation for the Nusselt number was

$$Nu_L = \left\{0.825 + \frac{0.387Ra_L^{1/6}}{\left[1+(0.492/Pr)^{9/16}\right]^{8/27}}\right\}^2 \tag{28}$$

For this study, the convection heat transfer coefficients were calculated to be 9.3 W/m^{2}K and 8.7 W/m^{2}K for the horizontal and vertical plates, respectively. Although this approximation will be fairly accurate for the unexposed side of the plate, the presence of the fire on the exposed side make the determination of the actual convective heat transfer coefficient much more difficult. In order to simplify the measurement method, the use of the unexposed side convective heat transfer coefficient was also implemented on the exposed side in this study. Further assessment of the exposed side boundary condition and its effect on the calculated heat flux is found in Section 5.5.

5.3.2 Scaling and resolution effects

The effect of measurement errors on the calculated heat flux was investigated through the propagation of errors technique [63]. This was done to help understand the impact of several different experimental parameters on the accuracy of the inverse heat transfer method. Using this technique, an estimation of the heat flux measurement error is calculated as

$$\epsilon_{q_0} = \sqrt{S_T^2\epsilon_T^2 + S_h^2\epsilon_h^2 + S_\Delta^2\epsilon_\Delta^2 + [\dots]} \tag{29}$$

where this is continued until each variable in the equation is accounted for. The first parameters to be investigated are the physical scaling and resolution of the measurement. Using propagation of errors, the uncertainty contribution of each term in the inverse analysis is shown in Table 6 for IR thermography of a horizontal stainless steel plate exposed to fire using a measurement frequency of 1 Hz and a spatial resolution of 1.7 cm^2. Here, measurement errors were calculated as the random error measured in experiments. This includes length measurements, temperature measurements, and time measurements. Property errors were set to ten percent of their respective values. Errors in emissivity were calculated based on the camera calibration discussed in Section 2.1.1. Errors in convection heat transfer coefficient were estimated as 30 percent however, as will be discussed in Section 5.5, this estimation is much smaller than actual errors for this setup. An uncertainty analysis of the vertical plate was also conducted. Consistent trends were found between the two analyses. As can be seen, uncertainty in the temperature measurement and the convective heat transfer coefficient are the largest contributors to the uncertainty in the heat flux measurement. Increasing the accuracy of the convective coefficient can be accomplished through the use of more accurate correlations and is not significantly affected by physical scale or resolution of the measurement.

Table 6. Uncertainty analysis parameters and results for horizontally oriented SS304 plate exposed to 20 kW fire.

Parameter	Value	Parameter Error	Flux Error (kW/m^2)
Δ (m)	0.013	2.00E-04	0.02
T (K)	575	0.3	1.46
l (m)	0.00079	1.59E-05	0.12
k (W/m-K)	16.2	1.6	0.06
c_p (J/Kg-K)	515	51	0.65
ρ (kg/m^3)	7900	790	0.65
h (W/m^2-K)	11	3.3	1.89
ε	0.95	0.05	0.58
T_∞ (K)	288	0.3	0.01
t (s)	1	0.0001	0
Total			2.63

The temperature measurement uncertainty has a large impact on the calculated heat flux because it propagates through several channels. Many of these propagation channels are a function of the physical scale of the measurement and the spatial and temporal resolutions. The impact of each

of these was done by further investigating the uncertainty coefficient for the temperature measurement of the analysis pixel

$$S_T = \frac{\partial q_0}{\partial T_{x,y}} = h_f + h_b + 8\left(\varepsilon_f + \varepsilon_b\right)\sigma_{SB}T_{x,y}^3 + \frac{4k\delta}{\Delta^2} + \frac{\rho\delta c_p}{\mathrm{t}} \tag{30}$$

The first three terms in the equation are associated with the surface losses of the plate and are not affected by measurement resolution. The last two terms in the equation are associated with the in-plane thermal diffusion and internal thermal storage, respectively.

The main difficulty associated with scaling this measurement technique to larger sizes is with the thickness of the measurement plate. The plate thickness plays a role in propagating the temperature measurement error through both lateral conduction and thermal storage. Ideally, the measurement plate should be as thin as possible to minimize both of these effects. However, at larger scales, mechanical loading can limit how thin the plate can be. Therefore, in order to maintain the accuracy of the measurement, appropriate spatial and temporal resolutions must be chosen.

When applying an inverse analysis method for heat transfer measurements, it is important to understand the measurement limitations inherent in the method. This occurs through two different mechanisms. The first limitation focuses on the minimum resolvable heat flux based on the spatial and temporal resolutions of the IR camera. For most situations, limitations on the necessary spatial and temporal resolutions are determined by the expected heat flux variations to be measured. In general, the accuracy of the heat flux measurement decreases with both increasing spatial and temporal resolution. However, changing spatial and temporal resolution does not affect the measurement accuracy in a constant fashion. These effects were calculated for the stainless steel plate used in this study (l=0.79 mm) by calculating the value of the last 2 terms of Eq. (30) for varying spatial and temporal resolutions. Figure 33 shows a plot of the resolution effects on the uncertainty coefficient for the temperature measurement. As expected at high spatial resolutions, errors from thermal diffusion dominate the measurement. In this region, temporal resolution has very little effect on the measurement accuracy. Likewise at high temporal resolutions, errors from thermal storage dominate and spatial resolution plays a smaller role.

The second limitation is that as plate dimensions increase the thermal signal is attenuated due to the thermal mass of the plate and lateral thermal diffusion. Nakamura investigated these

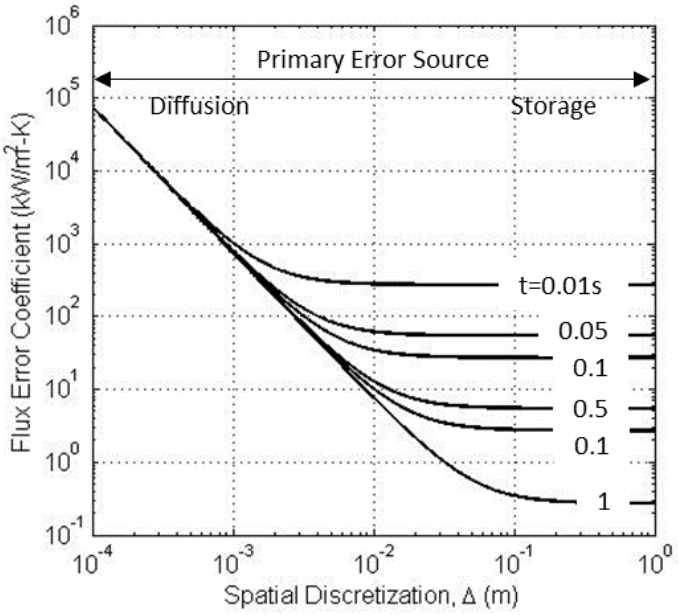

Figure 33. Effect of spatial and temporal resolution on the surface heat flux measurement error through thermal diffusion and storage.

limitations for a thin metallic foil with an insulated backing exposed to convective heating while conducting IR thermography of the exposed surface [64]. The minimum detectable heat flux variations are a function of the measurement plate and the minimum NETD of the IR camera. The procedure for calculating the attenuation can be adapted for this setup by removing the effects of the insulating backing and applying the exposure flux as well as convective and radiative boundary conditions to the unexposed side. With known spatial and temporal resolutions, the minimum detectable temporal and spatial fluctuations in the exposure flux can be calculated, respectively, as

$$q_{\Delta} = \frac{4k\delta T_{NETD}}{\varepsilon \Delta^2} \tag{31}$$

$$q_t = \frac{2\pi T_{NETD}\rho\delta c_p}{\varepsilon t} \tag{32}$$

Using these equations, and knowing expected variations in the measured heat flux, it is possible to select appropriate plate material and dimensions for the heat flux measurement. This selection involves balancing having enough spatial and temporal resolution to adequately capture the heat flux and not having overly sensitive measurements as to overwhelm meaningful data. In this study, experimental measurements were made with stainless steel plate because its material properties

make it good for balancing the minimum detectable heat flux fluctuations and mitigating measurement noise.

5.3.3 Plate material effects

The effects of plate material on the inverse heat transfer calculation were also investigated using the uncertainty coefficient for the temperature measurement. Like the scaling and resolution effects, the first three terms are associated with surface conditions and are unaffected by plate material whereas the internal diffusion and storage are affected. For this study, SS304 and AA6061-T651 were chosen for plate materials. SS304 was chosen because it has been successfully implemented in several other IR thermography based measurement techniques. AA6061 was chosen as a second material because it is the material used in burnthrough experiments in this study. Because AA6061 properties contrast that of SS304 with AA6061 having a higher thermal conductivity and a lower thermal mass, the validity of the methodology needed to be assessed to determine the feasibility of generating *in situ* heat flux maps from burnthrough test temperature measurements. Based on these property differences it would be expected that heat flux maps generated using the SS304 plate at higher spatial resolutions and lower temporal resolutions would have less uncertainty than those produced using the AA6061. Likewise, the AA6061 would be expected to perform better under higher temporal resolutions and lower spatial resolutions due to its lower thermal mass. Under this assumption there exists a temporal and spatial resolution at which the temperature errors propagated through the analysis are expected to be equal. This resolution ratio can be calculated by setting Eq. (30) equal for each of the plate materials

$$\frac{4k_{SS}\delta}{\Delta^2}+\frac{\rho_{SS}\delta c_{p,SS}}{\mathrm{t}}=\frac{4k_{AA}\delta}{\Delta^2}+\frac{\rho_{AA}\delta c_{p,AA}}{\mathrm{t}} \tag{33}$$

Here, the terms associated with the surface conditions have been eliminated as they are equal for both plates. Using Eq. (33) a ratio of spatial and temporal resolution can be established where both the SS304 and AA6061 plates perform equally as

$$\frac{\Delta^2}{t}=\frac{4(k_{AA}-k_{SS})}{\rho_{SS}c_{p,SS}-\rho_{AA}c_{p,AA}} \tag{34}$$

For these materials, this resolution ratio is approximately $5.03*10^{-4}$ m^2/s but varies slightly depending on temperature due to the temperature dependency of the material properties. Figure

34 contains the portion of the temperature uncertainty coefficient in Eq. (30) associated with the internal fluxes as a function of this resolution ratio in Eq. (34). At high spatial and low temporal resolutions, the performance of the SS304 plate is expected to be approximately an order of magnitude better than the AA6061 plate which is expected because the thermal conductivity of the AA6061 is about an order of magnitude larger than that of the SS304 plate. Likewise at low spatial and high temporal resolutions, the performance of the AA6061 is expected to be approximately 50% better than the SS304 plate due to the smaller thermal mass of the aluminum. The ratio of $5.03*10^{-4}$ m^2/s where the two materials are expected to perform equally for all of the shown resolutions. Figure 34 also suggests that each material will have an optimal resolution ratio to achieve minimum uncertainty for a given temporal resolution. For a 1*s* time resolution, this is approximately $1x10^{-4}$ m^2/s for SS304 and $1x10^{-3}$ m^2/s for AA6061.

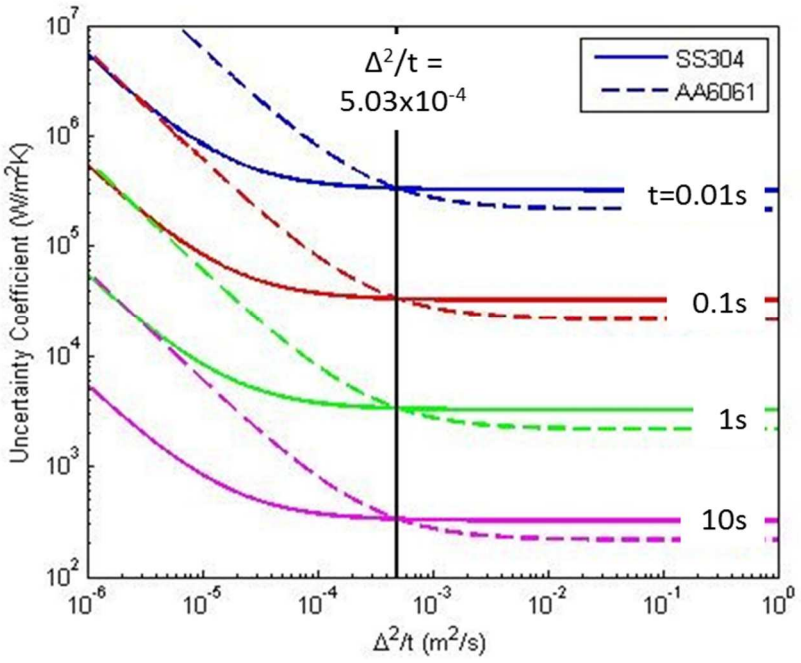

Figure 34. Effect of plate material on surface heat flux measurement error.

5.4 Results

5.4.1 Heat Flux Measured Using IR Thermography Method and Schimdt-Boelter HFG

The results of the radiant panel tests are shown in Table 7. For these tests, the measured heat flux from IR thermography was within one standard deviation of that measured using a Schmidt-Boelter HFG at the center of the exposed plate. The heat fluxes from the IR thermography were determined using natural convection heat transfer coefficients on both sides of the plate. Full-field

heat fluxes are shown in Figure 35 for the radiant panel tests. The heat flux is relatively uniform around the plate center and above the plate center. This is expected as the radiant heater panels extended above the top of the plate. Around the sides and bottom of the plate, the heat flux is lower because they are adjacent to the edge of the radiant panels making the view fraction between the hot panels and points around these edges of the plate smaller than those of the plate center.

Table 7. Comparison of standard surface heat flux measurements from radiant heater panel via traditional technique and IR thermography of SS304 plate.

Heater Panel Temperature (°C)	Measured Surface Heat Flux (kW/m^2)			
	Schmidt-Boelter HFG		IR Thermography	
	Mean	Deviation	Mean	Deviation
500	8.5	0.3	8.8	0.6
600	14.1	0.4	14.6	0.9
700	21.4	0.6	22.3	1.3

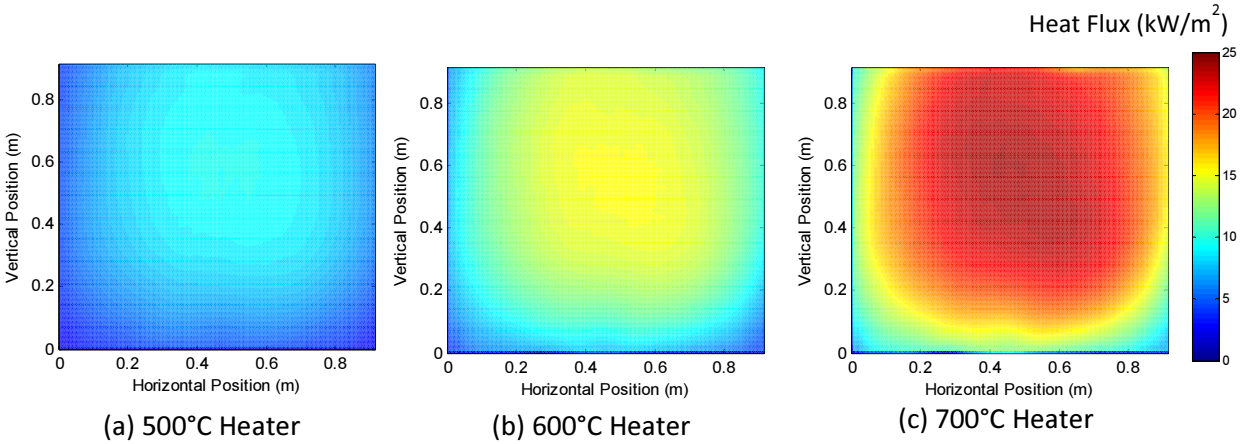

Figure 35. Time-averaged full-field heat flux maps for plates exposed to radiant heater panels at multiple temperatures.

For the horizontally oriented plates exposed to fire, a comparison between time averaged heat fluxes over the duration of the exposure measured by the Schmidt-Boelter HFG and through IR thermography with the SS304 plate is seen in Table 8 for each of the five HFG locations. This table contains the mean value and standard deviation of the heat flux for each fire size and location. Heat fluxes measured via IR thermography were calculated to be smaller at the fire stagnation point than those from the Schmidt-Boelter HFG likely due to the higher convective heat transfer coefficient at this location. The opposite trend exists for measurements away from the fire stagnation point. However, away from the stagnation point, the two measurement methods produce heat fluxes that are similar and well within one standard deviation of each other.

Table 8. Comparison of surface heat flux measurements from IR thermography and traditional gauges on horizontally oriented SS304 plate exposed to diffuse flame.

Location	Fire Size (kW)	Measured Surface Heat Flux (kW/m^2)			
		Schmidt-Boelter HFG		IR Thermograph	
		Mean	Deviation	Mean	Deviation
Center	20	8.67	0.99	6.37	1.24
	30	14.11	1.4	11.72	2.63
	40	20.39	2.27	17.4	4.9
Top-Left	20	4.97	0.36	5.76	0.88
	30	8.83	0.6	10.03	2.03
	40	13.25	3.71	14.2	3.91
Top-Right	20	4.61	0.68	5.26	0.98
	30	7.19	1.18	8.83	2.18
	40	11.02	1.87	13.1	4.72
Bottom-Left	20	5.15	0.62	5.79	0.88
	30	9.24	1.3	9.83	1.73
	40	14.66	1.96	14.63	3.69
Bottom-Right	20	5.19	0.64	5.41	0.94
	30	8.12	0.91	8.94	1.73
	40	11.6	1.98	13.5	3.61

5.4.2 Spatial and Temporal Resolution Effects

Figure 36 contains the IR thermography measured standard heat flux maps at each of the three spatial resolutions for the 20 kW fire exposure using the SS304 plate in the horizontal orientation. In these maps, both the loss in the spatial details and the decrease of measurement noise can be observed as the spatial resolution is decreased. However, spatial trends and stagnation point heat

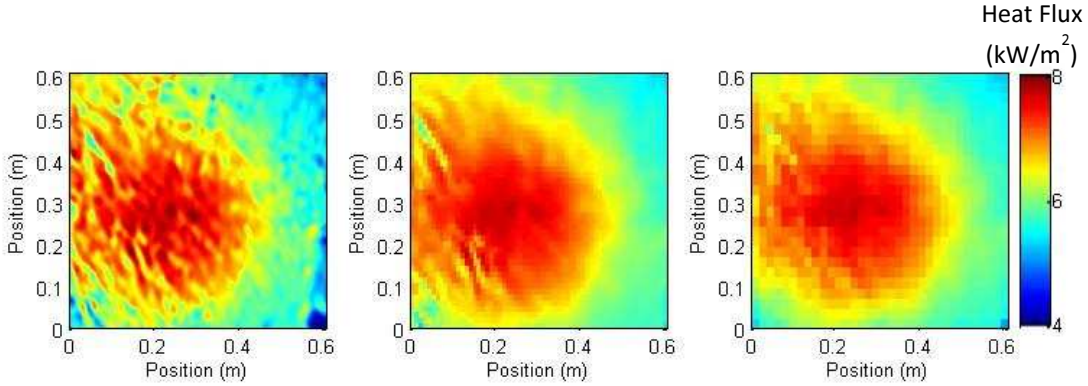

Figure 36. Time averaged full-field surface heat flux maps for horizontally oriented stainless steel plate exposed to 20 kW fire at multiple spatial resolutions.

fluxes are unaffected by these changes. Standard heat flux maps for each of the tested fire sizes in the horizontal orientation at a resolution of 0.02 cm^2 using the SS304 plate are seen in Figure 37. As expected, peak measured heat flux and the radial heat flux gradient increase with increase in fire heat release rate. All of the maps in Figures 36 and 37 are time averaged over the duration of the test.

The effects of spatial and temporal resolution on measurement uncertainty are seen in Figure 38 and Figure 39 by performing separate analyses using varying spatial and temporal resolutions on the same test. Here, full-field maps of the lateral conduction and thermal storage heat flux

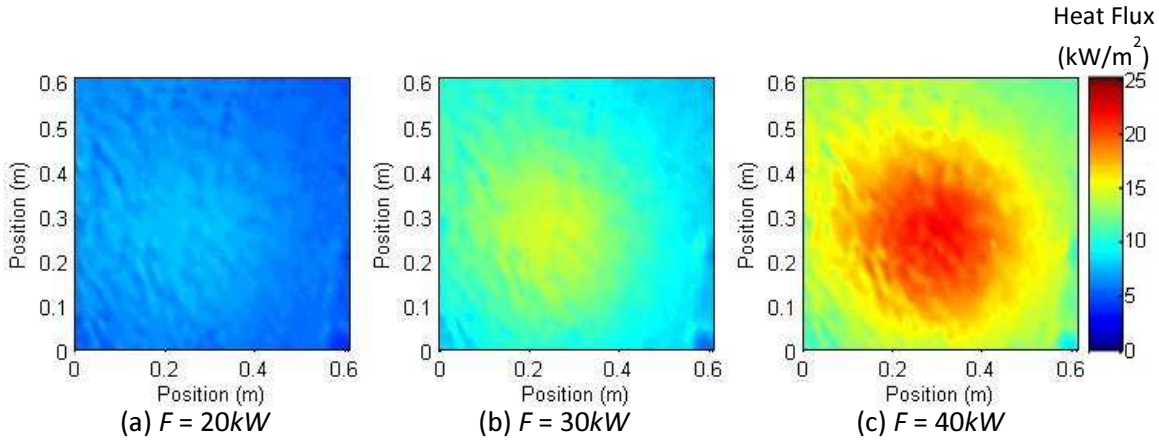

Figure 37. Time-averaged full field heat flux measurements at a spatial resolution of 1.2 mm (1.4 mm^2) on a horizontally oriented stainless steel plate exposed to fires of multiple HRRs.

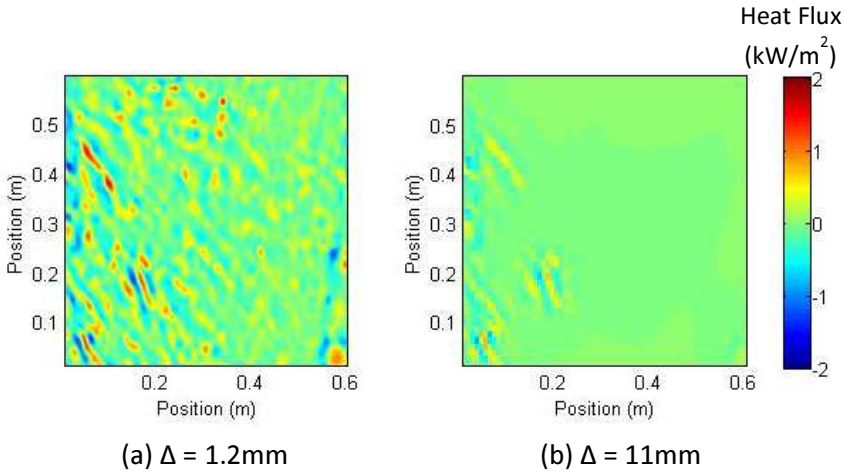

Figure 38. Contribution of calculated in-plane lateral conduction to measured surface heat flux on a horizontally oriented stainless steel plate exposed to a 20 kW fire at multiple spatial resolutions.

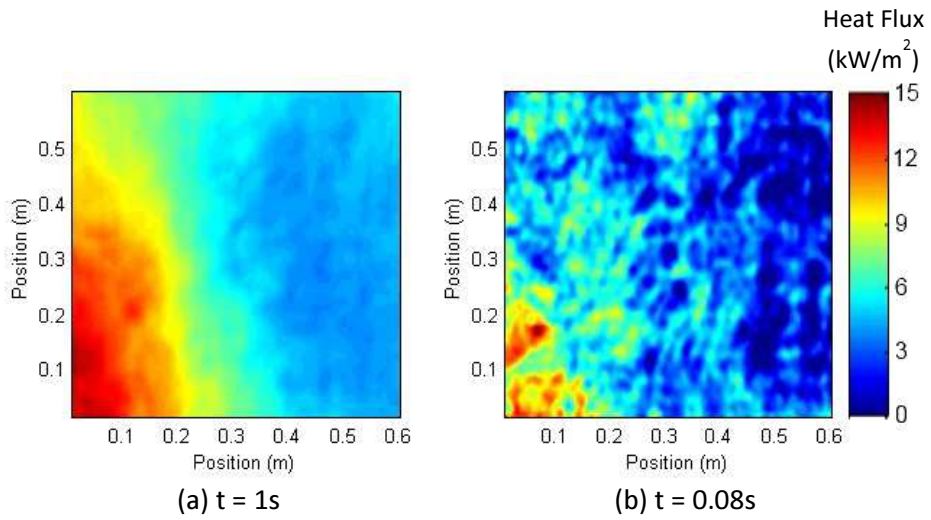

Figure 39. Contribution of thermal storage on the calculated heat flux into a horizontally oriented stainless steel surface exposed to a 20 kW fire multiple temporal resolutions.

components of the inverse analysis are seen for each case. The lateral conduction maps are averaged over the duration of the test while the thermal storage maps are taken from a single pair of images to eliminate the effects of temporal averaging. Results in Figure 38 show a decrease in calculated in-plane conduction flux with a decrease in spatial resolution. Similarly, results in Figure 39 indicate a decrease in calculated thermal storage with a decrease in temporal resolution.

A comparison of standard heat flux maps obtained using the SS304 plate and the AA6061 plate is seen in Figure 40. This is shown for a temporal resolution of 1 Hz and spatial resolutions of 0.02 cm^2 and 5.2 cm^2. For each plate material, the heat flux distributions were from the same test but with different spatial resolutions applied through the Gaussian averaging scheme previously discussed. At a high spatial resolution, more noise exists in the measurements taken using the aluminum plate resulting in less accurate heat flux maps. However, at lower spatial resolutions, the noise has less effect on the heat flux calculation and similar results are obtained with the SS304 and AA6061 plates.

5.4.3 Fires against a Vertical Plate

For the vertical orientation testing, the time averaged standard heat flux for each of the tested fire sizes is provided in Figure 41. Just as the horizontally oriented plates, peak heat flux and spatial gradient increase with increasing fire heat release rate. To validate the results, the centerline heat flux profile of the plate was compared to existing data from Back [51] and empirical correlations developed from that data [53]. This comparison is presented in the subsequent section. The

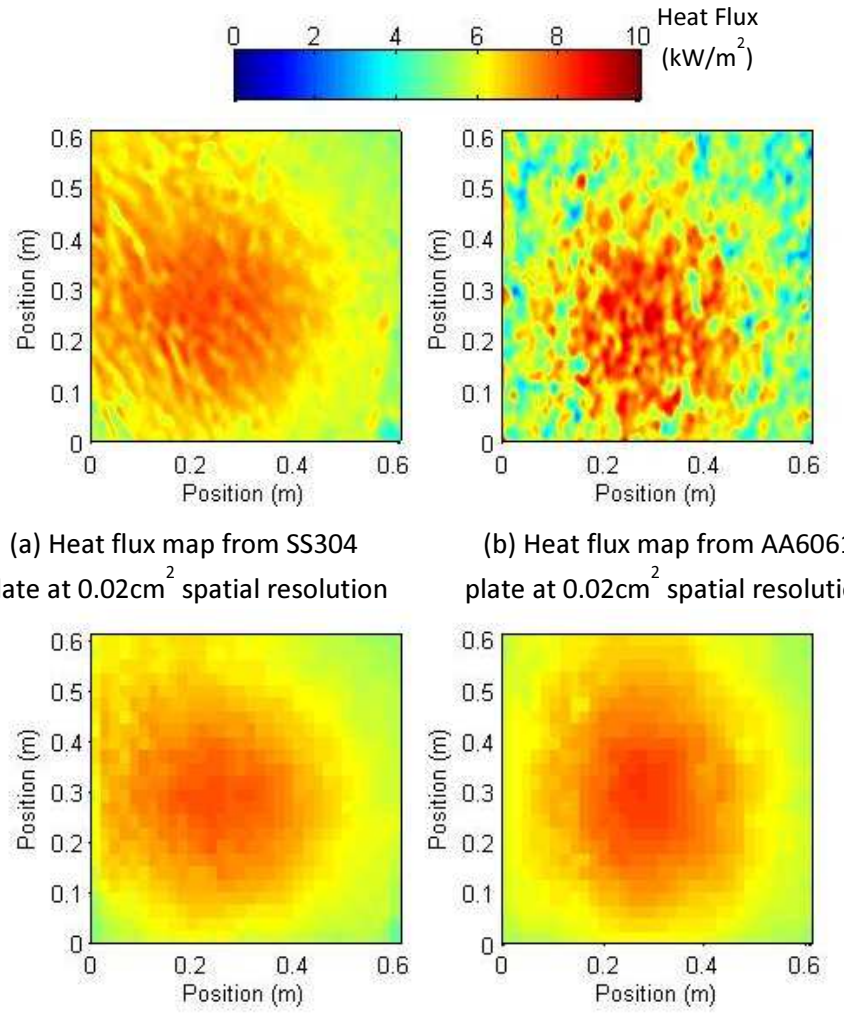

(a) Heat flux map from SS304 plate at 0.02cm^2 spatial resolution

(b) Heat flux map from AA6061 plate at 0.02cm^2 spatial resolution

(c) Heat flux map from SS304 plate at 5.2cm^2 spatial resolution

(d) Heat flux map from AA6061 plate at 5.2cm^2 spatial resolution

Figure 40. Time-averaged full-field heat flux maps for horizontally oriented stainless steel and aluminum alloy plates exposed to 20 kW fire at multiple spatial resolutions.

measurements in this study are significantly lower than those measured by Back. This difference will be discussed in the subsequent section. However, the normalized height of the measurements in this study continue much lower values than were captured by Back.

5.5 Discussion

Inverse heat transfer analysis on IR thermographs was shown in the previous section to provide spatial distributions of heat flux from a fire in two different configurations. A comparison of the heat fluxes from the IR thermography is compared with data from Schmidt-Boelter and other studies to assess the accuracy of the method. In addition, the effect of spatial resolution, temporal

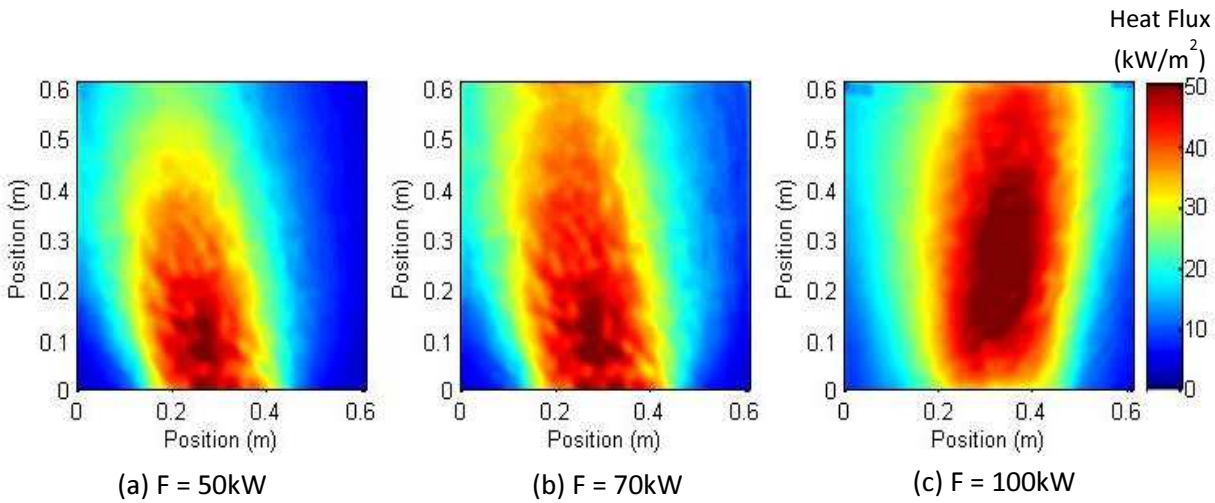

Figure 41. Time-averaged full-field heat flux into a vertically oriented stainless steel plate exposed to fires with multiple HRRs.

resolution, and plate material are further investigated to validate the analysis provided in Section 5.3.

Heat fluxes in Table 8 were compared and it was found that the heat fluxes measured by the Schmidt-Boelter HFG and IR thermography for the horizontal SS304 plate were in agreement with values being within one standard deviation. These heat fluxes are also in agreement with those measured in a separate study by Hasemi et al. [52] with a localized fire exposure impinging onto a ceiling. In the study by Hasemi *et al.*, heat fluxes of 10 kW/m^2 to 20 kW/m^2 were measured at the flame stagnation point for similar fire sizes. Though the results are statistically the same, some of the discrepancy in the results may be attributed to the uncertainty in the convection heat transfer coefficient. Several studies have experimentally measured convection heat transfer coefficient for similar exposures. Veloo and Quintiere [65] found convection coefficients for these temperature ranges to be approximately 30 W/m^{2}K while Wasson [66] found coefficients for similar geometries to be approximately 40 W/m^{2}K. By increasing the predicted convection coefficient at the center from 9.3 W/m^{2}K to 38 W/m^{2}K, the average heat fluxes obtained from the inverse analysis match those from the Schmidt-Boelter HFG. Near the edges of the plate, the heat flux measurement from IR thermography more closely follows that from the traditional gauge. Cooper [67] developed correlations for the radial distribution of convective coefficient for horizontal plates using smaller exposures and non-heated jets. Using these correlations, convective coefficients of 51 W/m^{2}K and 23 W/m^{2}K were calculated for the plate center and quadrant centers, respectively. Using these coefficients, heat flux measurements via IR thermography would be greater than those measured

via Schmidt-Boelter HFG. This difference is attributed to the accuracy of the correlation and that the correlation is generated from experimental data outside parameters used in this study. Ultimately, the accuracy of the heat transfer coefficient can affect the heat flux determined using the IR thermography and highlights a need for more accurate measurements of this in fires.

Validation measurements using the Schmidt-Boelter HFG were not made for the vertical surface tests. Instead, IR thermography measurements in this configuration were compared to existing literature. An experimental study of heat fluxes on vertical surfaces exposed to an adjacent fire was conducted by Back *et al.* [51]. In the study by Back *et al.*, heat flux fields were measured using an array of single point water cooled Schmidt-Boelter HFG. Back *et al.* determined an empirical relationship between fire size and peak heat flux to be

$$q_{peak} = 200\left[1 - \exp\left(-0.09F^{1/3}\right)\right] \tag{35}$$

where F is the fire heat release rate in kW. This relationship was derived from fires with heat release rates ranging from 50 kW to 520 kW and appears to be accurate to within approximately 10 kW/m^2. A comparison of the predicted peak standard fluxes compared to IR thermography peak standard flux is provided in Table 9. The peak heat fluxes measured in this study are in agreement with those from the correlation given the accuracies of the correlation and the measurements.

Table 9. Comparison of peak centerline heat flux values obtained from published correlations and IR thermography.

Fire Size	Correlation	Measured (kW/m^2)	
(kW)	(kW/m2)	Mean	Deviation
50	56.4	49.04	3.98
70	62	50.5	5.73
100	68.3	60.35	5.89

Back *et al.* developed empirical correlations for the variation in the heat flux as a function of elevation above the fire normalized relative to the flame height. It was found that the flame height for an unobstructed plume from Heskestad [68] could also be used to predict the flame height for a fire against a flat wall. As a result, the flame height against a flat wall was determined using the following

$$L_f = 0.23F^{2/5} - 1.02D \tag{36}$$

The centerline heat flux variation with elevation was calculated using the following correlations provided by Back *et al.*

$$\begin{aligned} q_{CL} &= q_{peak} && z/L_f < 0.4 \\ q_{CL} &= q_{peak} - \tfrac{5}{3}\left(z/L_f - 2/5\right)\left(q_{peak} - 20\right) && 0.4 < z/L_f < 1.0 \\ q_{CL} &= 20\left(z/L_f\right)^{-5/3} && 1.0 < z/L_f \end{aligned} \tag{37}$$

For the fire sizes tested in this study, the flame lengths were calculated from Eq. (36) to be 0.79 m, 0.95 m, and 1.14 m for the 50 kW, 70 kW, and 100 kW fires, respectively. A comparison of the measured centerline heat flux to these correlations and experimental measurements by Back *et al.* are seen in Figure 42. Uncertainty in the measured heat flux from IR thermography and the correlations are not shown for clarity. The uncertainties in the measured heat flux are similar to those seen in Table 9 while the uncertainty in the correlations are similar to the 10 kW/m^2 discussed previously. The trend in the heat fluxes from the IR thermography with elevation agree well with the correlations and data from Back *et al.* The peak heat fluxes measured using IR thermography in this study are about 5 kW/m^2 to 10 kW/m^2 lower than what was measured by Back *et al.* Similar to the horizontal configuration, this is likely because the predicted convection heat transfer coefficient of 10 W/m^{2}K at the maximum flux location is likely lower than the actual coefficient. Increasing the convection coefficient to values between 20 W/m^{2}K and 30 W/m^{2}K generates peak heat flux values the same as those obtained from the correlation by Back *et al.* However, it is of

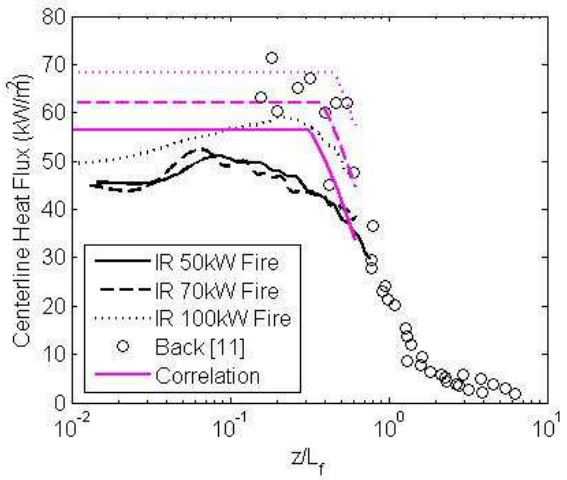

Figure 42. Comparison of centerline heat flux measurement obtained via IR thermography to published correlation of values measured by Back [51].

note that the lines for each fire size describing the vertical distribution of heat flux shown in Figure 42 from the IR thermography in this study consist of nearly 500 data points, which is a significantly higher resolution than captured by Back *et al.* Also because of this high resolution, it was possible to obtain heat flux distributions at very low z/L_f values which is practically impossible with traditional sensors due to the size of the sensor itself.

One difficulty when working with thermographs for heat flux measurements is the inherent noise from the IR measurement. This is especially true with fire exposures that produce random ambient IR radiation that is captured by the camera. In addition, the discretization of Fourier's law is sensitive to random temperature measurement errors. To help mitigate this error, the raw temperature data was filtered before the inverse heat transfer analysis and the temperature differential used in Fourier's law was also filtered. Rainieri and Pagliarini [69] analyzed several two-dimensional filters for use in IR thermography measurements and found that the double application of a Wiener filter provides the best degree of filtering while minimizing losses of detail. This approach has been successfully implemented in previous inverse heat transfer analysis work [60], [70]. For this study, each thermograph was filtered using a 7 by 7 pixel subset before the analysis and the temperature differential was further filtered using an 11 by 11 pixel subset. The effects of this filtering are seen in Figure 43 for the SS304 plate and Figure 44 for the AA6061

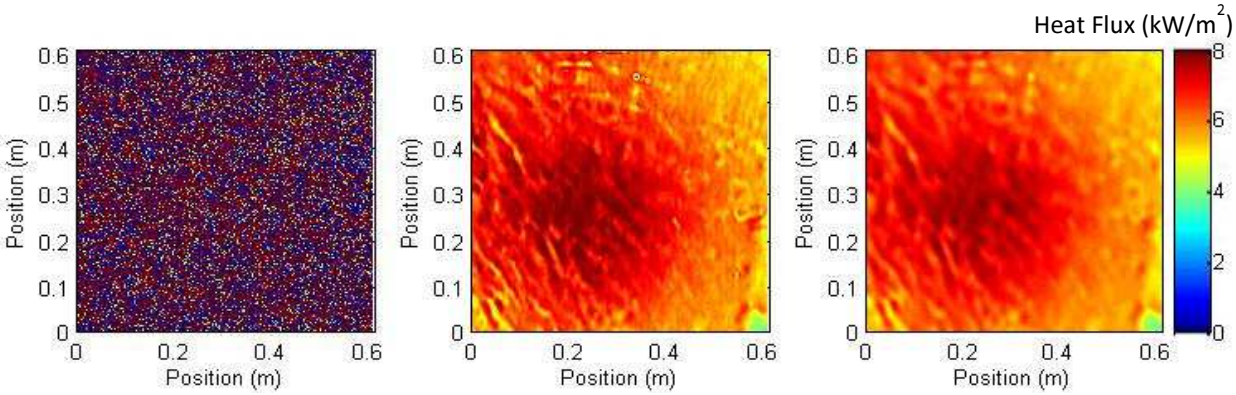

(a) No spatial filtering

(b) Spatial filtering of thermograph

(c) Spatial filtering of thermograph and spatial temperature differentials

Figure 43. Effect of spatial filtering of temperature data and calculated spatial temperature differentials on the calculated instantaneous surface heat flux into a horizontally oriented stainless steel plate.

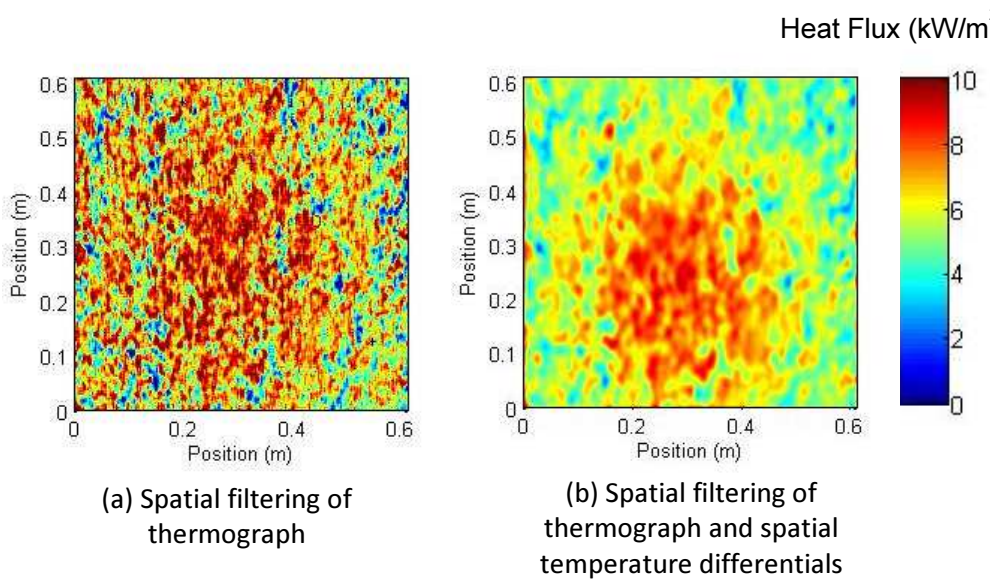

Figure 44. Effect of spatial filtering of temperature data and calculated spatial temperature differentials on the calculated instantaneous surface heat flux into a horizontally oriented aluminum alloy plate.

plate. Both of these figures were generated at a spatial and temporal resolution of 0.02 cm^2 and 1 Hz, respectively. Without the initial filtering of the entire thermograph, heat flux measurements at higher spatial or temporal resolutions are not possible because the ambient noise in the image is amplified through the lateral conduction and thermal storage terms of the inverse analysis. This is seen in Figure 43a for the SS304 plate. Although not as prevalent in the SS304 plate at the tested resolutions, the filtering of the temperature differential within the inverse analysis helps to mitigate the error propagation through the lateral conduction and thermal storage. For the AA6061 plate, the filtering of the temperature differential reduces the noise present in the heat flux map by nearly an order of magnitude as seen in Figure 44. This reduction occurs via the lateral conduction term of the inverse heat transfer analysis because AA6061 has a thermal conductivity approximately one order of magnitude larger than SS304.

The effects of spatial and temporal resolution were previously shown in Figure 38 and Figure 39 using a SS304 plate. For most metals, the effects of lateral conduction will be greater than the effects of thermal storage because metals have a high thermal conductivity. This is true for the SS304 plate used in this study. Using Eq. (31), the minimum resolvable spatial heat flux variation, and ultimately a metric of measurement noise, can be calculated for the different spatial resolutions used in the analysis. For the 0.02 cm^2 resolution, the minimum variation is 2.8 kW/m^2. The

amount of noise present in Figure 36 for this case is lower than this because the data filtering and temporal averaging help to mitigate this error. Likewise, for the 1.7 cm^2 resolution the minimum variation is 0.032 kW/m^2. Figure 38 contains lateral conduction maps which show that switching from a spatial resolution of 0.02 cm^2 to 1.7 cm^2, the amount of noise in the lateral conduction component of the inverse analysis is reduced by approximately an order of magnitude. This large decrease is expected because the minimum resolvable heat flux variations for these resolutions also changes by nearly two orders of magnitude. However, because of the data filtering, the calculated decrease is more than experimentally observed. A similar trend can be seen in the thermal storage, although to a lesser degree. Using Eq. (32), the minimum heat flux variations can be calculated as 10.6 kW/m^2 and 27.8 kW/m^2 for temporal resolutions of 1 Hz and 13 Hz, respectively. The experimentally observed reduction between these two temporal resolutions was found to only be approximately 10% as can be seen by the thermal storage maps of Figure 39. Again the use of data filtering and averaging on the measured thermographs causes this observation to be lower than calculated.

In Figure 40, it can be seen that the performance of the AA6061 plate is significantly worse than the SS304 at the 0.02 cm^2 spatial resolution and 1 Hz temporal resolution. At these spatial and temporal resolutions, the resolution ratio Δ^2/t is approximately $2x10^{-6}$ m^2/s. Based on the temperature uncertainty coefficient differences between the two plate materials from Eq. (30) and plotted in Figure 33, it is expected that the errors from the AA6061 plate be approximately one order of magnitude worse which is consistent with the results in Figure 40. For the lower spatial resolution of 5.2 cm^2, the resolution ratio is $5.2x10^{-4}$ m^2/s which is approximately where equal performance between the two materials is expected. This is also experimentally observed as seen in Figure 40. At even lower spatial resolutions, the AA6061 plate is expected from Figure 33 to perform slightly better than the SS304 plate. However, since the thermal mass of the SS304 plate is only 50% larger than that of the AA6061 plate this difference is expected to be small. Experimentally, no significant difference was observed at lower spatial resolutions. Similar to the resolution effects, this reduction in the observed error was attributed to the filtering of the temporal temperature gradient within the inverse heat transfer analysis.

5.6 Heat Flux Mapping Conclusions

Accurate thermal predictions are necessary for prediction of fire induced burnthrough times and require accurate measurement of the incident heat fluxes on the surface. In order to obtain more accurate heat flux characteristics, a methodology for the calculation of heat flux using temperature measurements was adapted for *in situ* use in fire environments. Utilizing IR thermography, temperature measurements can be made with much higher resolution than possible with traditional techniques. In this study, the utilization IR thermography paired with inverse heat transfer analysis was investigated. The methodology was first validated at the intermediate scale using an SS304 plate exposed to a radiant heat source. Under this more controlled environment, measurements obtained via IR thermography matched within one standard deviation measurements obtained from traditional heat flux sensors.

The heat flux measurement methodology was also implemented to measure surface heat fluxes from diffuse fires onto both horizontally and vertically oriented plates. Surface heat fluxes onto horizontally oriented plates were validated against traditional measurement techniques. Using simplified natural convection coefficient correlations, it was found that heat fluxes calculated using IR thermography generally under-predicted measurements from traditional techniques. However, by utilizing single point convection heat transfer coefficient data, calculated surface heat fluxes match traditional measurements. This highlighted the need for accurate full-field convection heat transfer coefficient data to accurately calculate surface heat flux. Surface heat fluxes into vertically oriented surfaces was compared to data and correlations available in literature. Like the horizontally oriented data, heat flux calculations from IR thermography typically under-predicted values when utilizing simplified natural convection coefficient correlations. However, because of the high spatial resolution of the technique, heat flux measurements could be obtained at much lower flame heights than available in literature.

Lastly, the effects measurement spatial and temporal resolution on as well as surface material on heat flux measurement uncertainty were numerically and experimentally investigated. It was found that increasing resolution also increased measurement uncertainty through in-plane thermal diffusion and thermal storage for spatial and temporal resolutions, respectively. Plate material was found to effect measurement uncertainty through the specific heat capacity for thermal storage and conductivity for lateral diffusion. In comparing SS304 and AA6061 plates, it was found that

SS304 plates perform better at high spatial resolution because the material conductivity is lower while AA6061 plates perform better at high temporal resolution because the specific heat capacity is lower. A specific ratio of spatial and temporal resolution was calculated where the two materials would perform comparably. This behavior was experimentally observed at this resolution ratio.

Chapter 6: Burnthrough Models

6.1 Introduction

In order to predict both the occurrence of burnthrough and the time to burnthrough, the burnthrough mechanisms discussed in Chapter 3 were implemented in the commercial finite element (FE) analysis software Abaqus. The FE analysis was performed in a sequential approach meaning that thermal models were run independently of mechanical models. This decoupled approach neglects any mechanical response dependencies on the thermal response which, as will be discussed subsequently, is aligned with experimental measurement and numerical modeling methodologies used. The primary advantage of the decoupled approach is that it is significantly less computationally expensive than the fully-coupled thermo-mechanical approach. A flow chart of how each aspect of this research is used to support model application and benchmarking is shown in Figure 45.

Here, the development of the FE models of the burnthrough experiments described in Chapter 2 will be discussed and a comparison of experimentally measured and numerically calculated burnthrough results will be conducted.

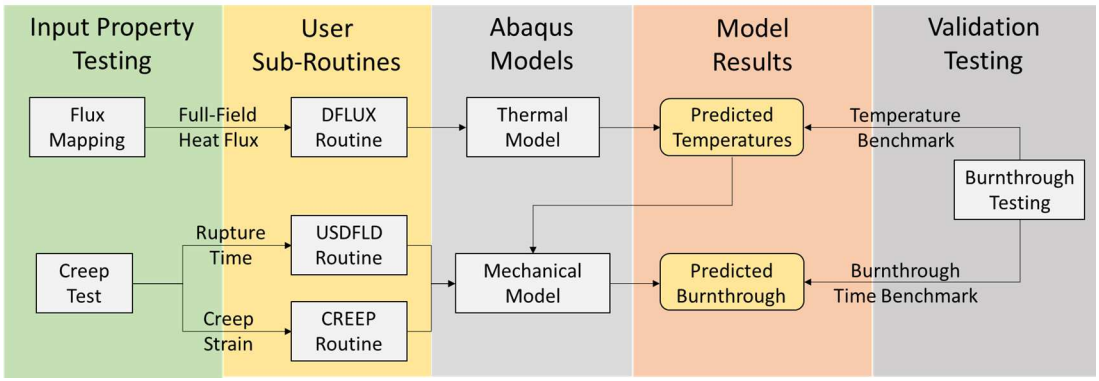

Figure 45. Flow chart for connection of work conducted during research for purposes of development and benchmarking of burnthrough model.

6.2 Benchmark Modeling Approach

6.2.1 Thermal Model

A series of thermal FE models were developed to predict the full-field transient temperature response of the test plates. For each of these models, the full plate geometry was implemented into Abaqus. Although geometric symmetry exists for the test plates along with nominal radial symmetry of the exposure, no model symmetry was implemented because a spatially discrete

measured full field heat flux was applied to the plates as described below. All of the thermal models utilized 20 node solid quadratic thermal elements (DC3D20). For all thicknesses, only a single element was used through the plate thickness which provided three temperature predictions through the plate thickness. This was done because no significant thermal gradient was expected or observed in this direction. Although element aspect ratios need to be minimized in mechanical finite element analyses, thermal finite element analyses are not sensitive to problems caused by large element aspect ratios. Thus, the only requirement for selecting in-plane mesh densities is the ability to adequately capture the expected in-plane thermal gradients. Because of this, all thermal models were conducted with in plane meshes seeded at 30 mm which provided element aspect ratios ranging from 4.7 to 38.

For all of the thermal analyses, temperature dependent thermal properties of the material were used. Figure 46 shows the thermal conductivity for solid aluminum used in the analyses. Values were specified at intervals of 50 to 100°C with linear interpolation between specified values as shown in the figure. Because several different experimental parameters caused material melting, the latent heat of the phase change needed to be incorporated into the thermal properties. This was done using an apparent specific heat in the phase change region. The apparent specific heat was previously measured using a differential scanning calorimeter. Figure 47 contains the apparent specific heat used in the thermal models including the phase change temperature. Apparent specific heat is also shown focused on solid phase values in Figure 47b. For all models, a constant density of 2690 kg/m^3 was used. Any changes in material density were implemented via thermal expansion in the mechanical models are discussed in the subsequent section.

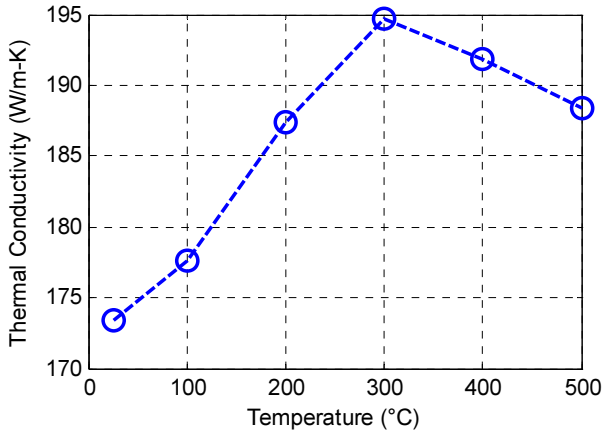

Figure 46. Material thermal conductivity for AA6061 used in thermal FE models.

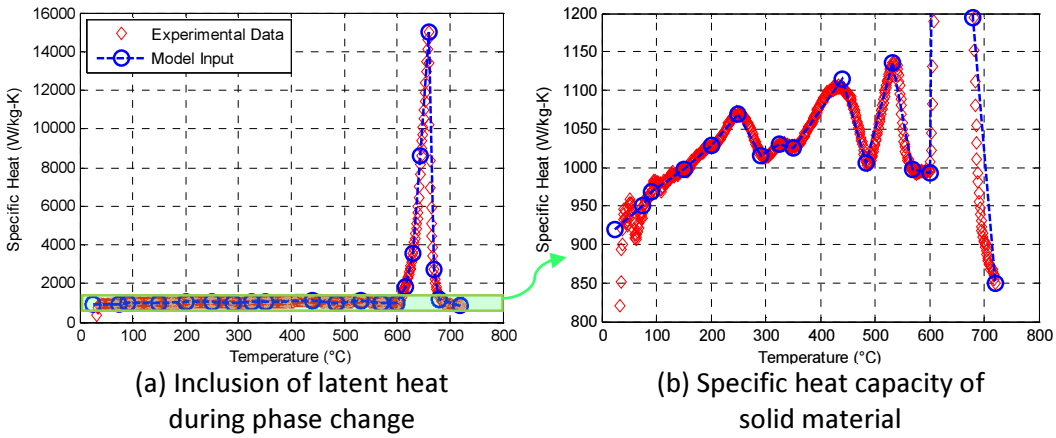

Figure 47. Apparent material specific heat capacity including latent heat used in thermal FE models.

Heat fluxes were applied to all of the thermal models based on the full-field heat flux mapping discussed in Chapter 5. The time-averaged heat flux profile for the plates exposed to the jet burner are shown in Figure 48 and Figure 49 for the vertically and horizontally oriented plates, respectively. Likewise, heat flux profiles for plates exposed to the sand burner are shown in Figures 50 and 51 for vertically and horizontally oriented plates, respectively. Each of these heat flux maps was generated using a 0.79 mm thick SS304 plate like that described in Section 5.2. The spatial resolution of the heat flux maps was decreased using a Gaussian averaging scheme to 16 mm. This resolution was chosen because it could adequately capture the measured heat flux profiles while minimizing computational costs involved with the thermal model. The temporal resolution of the heat flux maps used in the thermal models was 1s.

For all of the models, spatially and temporally discrete heat flux maps were applied using the Abaqus user sub-routine DFLUX. This routine is shown in Appendix 1. The DFLUX routine was setup to handle both incompatible meshing between the heat flux map and the thermal model as well as incompatible time discretizations. For both incompatibilities, linear interpolation between heat flux measurement locations and times was applied in the thermal model. One difficulty in working with exact heat flux measurements is allowing thermal model durations longer than those of the heat flux measurement. Since the exposure is nominally constant with respect to time, heat flux maps are applied in a repeating fashion to allow for indefinite thermal modeling using a

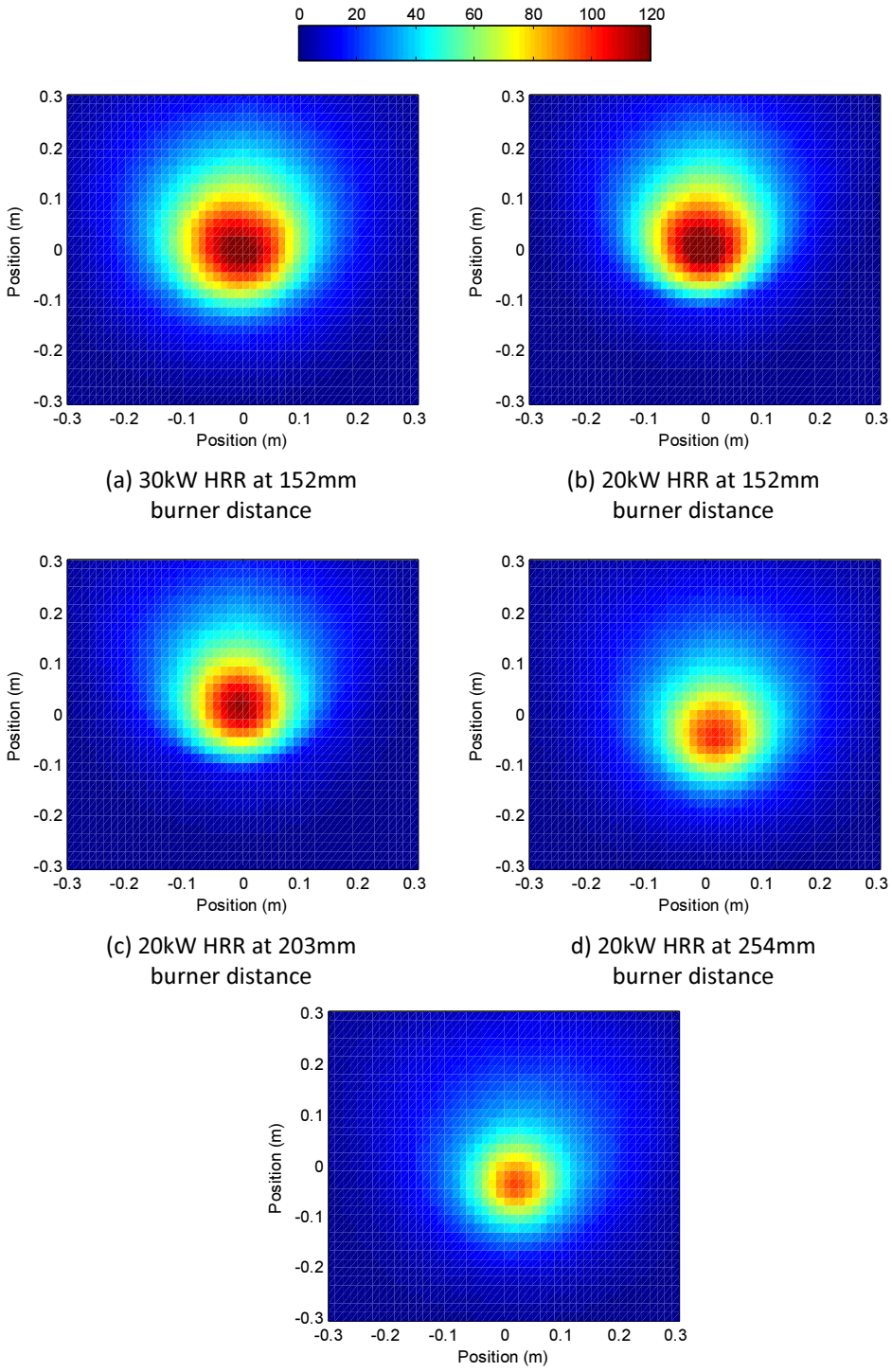

Figure 48. Time-averaged full-field heat flux applied to FE models of vertically oriented plates exposed to propane jet burner.

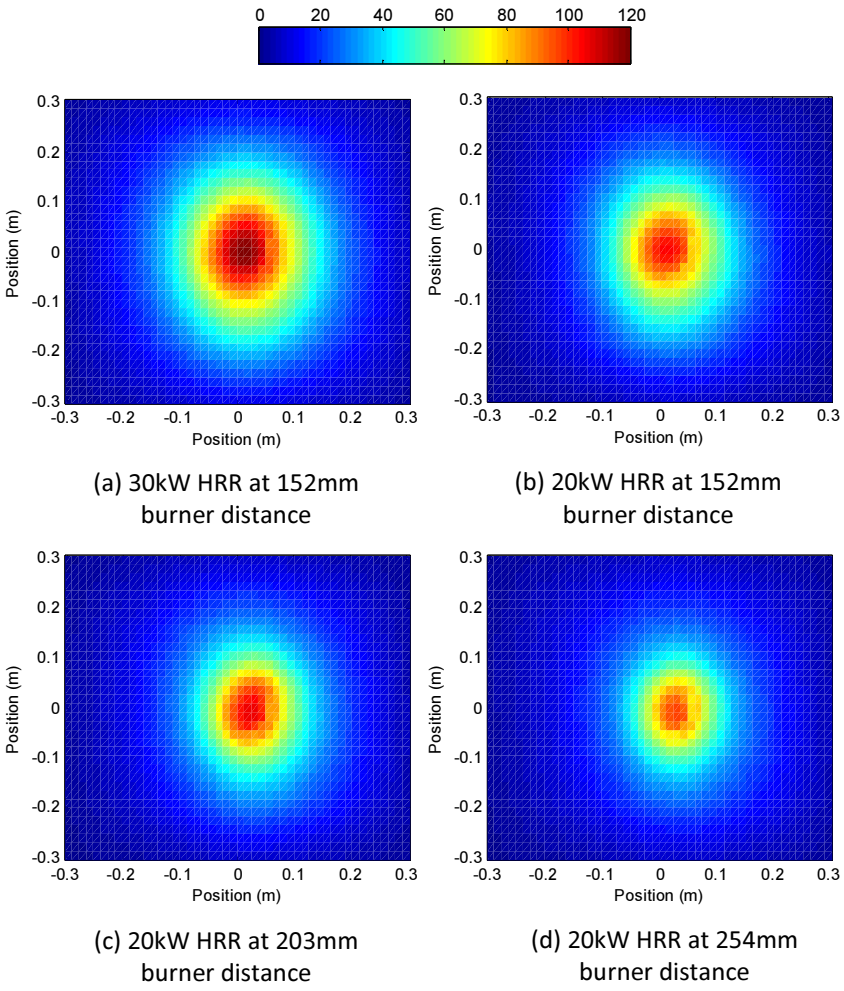

Figure 49. Time-averaged full-field heat flux applied to FE models of horizontally oriented plates exposed to propane jet burner.

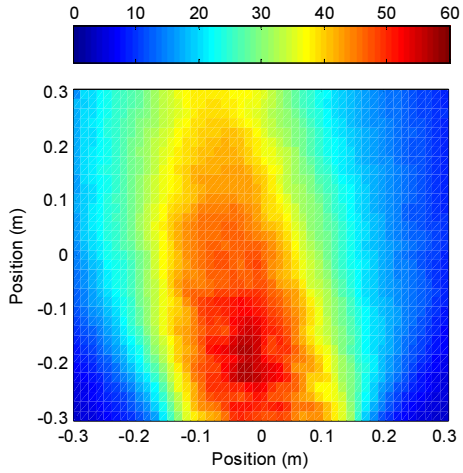

Figure 50. Time-averaged full-field heat flux applied to thermal FE models of vertically oriented plate exposed to propane sand burner.

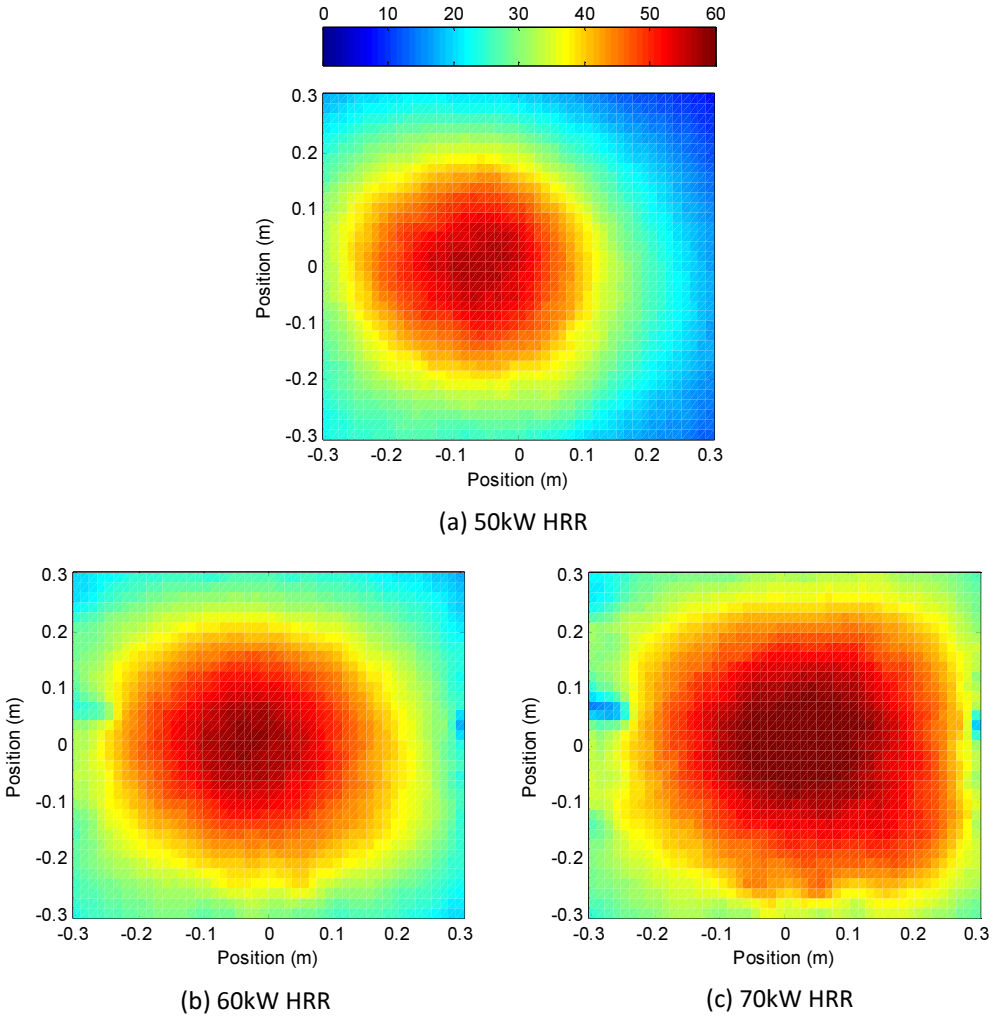

Figure 51. Time-averaged full-field heat flux maps used in thermal FE models of horizontally oriented plates exposed to propane sand burner.

definite amount of heat flux maps. That is, although heat flux mapping was only conducted for 300 s, for longer simulations these 300 s are repeated to allow for thermal predictions.

Convection and radiation thermal boundary conditions were applied to both the unexposed and exposed sides of the model plate. For each test, an emissivity of 0.95 was applied to all surfaces painted with high emissivity paint. For bare aluminum surfaces, an emissivity of 0.5 was used. Natural convection correlations by Sparrow *et al.* [61] were used for convection on the unexposed surface as described by Eq. (27) and (28) in Section 5.3.1. A peak surface temperature of 500°C was used in the convection heat transfer coefficient calculation which yielded a value of 10.1 W/m^2K for horizontally oriented plates and 9.6 W/m^2K for the vertically oriented plates. While

these correlations are appropriate for the unexposed surface, they were also implemented for the exposed surface. As discussed in Section 5.5, these correlations under-predict the actual convection heat transfer coefficient for the exposed surface. However, this does not produce large errors in thermal predictions so long as consistent convection coefficients are used in both the thermal model and the calculation of incident heat flux using the inverse method discussed in Chapter 5. This is because and under prediction in convection coefficient in the heat flux calculation produces under predicted heat flux values which, in turn, negate errors caused by under predicted convection coefficients in the thermal analysis. No convection or radiation boundary conditions were applied to the edges of the plate in the thermal models. This has no significant effect on the thermal prediction as the surface area of the plate edges accounted for less than 2.5% of the total surface area for the thickest plates.

6.2.2 Mechanical Model

Once plate temperature predictions were generated using the thermal models, these were inserted into mechanical models to predict the stress response and burnthrough behavior of the plate. For all of the mechanical models, temperature dependent mechanical properties were used. Figure 52 contains the temperature dependent thermal expansion coefficient used for all the mechanical models. Like the thermal properties, linear interpolation was used between the specified temperatures and a constant extrapolation of the expansion coefficient was used at temperatures above 450°C. A full representation of the material's stress-strain behavior as measured by Allen

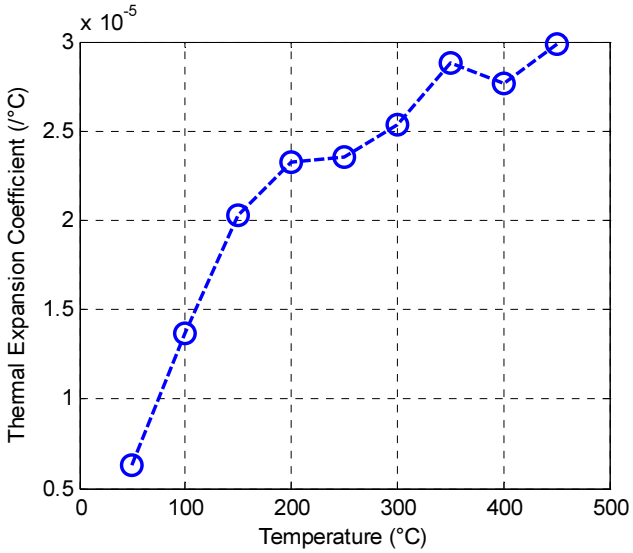

Figure 52. Thermal expansion coefficient used in mechanical FE models.

[34] was included in the model. Data from Allen was recorded in an engineering stress and strain form. These experimental engineering stress-strain curves are shown in Figure 53. Abaqus input requires stress-strain information in the true (Cauchy) stress true-strain form. True strain of the material was calculated using the integral conversion:

$$\varepsilon_{true} = \int_{L_i}^{L} {}^{1}/_{L}\, dL = \ln({}^{L}/_{L_i}) \tag{38}$$

Where L is a unit length of the tensile test specimen. Using the relationship, the current length is equal to the initial length plus the change in length, Eq. (38) can be rewritten as

$$\varepsilon_{true} = \ln(1 + \varepsilon_{eng}) \tag{39}$$

Using the constant volume approach, an approximation for the material true stress prior to material necking can be calculated as

$$\sigma_{true} = \sigma_{eng}(1 + \varepsilon_{eng}) \tag{40}$$

Figure 54 contains the approximated true-stress true-strain relationships used in the mechanical models. These relationships are stylized from the experimental data because measurement noise in the data can cause convergence issues in the finite element model. Additionally, traditional finite element solvers cannot handle decreases in applied true stress with increasing strain. Stress-strain inputs that exhibit this behavior were truncated at their peak stress value and linear

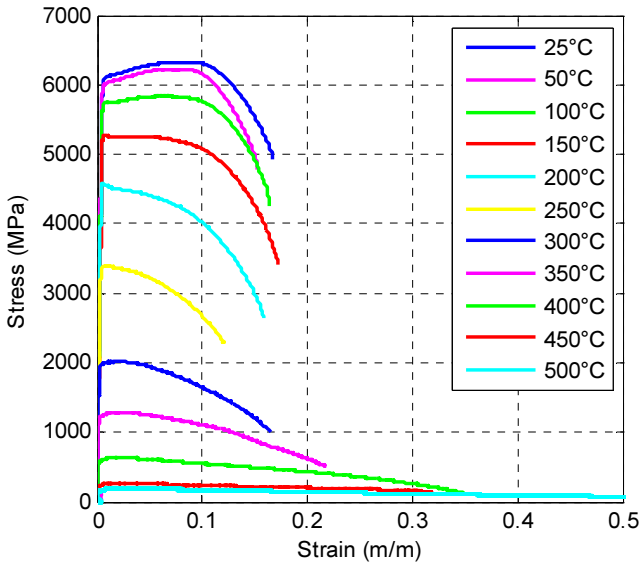

Figure 53. High temperature engineering stress strain curves as measured by Allen [34].

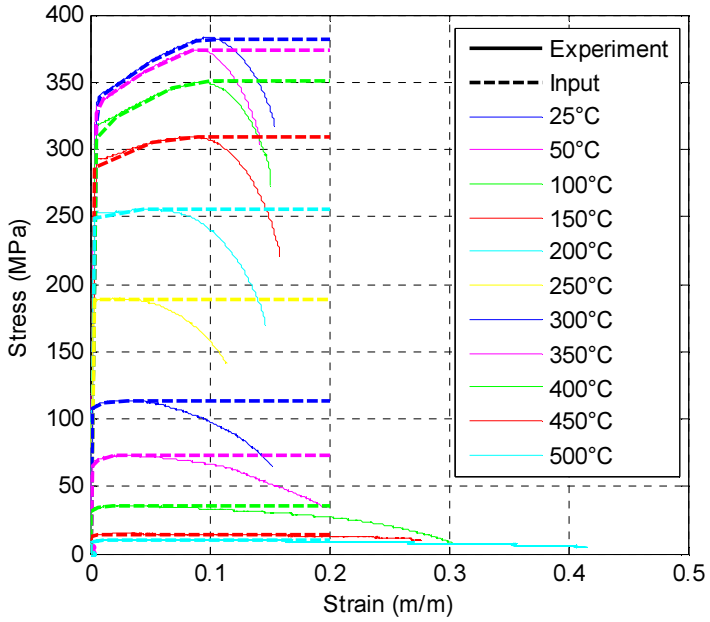

Figure 54. Converted high temperature true stress-strain behavior used in mechanical FE models.

extrapolation of that peak value was used by the solver at high strains. Secondary and tertiary creep response of the material was also implemented in the mechanical models. Because the Abaqus framework does not include a tertiary creep response model, the CREEP user sub-routine was used to implement the modified K-R creep model as discussed in Chapter 4.

Calculation of the burnthrough time was implemented into the Abaqus framework via the USDFLD user sub-routine. Three solution dependent variables (SDVs) were used to fully implement the burnthrough model. In the Abaqus environment, SDVs are an integration point variable that is calculated by the algorithm specified within the USDFLD routine. The use of SDVs to monitor burnthrough states was used for two main reasons. First, SDVs allow for seamless integration of the burnthrough variables in the Abaqus environment's post-process visualization tools. That is, burnthrough variables can be viewed in the Abaqus post-processor alongside any other integration point or nodal result tensor. Second, the USDFLD routine allows for the SDVs to be read by the Abaqus solver as field variables. This allows for material property definitions that are dependent on SDV values. This combination of features allowed for successful integration of the burnthrough methodology without the need for development of user elements or materials.

The first SDV used in the mechanical models tracked the progression of the life fraction as defined by Eq. (4). This particular SDV was also used in the user CREEP routine to calculate the instantaneous creep strain increment according to Eq. (19). The second and third SDVs were implemented as representative Boolean variables to define burnthrough via the two mechanisms discussed in Chapter 3. The material melting SDV was triggered by integration point temperatures in excess of 633°C as discussed in Chapter 3. The creep rupture SDV was triggered by life fraction values in excess of 0.995. Although theoretical rupture does not occur until life fractions reach a value of one, life fractions were truncated to 0.995. This was done because creep strain increments approach infinite values as the life fraction approaches one and excessive creep strain increment calculations causes model instability. SDV dependent material properties were used to implement a pseudo element deletion feature into the mechanical models by reducing material stiffness by several orders of magnitude once burnthrough has been achieved.

Mechanical boundary conditions were applied to the model to mimic experimental conditions. For models of experiments involving the propane jet burner, plates were supported along edges corresponding to the pressed ceramic fiber board insulation that formed the supportive surfaces. For models of experiments utilizing the propane sand burner, point boundary conditions were used to mimic the screw tips used to support the test articles during experiments. For all mechanical models, gravitational forces on the plate were prescribed using the Abaqus environments gravity feature along with the specified material density. This feature uses the specified gravitational force (9.81 m/s^2 used here) and the defined material density to calculate corresponding volumetric loads corresponding to each node in the analysis using a tributary volume approach. Plate temperatures calculated in the thermal models were prescribed to geometries in the mechanical models via predefined fields. Because different meshing schemes were used in the thermal and mechanical models, mesh incompatible mapping was used to transfer temperatures to the mechanical model. This mapping technique uses linear interpolation based on thermal and mechanical model nodal locations as well as analysis timesteps.

All of the mechanical models were meshed using fully integrated solid quadratic elements (C3D20). Initial models used 5 elements through the plate thickness. The expected complexity of the through thickness stress field did not warrant this degree of mesh resolution. However, this resolution was necessary to provide insight into the through thickness propagation of the

burnthrough state. The effects of through thickness element density on burnthrough time convergence was studied. Burnthrough time convergence was found to occur at through thickness densities above 2 elements. Because of this, later models were conducted using 3 elements in the through thickness direction as this accurately captured the burnthrough rupture phenomenon while minimizing computational costs. In-plane meshes densities were biased towards the center of the plate where burnthrough was expected to occur. Specific densities were selected to maintain an element aspect ratio of 1:1 between the in-plane and through thickness directions and the plate center. Initial modeling was conducted with element aspect ratios of 1:5 at the plate edges. The effects of element aspect ratio at the plate edges on the stress response at the plate center were investigated. It was found that the burnthrough location stress response was insensitive to edge element aspect ratios. This led to increasing the edge element aspect ratio to 1:10 for final models. Figure 55 shows a typical mesh for the burnthrough benchmarking models.

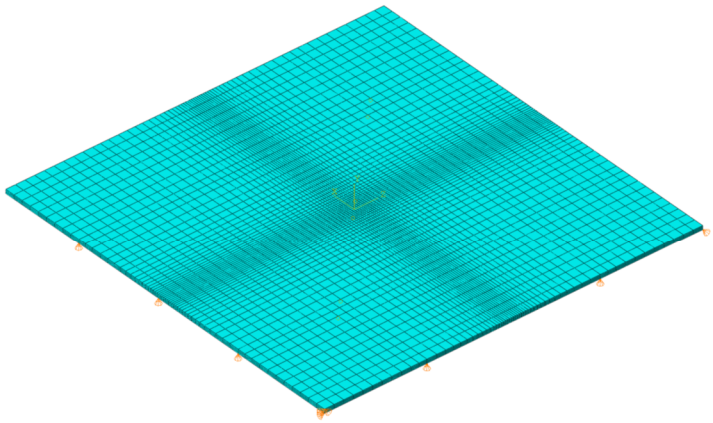

Figure 55. Sample mesh for mechanical FE model of 3.18 mm thick horizontally oriented plate.

6.3 Benchmark Model Results

6.3.1 Jet Burner Exposures

A comparison of experimentally measured burnthrough times and those calculated from the FE models is provided in Table 10 for plates exposed to the propane jet burner. For all of the jet burner exposures, the material melting mechanism was experimentally observed and predicted by the FE models. Additionally, the occurrence of burnthrough was accurately modeled for all of the propane jet burner exposures except for a single case where the predicted steady state temperature was 630°C. This provides an accuracy of burnthrough occurrence of over 90% within the experimental parameters used in this study. Finally, burnthrough times predicted by the FE model for these exposures are generally within 20% of experimental results.

Table 10. Comparison of experimentally observed and numerically calculated burnthrough times for plates exposed to propane jet burner.

Plate Orientation	Thickness (mm)	HRR (kW)	Distance (m)	Exp. Burnthrough		Model Burnthrough	
				Mechanism	Time (s)	Mechanism	Time (s)
Vertical	0.79	20	0.2	Melting	44*	Melting	43
	0.79	20	0.25	Melting	60*	Melting	52
	0.79	20	0.3	Melting	75	Melting	73
	1.58	20	0.2	Melting	116	Melting	84
	1.58	20	0.25	Melting	138†	Melting	98
	3.18	30	0.15	Melting	236†	Melting	259
	3.18	20	0.15	No Burnthrough		No Burnthrough	
	3.18	20	0.2	No Burnthrough		No Burnthrough	
	3.18	20	0.25	No Burnthrough		No Burnthrough	
Horizontal	0.79	20	0.2	Melting	41	Melting	36
	0.79	20	0.25	Melting	52	No Burnthrough	
	1.58	30	0.15	Melting	61	Melting	51
	1.58	20	0.15	Melting	108	Melting	90
	1.58	20	0.2	Melting	131	Melting	131
	3.18	30	0.15	Melting	143	Melting	154
	6.35	30	0.15	No Burnthrough		No Burnthrough	

*taken from average of multiple tests

†taken from average of multiple structural loads

In order to gain confidence in the burnthrough model's ability to accurately predict both the occurrence of burnthrough, model results were compared to experimentally measured data from Chapter 2. This additionally helped to investigate the origin of differences in the measured and calculated burnthrough times. Since the thermo-mechanical FE models were conducted sequentially, temperature results from the thermal FE models were first compared to experimental data. Figure 56 contains a sample comparison of full-field temperature map from experimental data and FE model at burnthrough for a 3.18 mm thick plate exposed to a 30 kW flame from the propane jet burner at 0.15 m. Full-field temperature trends from TDIC measurements and thermal FE models are in good agreement. Spatial temperature gradients are nominally radially symmetric with the exception of edge effects in both experimental measurement and model prediction. A comparison of the temperature response of the burnthrough site for vertically oriented plates exposed to the propane jet burner is seen in Figure 57. The same comparison is seen in Figure 58 for horizontally oriented plates. In general, transient thermal responses calculated from the FE model are within 20°C of experimental values while calculated steady state temperatures are generally within 10°C.

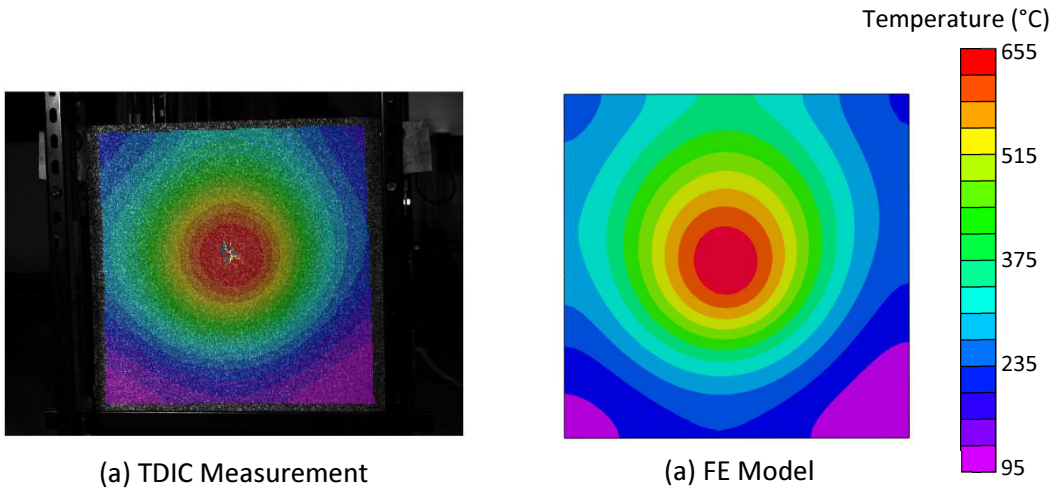

Figure 56. Comparison of full-field temperature measurement of 3.18 mm thick vertically oriented plate exposed to propane jet burner.

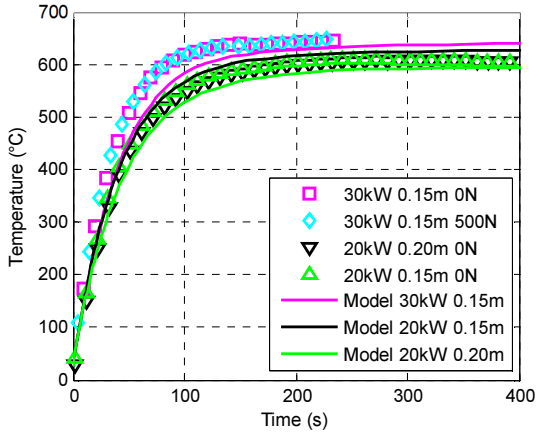

(a) 3.18mm thick plate

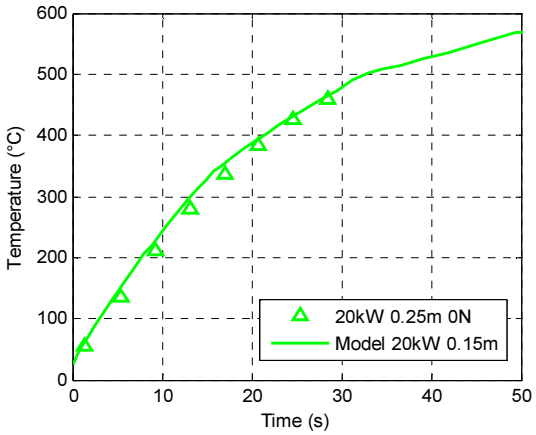

(b) 1.58mm thick plate

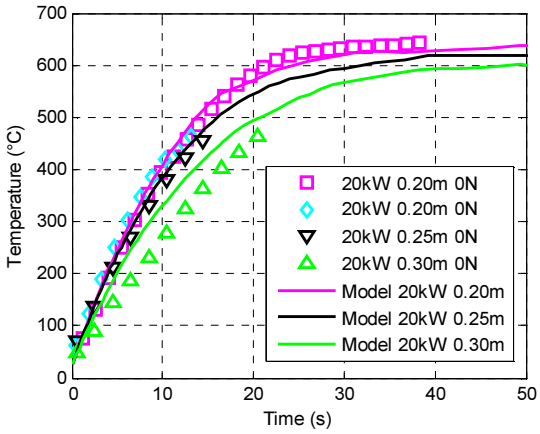

(c) 0.79mm thick plate

Figure 57. Comparison of temperature response at burnthrough site for vertically oriented plates exposed to the propane jet burner.

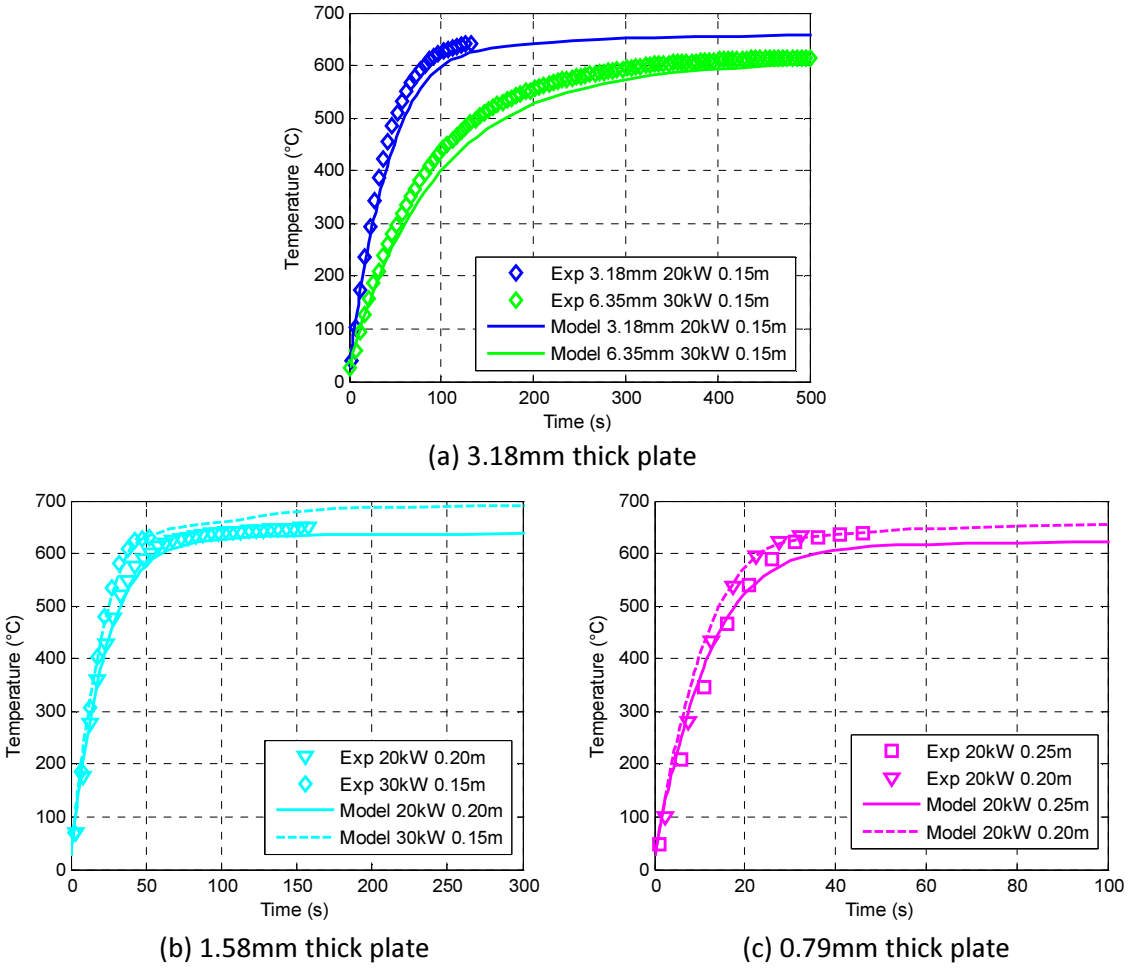

Figure 58. Comparison of temperature response at burnthrough site for horizontally oriented plates exposed to propane jet burner.

A comparison of the out-of-plane displacement results from experiments and FE models is shown in Figures 59-61. Figure 59 contains a sample comparison of full-field out-of-plane deflection from DIC measurement and FE model for a 3.18 mm thick plate exposed to a 30 kW flame at a burner distance of 0.15 m under a 500 N compressive load. Spatial trends between the experiment and model are in good agreement. The deflection of the burnthrough site is seen in Figure 60 for experiments and models with and without applied structural load. FE models generally under-predicted experimental data by 10% through the thermal transient region remained within 10% until the occurrence of burnthrough. The FE model was not able to predict the out-of-plane deflection behavior at the plate edges as well as at the plate center as seen in the displacement profiles in Figure 61. However, the spatial displacement trends are accurately predicted by the FE models.

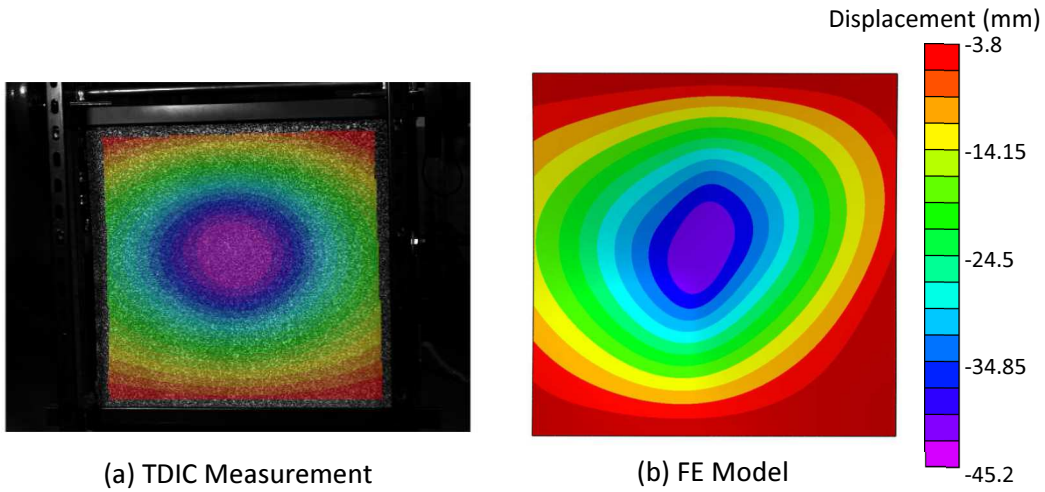

Figure 59. Comparison of full-field out-of-plane deflection of 3.18 mm thick vertically oriented plate under 500 N compressive load and exposed to propane jet burner.

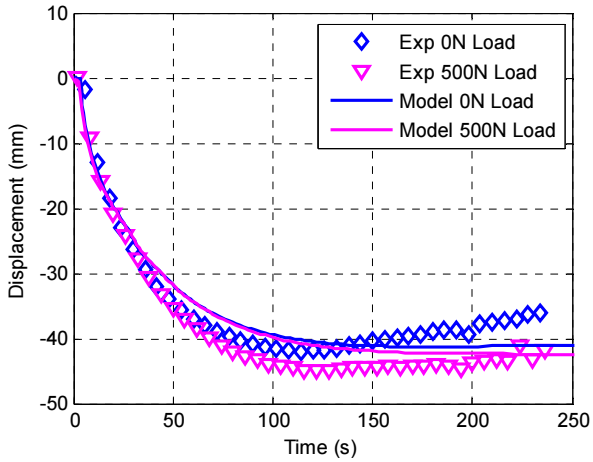

Figure 60. Experimental and numerical burnthrough location out-of-plane displacement of 3.18 mm thick vertically oriented plate exposed to propane jet burner and under multiple compressive loads.

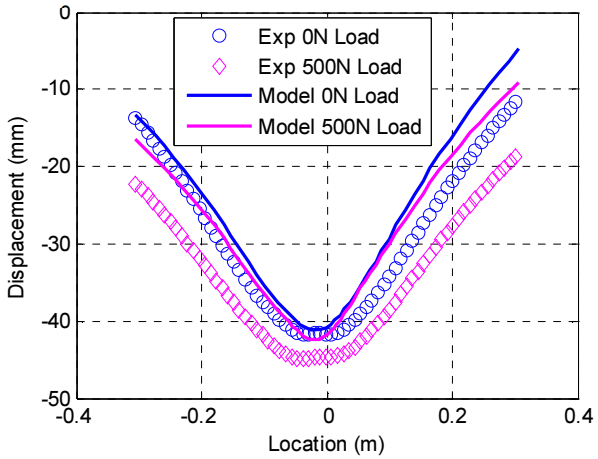

Figure 61. Experimental and numerical out-of-plane displacement profiles at burnthrough for a 3.18 mm thick vertically oriented plate exposed to propane jet burner and under multiple compressive loads.

6.3.2 Sand Burner Exposures

Table 11 contains a comparison of burnthrough times from FE models and experimental observation to plates exposed to the propane sand burner. For all of the test parameters, the burnthrough model was successfully able to model the occurrence of burnthrough. However, the vertically oriented plate model did predict burnthrough via creep rupture while experimental observation suggested burnthrough occurred via plate melting. Burnthrough times from the FE model were generally within 40% of experimental observation.

Table 11. Comparison of experimentally observed and numerically calculated burnthrough times for plates exposed to propane sand burner.

Plate Orientation	Thickness (mm)	HRR (kW)	Exp. Burnthrough		Model Burnthrough	
			Mechanism	Time (s)	Mechanism	Time
Vertical	0.79	70	Melting	315	Rupture	291
	0.79†	70	No Burnthrough		No Burnthrough	
	0.79†	80	No Burnthrough		No Burnthrough	
Horizontal	1.58	30	No Burnthrough		No Burnthrough	
	1.58	40	No Burnthrough		No Burnthrough	
	1.58	50	Rupture	281*	Rupture	355
	1.58	60	Rupture	203	Rupture	323
	1.58	70	Rupture	198	Rupture	239
	3.18	50	Rupture	467*	Rupture	643
	3.18	60	Rupture	419	Rupture	541
	3.18	70	Rupture	439	Rupture	395
	6.35	110	Rupture	687	Rupture	670

†unexposed side of plate painted with high emissivity paint

*taken from average of multiple tests

Because the surface heat fluxes generated by the propane sand burner were so low, only select location temperature measurements were obtained because the unexposed surface of the plate needed to be left unpainted to minimize thermal losses as discussed in Chapter 2. This meant that only select thermal validation measurements and no intermediate mechanical validation measurements could be obtained for experiments where burnthrough occurred. A comparison of the thermal validation measurements near the burnthrough location and temperatures obtained from the thermal FE model are seen in Figure 62 for both horizontally and vertically oriented plates. This comparison includes thermal data from experiments where burnthrough was not achieved. The FE models are generally within 20°C of experimental measurements. However, the measured and observed temperature fluctuations are higher than exposures from the propane jet burner due to the nature of the buoyant flame from the propane sand burner.

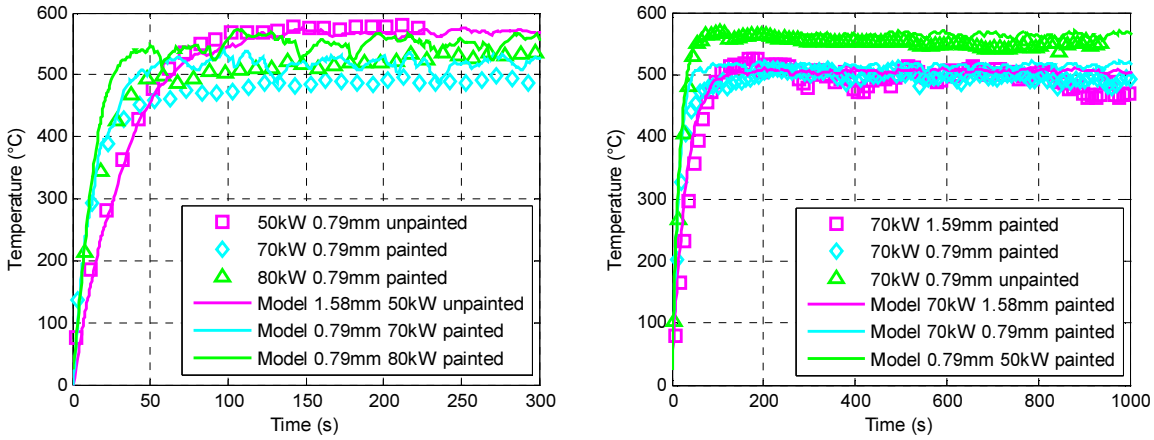

(a) Vertically oriented plates (b) Horizontally oriented plates

Figure 62. Comparison of experimental and numerical peak temperature measurements for plates exposed to propane sand burner.

6.4 Benchmark Model Discussion

For exposures to both the propane jet and sand burners, the implementation of the heat flux mapping methodology allowed for thermal predictions within 20°C in the transient region and 10°C in the steady state region. It was discussed in Section 5.5 that error in the convection heat transfer coefficient is a significant contributor to error in the calculated surface heat flux. Using the same propagation of error analysis shown in Eq. (29), the effect of error in the convective heat transfer coefficient on the surface heat flux can be calculated as

$$\epsilon_{q"} = \frac{dq"}{dh}\epsilon_h = \epsilon_h(T_{SS304} - T_0) \tag{41}$$

where T_{SS304} is the instantaneous temperature of the discrete element of the SS304 plate used to generate the heat flux map. Note that this only accounts for errors in the exposed surface as the natural convection correlations should more accurately capture the unexposed surface convection. Applying the same approach to the heat transfer calculation, the effect of errors from the applied heat flux and convective losses can be calculated as

$$\epsilon_{T_{AA6061}} = \sqrt{\left(\frac{dT}{dq"}\right)^2 \epsilon_{q"}^2 + \left(\frac{dT}{dh}\right)^2 \epsilon_h^2} \tag{42}$$

By combining Eqs. (41) and (42) the an equation can be calculated for the error in the modeled temperature due to the temperatures of the SS304 and AA6061 plates propagated through the convection heat transfer coefficient.

$$\epsilon_{T_{AA6061}} = \sqrt{\epsilon_h^2[(T_{SS304} - T_0)^2 - (T_{AA6061} - T_0)^2]} \quad (43)$$

Based on this equation, when temperatures of the plates used in the heat flux mapping and the predicted temperature of the plate are identical, then the bias errors propagated through the convection heat transfer coefficient are nullified. However, under identical exposures, AA6061 will heat faster than SS304 because of its lower specific heat capacity. This creates an error based on the temperature differential between the heat flux mapping and the actual burnthrough model. Because of this, errors are higher in the transient region of the thermal model as observed in Figure 57 and Figure 58 for models of the propane jet burner exposures. Thermal responses to the propane sand burner already vary more due to the fire dynamics which increases the test to test uncertainty of the thermal response.

Model predictions of the mechanical response of plates exposed to the propane jet burner agree well with experimental measurements. Out-of-plane deflection measured during burnthrough experiments is generally 10% larger than deflections calculated in the FE models. There are two reasons for these discrepancies. First, the models do not include the effects of any imperfection present in the plates. Any imperfection present will be magnified as the plates are heated and become less stiff. This is also why the predicted difference in out-of-plane deflection between plates with and without structural compressive loads is smaller than experimentally observed. Under buckling loads, initial imperfections are magnified through second order geometric effects in that they create small bending moments which, in turn, create more deflection. This is the cause of discrepancies in the displacement trends near the plate edges seen in Figure 61. The second main reason for difference between the observed and modeled mechanical behavior is the idealization of boundary conditions. Although plates were supported using a nominal pinned boundary condition, plates were only supported by compressed ceramic fiber board during experiments. This ceramic fiber board is not designed to support any structural load and permanently crushes under relatively small forces. This can cause additional out-of-plane deflection through the same second order geometric mechanism as the plates' imperfections. Additionally, it is seen in Figure 60 that the measured out-of-plane displacement of the burnthrough location begins to increase when approaching burnthrough. This is because the force exerted on the plate from the flow of hot gases from the jet burner. The mechanical FE model

does not include this and, therefore, deflections at the burnthrough location continue to increase for the entirety of the model.

The combination of the melting and creep rupture burnthrough criteria was able to accurately capture the occurrence of burnthrough for over 95% of experiments, including experiments where burnthrough was not achieved. Typical temperature threshold burnthrough models would not have accurately been able to capture this. Table 12 contains burnthrough times predicted by a temperature threshold model at a nominal material solidus temperature of 585°C for select experiments using the propane jet and sand burners [71]. For propane jet burner tests, this basic model is highly conservative for every test case including multiple cases where the model predicts burnthrough when it was observed. In contrast, the model is unconservative for experiments involving the propane sand burner where it does not predict burnthrough for experiments where it is observed. Including all tests, the basic criteria only accurately predicts burnthrough occurrence for 60% of test cases. Utilizing the melting and creep rupture criteria developed through this research, accurate burnthrough occurrence in the models increases to nearly 95%. Additionally, burnthrough times where material melting does occur using an experimentally measured melting temperature provides significantly more accurate results. Burnthrough times when rupture occurs are also more accurately modeled using the rupture criteria as this allows for rupture predictions to occur in the thermal steady state region in which it was experimentally observed.

Table 12. Comparison of experimentally observed burnthrough times to basic 585℃ temperature threshold model.

Burner Type	Plate Orientation	Thickness (mm)	HRR (kW)	Distance (m)	Exp. Burnthrough Time (s)	Temperature Treshold Time (s)
Jet Burner	Vertical	0.79	20	0.3	75	45
		1.58	20	0.2	116	36
		3.18	30	0.15	236	75
		3.18	20	0.15	No Burnthrough	136
	Horizontal	1.58	20	0.2	131	61
		3.18	30	0.15	143	102
		6.35	30	0.15	No Burnthrough	618
Sand Burner	Vertical	0.79	70	NA	315	No Burnthrough
		0.79	70	NA	No Burnthrough	No Burnthrough
	Horizontal	1.58	50	NA	281	No Burnthrough
		1.58	70	NA	198	71
		3.18	50	NA	467	No Burnthrough
		3.18	70	NA	439	190

Using the FE model results, the evolution of the life fraction, temperature, and stress response of the burnthrough location can be studied to gain a better understanding of the creep rupture burnthrough phenomenon. Figure 63 contains overlaid responses of each of these three variables for a horizontally oriented plate exposed to the propane sand burner. Before the start of exposure, plate stresses are approximately 0.5 MPa to 2 MPa depending on the plate geometry. Once heating begins, a temporary increase in stress occurs reaching values between 20 MPa and 80 MPa. This increase in stress is caused by the local thermal strains at the burnthrough site in conjunction with confinement created by the plate edges which do not heat as fast. During this time, plate temperatures are not high enough to cause significant evolution of the material life fraction towards a burnthrough state. Once the burnthrough site reaches high enough temperatures, the high stresses are relaxed due to increasing amounts of creep strain. Also at these temperatures, significant life fraction evolution begins.

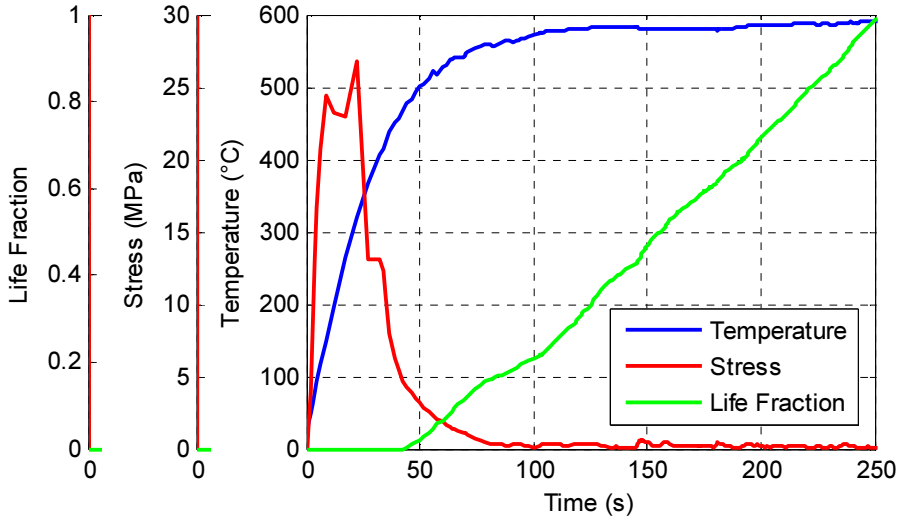

Figure 63. Temperature, stress, and life fraction evolution for a 1.58 mm thick horizontally oriented plate exposed to a 70 kW fire from a propane sand burner.

This understanding of the relationships between temperature, stress, and life fraction evolution can be used to understand the effects of physical and exposure parameters on experimental and numerical burnthrough times. To investigate the effects of fire repeatability on the numerical solution, multiple FE simulations were conducted for a 1.58 mm thick horizontally oriented plate exposed to a 60 kW fire from the propane sand burner. Identical parameters were used for all of the models except for three different measured heat flux maps measured from 3 separate 60 kW fires and a time-averaged heat flux map. While each heat flux map is nominally identical, fire

dynamic repeatability resulted in local heat fluxes that vary up to 15%. The life fraction evolution for each of these models is seen in Figure 64. The thermal response for each of these models was within the variation seen in the steady state temperatures of all the plates exposed to propane sand burner. However, the average temperature differentials of 10-15°C between tests resulted in burnthrough times that varied by up to 50%. This is the primary reason for developing and implementing the full-field heat flux mapping methodology into the burnthrough validation models. Additionally, this supports that although burnthrough times obtained from the models can differ from experimentally observed values by up to 50%, this is within the test to test repeatability expected from the burnthrough models based on the heat flux maps used in the thermal models.

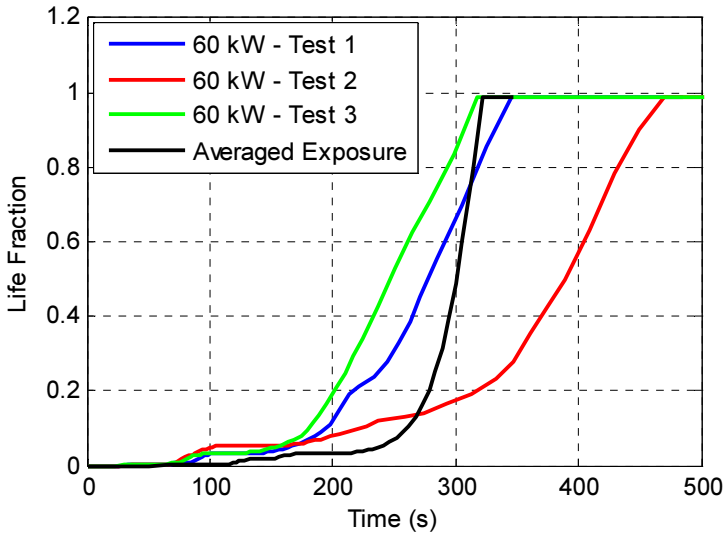

Figure 64. Life fraction evolution for a 1.58 mm horizontally oriented plate exposed to $60kW$ fires from a propane sand burner. Each model utilizes a different heat flux map from nominally identical fires.

The effects of the applied structural load on the burnthrough site stress response were also investigated using the FE models. Figure 65 contains the stress response of the burnthrough site for 3.18 mm thick plates with and without and applied structural load. The difference in initial stress state can be seen at t=0 s. Like the stress response in Figure 63, the stress of plates with and without load increase during initial heating to stresses within 5% of each other. After 150 s, the stresses in the structurally loaded plate have relaxed to nearly identical values to those from the unloaded plate. This suggests that predicted burnthrough time is insensitive to the applied structural loads and mechanical boundary conditions of the plate. Instead, burnthrough time is more dependent on plate the exposure parameters and plate geometry.

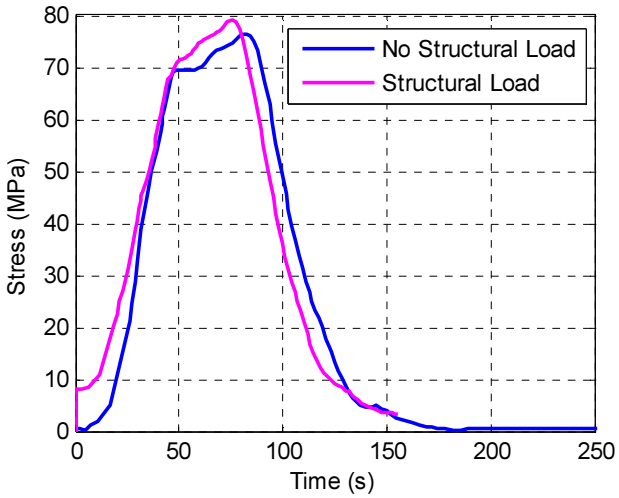

Figure 65. Burnthrough site stress evolution of 3.18 mm thick horizontally oriented plates with and without applied structural load.

6.5 Burnthrough Model Conclusions

Numerical models of both the melting and creep rupture burnthrough mechanisms developed in Chapter 3 were implemented into sequentially coupled thermo-mechanical FE models. FE models were used to numerically calculate predicted burnthrough times for the experiments conducted during this research. These models utilized the heat flux mapping methodology discussed in Chapter 5 to apply temporally and spatially varying heat fluxes to the thermal models. Although it was seen in Chapter 5 that errors in the convective heat transfer coefficient generated large errors in measured heat fluxes, these errors were mitigated by utilizing the same convective heat transfer coefficient in both the inverse heat transfer analysis and the thermal FE model. Because of this, temperature predictions from the thermal models were within 20°C in the transient region and 10°C in the steady state region for plates exposed to the propane jet burner. Models of plates exposed to the propane sand burner were within 20°C in both the transient and steady state regions.

Using the melting and rupture mechanism models, the FE model was able to accurately predict the occurrence of burnthrough for nearly 95% of experimental data obtained during this study. This is a significant improvement over traditional temperature threshold models which only accurately predicted burnthrough occurrence for 60% of experiments. Burnthrough times from the material melting mechanism that utilized a melting temperature of 633°C were calculated to be within 20% of experimental values. Burnthrough times from the creep rupture mechanism were within 50% of experimental values. By numerically investigating the temperature, stress, and life fraction

evolution response of the burnthrough locations, much of the uncertainty in the calculated rupture time was attributed to uncertainty in the thermal response of the plate. This uncertainty is due to the natural randomness of the fire dynamics from the propane sand burner.

Chapter 7: Design Rules for Burnthrough

Once the burnthrough methodology was benchmarked against the experimental data as discussed in the previous chapter, a set of simplified burnthrough relationships was developed. These simplified relationships were developed for a relatively simple and fast implementation that can be utilized via spreadsheet calculation in a design setting as well as into low spatial resolution, large scale thermo-structural models where the stress and temperature evolution of a burnthrough site cannot be solve through FE analysis as done during this research.

To develop these designs rules, a series of thermo-structural models were created. These models were used as basic exposure scenarios to calibrate fitting parameters for both the melting and creep rupture burnthrough mechanisms. These models were developed for square plates with lengths ranging from 0.3 m to 1.2 m in 0.3 m increments. Plate thicknesses ranging from 0.79 mm to 6.35 mm were used for these models. Exposure heat fluxes were applied to these models via a radially symmetric Gaussian function. These exposures we classified using two variables: peak heat flux and heat flux radius. The heat flux radius was defined as the distance between the location of the peak heat flux and a point where the applied heat flux was half of the peak heat flux. A generalized heat flux profile is shown in Figure 66. Peak heat fluxes of 50 kW/m^2 to 90 kW/m^2 were used in the calibration models to capture both the melting and creep rupture burnthrough mechanisms. Exposure radii used in the calibration models ranged from 0.1 m to uniform exposures.

Convection and radiation thermal boundary conditions were modeled on both the exposed and unexposed sides of the plate. The same constant convective heat transfer coefficient of 10.1 W/m^2K as calculated in Section 6.2.1 was used in these models on both the exposed and unexposed surfaces. Additionally, a surface emissivity of 0.95 was used for both surfaces. Like the burnthrough validation models discussed in the previous chapter, these models utilized fully integrated quadratic solid elements (C3D20). The models were seeded with three elements though the thickness. In plane seeds were biased towards the plate center such that element aspect ratios were 1:1:1 at the center and 1:10:10 at the plate corners. Because the plate and exposure exhibit two planes of symmetry, only one quarter of the plates were modeled in these simulations to reduce

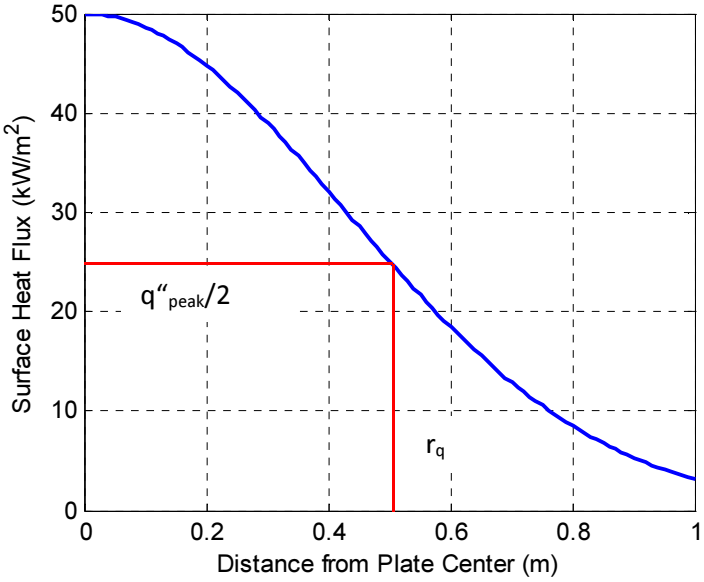

Figure 66. Radially symmetric heat flux profile used in development of burnthrough design rules.

computational costs. Like the burnthrough validation models, temperature dependent thermal and mechanical material properties were used in all of these basic exposure flat plate models.

Once developed, these simplified design rules for each of the burnthrough mechanisms were benchmarked against burnthrough data acquired both through numerical simulation as described in the previous chapter as well as experiments discussed in Chapter 2. The first benchmark comparison was against the simplified exposure models used to develop and calibrate the design rules. The primary purpose of this comparison was to determine the loss of accuracy in the burnthrough time predictions solely due to the numerical simplifications used to describe the burnthrough mechanisms. This would provide a best case scenario for accuracy of the design rules.

Next, design rules were benchmarked against thermo-structural models of 1.2 m by 1.2 m stiffened aluminum panels. The panel geometry was developed to be symmetric in two directions so that only one quarter of the panel needed to be modeled. The panel geometry used in these models is seen in Figure 67. As can be seen, a set of 3 50 mm deep stiffeners were spaced equally across the panel. Because of the symmetry, only two of the stiffeners are seen in the quarter of the panel model. Additionally a 50 mm deep stiffener was placed around the perimeter of the plate. The plate and all of the stiffeners were modeled as 6.35 mm thick. For all of the stiffened panel models,

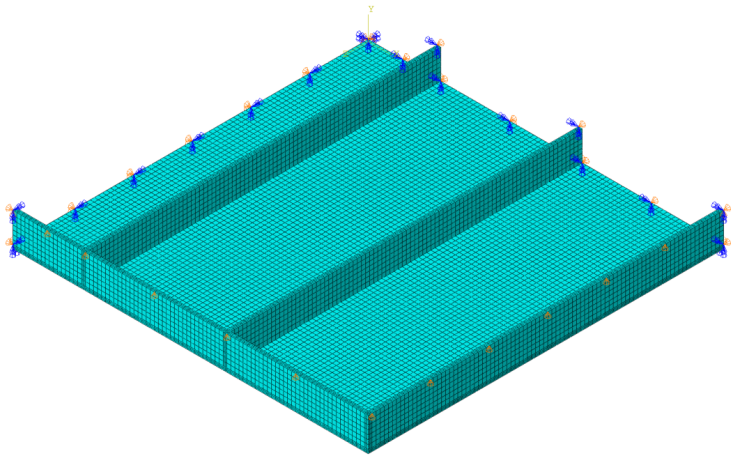

Figure 67. Stiffened panel geometry, mesh, and boundary conditions.

radially symmetric exposures with an exposure radius of 0.6 m as calculated by the above method were applied to the stiffened side of the plate. Convection and radiation thermal boundary conditions were applied to both the exposed and unexposed sides of the stiffened plates in the same manner as the plate models described above. Mechanically, the stiffened plates were simply supported around the perimeter of the plate along the base of the perimeter stiffener. Peak heat fluxes were selected to investigate predictions of both the melting and creep rupture mechanisms as discussed in Chapter 3. Peak heat fluxes of 85 kW/m^2 to 100 kW/m^2 were selected to capture the melting mechanism and heat fluxes of 55 kW/m^2 to 80 kW/m^2 were selected for the creep rupture mechanism.

Thermal models of the stiffened plate were assembled using solid quadratic heat transfer elements (DC3D20). Like the flat plate models, only a single element was used through the thickness of the plate and stiffeners because no significant thermal gradient was expected in the through thickness direction and heat transfer elements do not exhibit the same compliance difficulties due to element aspect ratio as mechanical elements. An in-plane seed of 15 mm was used for the thermal models. Mechanical models utilized fully integrated solid quadratic elements (C3D20) just like the flat plate models. For mechanical models, 3 elements were used through the thickness of the plate and stiffeners and in plane meshes were seeded at 7 mm. This provided a maximum element aspect ratio of approximately 3:1. Like all other FE models, temperature dependent thermal and mechanical material properties were used in the stiffened plate models.

Finally, design rules were used to predict the burnthrough time of experiments discussed in Chapter 2. Burnthrough times of horizontally and vertically oriented plates exposed to the propane jet burner were compared to design rule calculations for the material melting burnthrough mechanism. Additionally, burnthrough times of horizontally oriented plates exposed to the propane sand burner were compared to design rule calculations for the creep rupture burnthrough mechanism. For all of the design equation calculations, a convection heat transfer coefficient of 10.1 W/m^{2}K was used on both the exposed and unexposed sides. Surface emissivity for models of burnthrough experiments matched experimental conditions with 0.95 used for surfaces painted with high emissivity paint and 0.5 used for surfaces left bare. Because the design rules were developed using plates that were simply supported around the entire perimeter, models of burnthrough experiments inherently have the same support conditions.

7.1 Melting Mechanism Rules

7.1.1 Melting Mechanism Rules Development

Analytical calculation of the burnthrough time via the melting mechanism was achieved through a lumped capacitance approach. The energy balance for uniform temperature plate can be expressed as

$$Q_0 + 2h\Delta^2(T_0 - T) + 2\varepsilon\sigma_{SB}\Delta^2(T_0^4 - T^4) = \rho V c_p \frac{\partial T}{\partial t} \tag{44}$$

where the convective and radiation boundary conditions are multiplied by two to represent boundary conditions for both the exposed and unexposed surfaces. This particular form of the energy balance does not have analytical solution for the transient temperature response. In order to develop an analytical solution, the radiation term of the equation was linearized as follows

$$q_0 + 2h(T_0 - T) + 2\varepsilon\sigma_{SB}(T_0^2 + T^2)(T_0 + T)(T_0 - T) = \rho\delta c_p \frac{\partial T}{\partial t} \tag{45}$$

and the linearized radiation coefficient was combined with the convection term to produce a solvable first order differential equation

$$q_0 + h_{eff}(T_0 - T) = \rho\delta c_p \frac{\partial T}{\partial t} \tag{46}$$

where

$$h_{eff} = 2(h + \varepsilon\sigma_{SB}(T_0^2 + T^2)(T_0 + T)) \tag{47}$$

here, the radiation boundary condition has been combined with the convective boundary condition to create an effective heat transfer coefficient. This effective coefficient includes the convective heat transfer coefficient added to a linearization of the radiation boundary condition. Figure 68 contains the linearized radiation coefficient with respect to temperature for a blackbody emitter. In this setting, h_{eff} is twice the sum of the convective and radiative heat transfer coefficients to account for losses from both the exposed and unexposed surfaces. Once the radiation boundary condition was linearized, an analytical solution for transient temperature response could be calculated from Eq. (46) using a separation of variables to be

$$T_{unif} = \frac{q_0}{h_{eff}}\left(1 - e^{-\frac{h_{eff}}{\rho\delta c_p}t}\right) + T_0 \tag{48}$$

where $h_{eff}/\rho\delta c_p$ is the exponential time constant.

The formulation of Eq. (44) assumed no lateral conduction losses in the plate. However, both burnthrough experimentation and modeling have shown that lateral conduction losses can significantly affect the burnthrough site temperature. To account for these losses, a modification factor was developed to calculate an altered temperature differential between ambient and steady state temperatures. The steady state temperature is found by taking the limit as t→∞ of Eq. (48).

$$T_{SS} = C_{LC}\frac{q_0}{h_{eff}} + T_0 \tag{49}$$

where C_{LC} is the lateral conduction modification factor. Based on Fourier's law, this lateral conduction modifier is a function of the radial temperature differential around the burnthrough initiation site. This temperature differential is a function of the fire diameter, peak heat flux, and plate thickness. It is important to note that the lateral conduction is also a function of material thermal conductivity, but that relationship was not developed here as AA6061 was the only material considered. Using a limit analysis, an exponential decay model for the lateral conduction modifier was developed as

$$C_{LC} = (1 - e^{-f(r_q, q'', \delta)}) \tag{50}$$

This form of the lateral conduction modifier will be a unity value as the exponential function goes to infinity and a zero value when the function goes to zero. To develop a form for the exponential function, a conceptual proportionality analysis was used. It was found that the lateral conduction

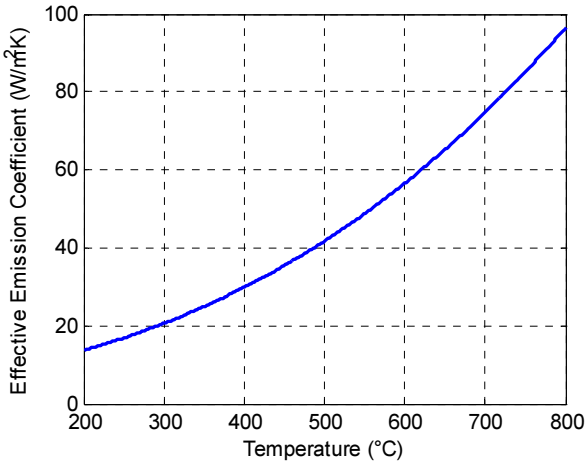

Figure 68. Linearized emissive boundary condition coefficient for blackbody radiation.

modifier should be directly proportional to the plate thickness and inversely proportional to the exposure radius and peak heat flux. To capture a uniform exposure, this relationship for the lateral conduction modifier approaches 1 when r_q approaches infinity. This results in the uniform steady state temperature obtained by taking the limit of Eq. (48) as t approaches infinity. Likewise, as the exposure radius approaches zero, the lateral conduction modifier also approaches zero which nullifies any exposure regardless of other exposure parameters. Thermal finite difference models of flat plates exposed radially symmetric heat fluxes as described in the previous section were used to determine the relationships for fire diameter, peak heat flux, and plate thickness. Steady state temperature was obtained from the thermal FE models for multiple heat fluxes, fire diameters, and plate thicknesses. This was compared to Eq. (49) using the lateral conduction modifier in Eq. (50). A non-linear regression analysis of FE model results was used to calculate lateral conduction modifier as

$$C_{LC} = \left(1 - e^{-0.00296 r_q \sqrt{\frac{q''}{\delta}}}\right) \tag{51}$$

where q'' is in units of W/m^2 and r_q and δ are in meters. It is important to note that this particular equation is only valid for AA6061 as the 0.00306 fitting parameter is a function of material conductivity. As previously stated, this relationship with material conductivity was not investigated because only AA6061 was considered. A comparison of steady state temperatures obtained from FE models and Eq. (49) is shown in the subsequent section. Finally, an explicit

analytical expression for burnthrough time via the material melting mechanism can be developed by rearranging Eq. (48) to be written in terms of the modified steady state temperature prediction

$$t_M = -\frac{\rho \delta c_p}{h_{eff}} \ln\left[1 - \frac{T_M - T_0}{T_{SS} - T_0}\right] \tag{52}$$

7.1.2 Melting Mechanism Design Rules Benchmarking

Melting time predictions as calculated by Eq. (52) were first compared to the model results for square plates exposed to the radially symmetric exposure described at the beginning of Chapter 7. Figure 69 contains a comparison of steady state temperatures obtained from thermal FE models and from Eq. (49) and the lateral conduction fitting parameter in Eq. (51). For uniform exposures, the predicted steady state temperatures match FE results within $3°C$. This high level of accuracy expected for uniform exposures because the uniform steady state temperature was solved for iteratively with the effective heat transfer coefficient. Then without any lateral conduction, the only difference between the analytical equation and the FE model is the small through-thickness temperature gradient. As the exposure radius is reduced below $0.4m$, errors from the lateral conduction fitting parameter become more prevalent. These errors occur because the lateral conduction away from burnthrough initiation site is only being represented by the simple exponential decay model of Eq. (51). While even the FE models are using an approximation of thermal conduction over the spatial discretization, it is much more accurate than the explicit formulation developed for the design rules. This causes errors in steady state temperatures

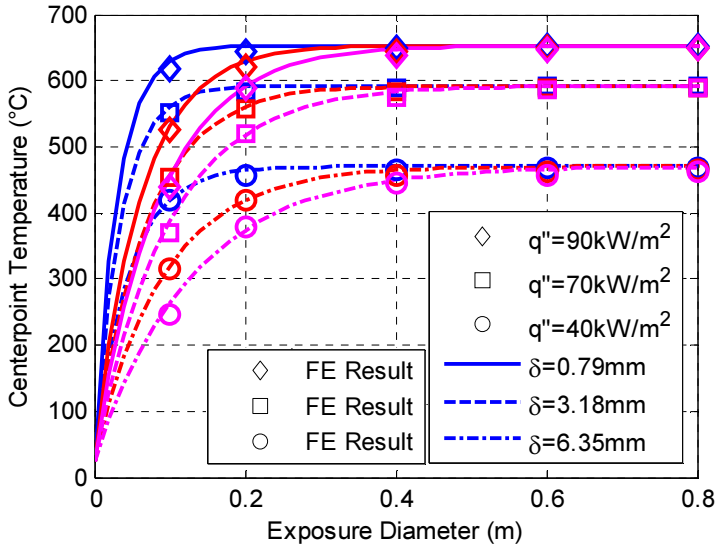

Figure 69. Comparison of steady state temperatures obtained from thermal FE simulation and developed design rule.

calculated from the analytical formulation up to 20°C. This error becomes larger with decreasing exposure radius because the in-plane temperature gradients are larger for smaller diameter exposures. Additionally at small exposure radii, higher temperature prediction errors were observed for thicker plates and higher heat fluxes. This is expected as lateral conduction heat fluxes are proportional to peak heat flux and plate thickness generating higher errors from the simple exponential decay model.

Figures 70 and 71 contain a comparison of the predicted melting times from FE analysis and from Eq. (52). Figure 70 contains this comparison is shown at a peak heat flux of 90 kW/m^2 for multiple exposure radii while Figure 71 contains the comparison at an exposure radius of 0.6 m for multiple peak heat fluxes. Both comparisons are for multiple plate thicknesses. It can be seen that the design equations generally under predict the melting times obtained via FE modeling. At high peak heat fluxes, the FE models and design equations appear to converge to the same burnthrough time. This is because at these higher heat fluxes, the transient temperature response of the plate up to burnthrough is highly linear as the energy into the plate from the applied exposure is significantly greater than the energy dissipating via the boundary conditions. The under prediction of melting time is exaggerated as the peak heat flux becomes lower. Opposite of high heat fluxes, the transient thermal response of the burnthrough site at lower heat fluxes becomes nonlinear as the predicted steady state temperature nears the material melting temperature. This nonlinearity causes an under prediction of burnthrough initiation time via the melting mechanism for lower heat fluxes as seen in Figure 70. Additionally, any errors in the prediction of the steady state temperature have a larger effect on the predicted melting time when the steady state temperature is near the melting temperature because of the reduced rate of temperature change with time near predicted steady state. In Figure 71 it can be seen that for a particular peak heat flux level, the design equations under predict the melting time by a constant value. In the case of a 90 kW/m^2 exposure, design equation predictions are approximately 20% less than results for FE analysis. This is true for all of the plate thicknesses analyzed in this research. Also, the minimum exposure radius necessary for material melting predicted by the design equations is also approximately 20% lower than FE results. This is because steady state temperatures calculated using Eq. (49) tend to slightly over predict FE models results as seen in Figure 69. This slight over prediction in temperature means that smaller exposure radii can still cause predicted steady state temperatures above material melting.

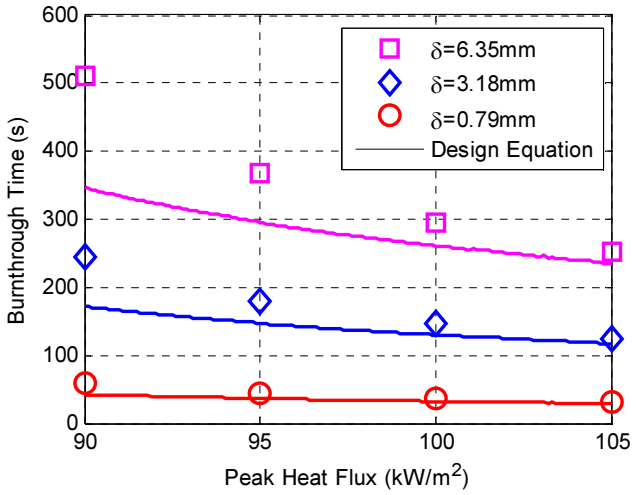

Figure 70. Comparison of burnthrough times via material melting mechanism from FE simulation and design rules for plate under exposure with radius of 0.6 m.

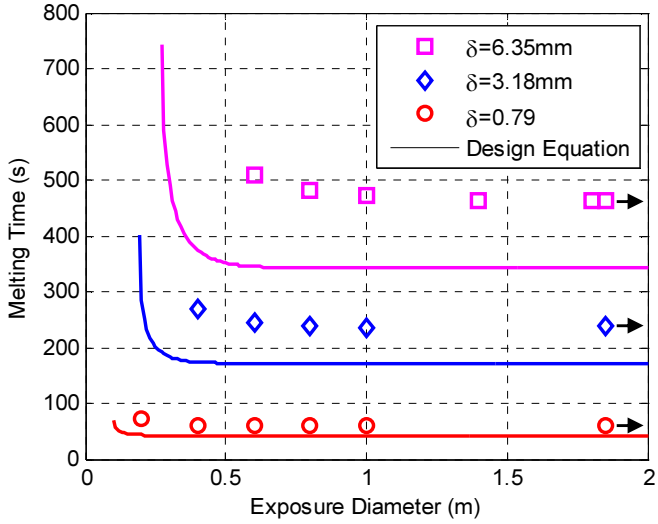

Figure 71. Comparison of burnthrough times via material melting mechanism from FE simulation and design rules for plate under 90 kW/m^2 peak exposure.

A comparison of predicted steady state temperatures obtained from Eq. (49) and FE modeling for the stiffened plate described at the beginning of Chapter 7 is shown in Figure 72. For all heat fluxes, the design equations under predict the steady state temperature obtained from FE analysis. This is expected because the stiffened side of the plate was exposed to the heat source. Because of this, the stiffeners increased the surface area of the exposure which increased the total energy into the plate. Because the stiffener temperatures were higher than the plate temperatures, the stiffeners heated the plate through conduction and raised the temperature of the burnthrough site. Figure 73 contains a comparison of the melting time for the design equations and FE modeling. Here, the design equations are able to predict the melting time to within 10%. The accuracy of the

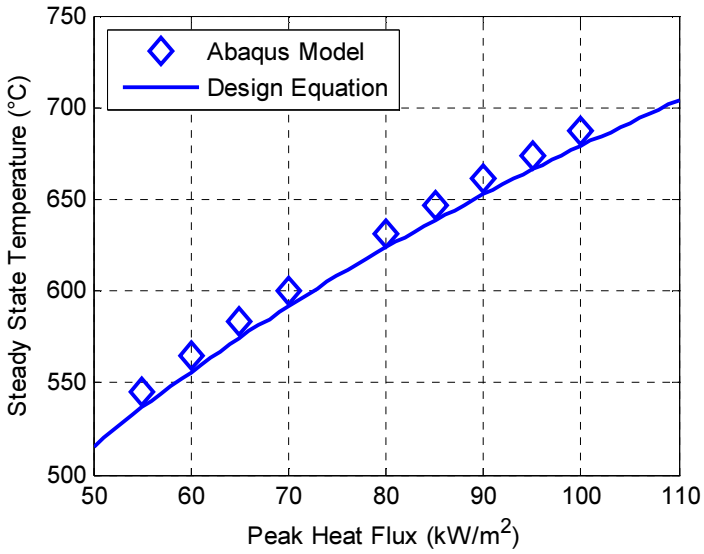

Figure 72. Steady temperature of stiffened panel geometry obtained from thermal FE simulation and design rules.

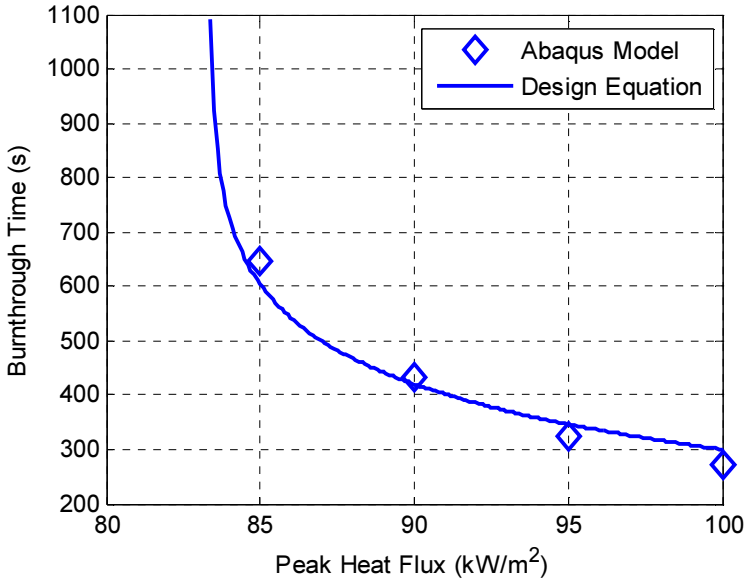

Figure 73. Burnthrough time from material melting of stiffened panel geometry obtained via FE simulation and design rules.

design equation is higher for the stiffened plate than the simple plates discussed above. This is because the under prediction of steady state temperature for the stiffened panels increased the melting time prediction. Since the design equations tend to under predict melting time for simple plates, this increase created a higher accuracy for the stiffened panels. However, if the design equations were compared to a stiffened plate where the unstiffened side was exposed to a heat

source, it is expected that the design equations would over predict burnthrough site temperature. This would results in a higher level of error in the predicted melting time.

Lastly, the design equations for material melting were used to predict melting times for the burnthrough experiments discussed in Chapter 2. In order to calculate predicted melting times, peak heat flux and exposure radius needed to be found for the heat fluxes applied to the plates in the burnthrough experiments. Peak heat fluxes were calculated by finding the maximum heat flux from the time averaged heat flux maps shown in Figures 48-51 in Section 6.2.1. To determine exposure radius, a horizontal section of the heat flux map was used. This section was taken at the height of the peak heat flux value. A nonlinear regression was used to determine an analytical representation of the heat flux profile in the form of a normal distribution. Exposure radii were calculated as the distance between the location of the peak heat flux and where the heat flux was half of the peak as discussed at the beginning of Chapter 7. Figure 74 contains a sample heat flux profile with the calculated exposure radius for a heat flux map from the propane jet and sand burners. As can be seen, the Gaussian representation is able to capture the flux profile for both types of burner with minimal errors.

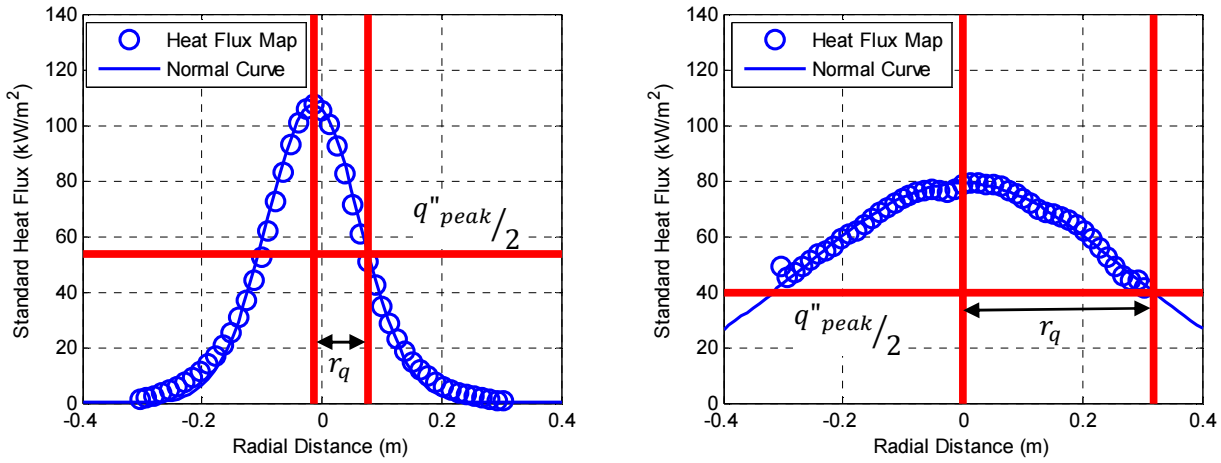

(a) Propane jet burner exposure (b) Propane sand burner exposure

Figure 74. Normalized heat flux fitting of propane sand and jet burner exposures.

Using the peak heat flux and exposure radius data, predictions of melting time were calculated using Eq. (52) for all of the experiments where material melting was observed. A comparison between experimental results and design equation results is seen in Table 13. The design equations are generally able to predict the experimentally observed melting time to within 25%. There is no

apparent trend of the design equations to over predict or under predict the experimental data. Although comparisons to FE results generally under predicted melting time, experimental uncertainty such as non-constant exposures and boundary condition uncertainty contribute to the more random nature of the differences between experimental melting times and those predicted using the design equations. The largest error occurred for the 6.35 mm thick plate where the design rules did not predict the occurrence of burnthrough. Instead, the predicted steady state temperature for this test was 4°C lower than the material melting. Errors in the prediction of burnthrough via melting when the predicted steady state temperature is near the material melting temperature threshold are expected and one of several motivations behind the development of the creep rupture mechanism model.

Table 13. Comparison of burnthrough times via the material melting mechanism from experimental observation and developed analytical design rule.

Plate Orientation	Thickness (mm)	HRR (kW)	Distance (m)	Peak Heat Flux (kW/m²)	Exposure Radius (m)	Time to Burnthrough (s)		
						Experiment	Design Rule	Difference (%)
Vertical	0.79	20	0.2	107.3	0.092	44	35	-20
	0.79	20	0.25	102.6	0.098	60	38	-37
	0.79	20	0.3	99.9	0.096	75	42	-44
	1.58	20	0.2	107.3	0.092	116	136	17
	1.58	20	0.25	102.6	0.098	138	167	21
	3.18	30	0.15	124.6	0.111	236	184	-22
Horizontal	0.79	20	0.2	108.1	0.095	41	33	-18
	0.79	20	0.25	98.9	0.088	52	49	-6
	1.58	30	0.15	113.5	0.111	61	70	14
	1.58	20	0.15	106.4	0.102	108	101	-7
	1.58	20	0.2	108.1	0.095	131	113	-14
	3.18	30	0.15	113.5	0.111	143	T_{SS}=628.5	NA

7.2 Creep Rupture Mechanism Rules

7.2.1 Creep Rupture Mechanism Rules Development

Design rules for the creep rupture mechanism are inherently more complex than the melting mechanism because the creep rupture mechanism requires the development of both thermal and mechanical predictions at the burnthrough site. These creep rupture mechanism design rules were conceptualized and calibrated based on observed temperature and stress response of thermo-structural models. Development of the creep rupture burnthrough mechanism design rules was based on Eq. (15). To predict the creep rupture time, accurate predictions of the material stress and temperature response at the burnthrough site are necessary.

Analytical expressions for the stress state evolution were developed based on predicted stress state from FE models. Figure 63 in Section 6.4 contains a stress, temperature, and life fraction evolution for a burnthrough site of a plate exposed to the propane sand burner. As previously discussed, an initial stress develops at this point due to the gravitational loads on the plate. The stress increases due to thermal strains and confinement until sufficient thermal energy is absorbed by the plate to implement creep straining of the material. This generally occurs at temperatures between 400°C and 500°C. At this point, creep relaxation reduces the stress to a near zero value. To predict this entire stress evolution, the response was split into two different regimes: steady-state room temperature stress prediction and stress relaxation prediction. It can be seen in Figure 63 that predicted evolution of the material life fraction does not begin to occur approximately until the material temperatures are in excess of 500°C which is similar to the threshold for the initiation of creep relaxation. Because of this, the calculation of creep rupture burnthrough time is calculated in two steps. First is the calculation of the time to creep relaxation initiation. Second is the calculation of the time for the life fraction to progress to a value of 1 after creep relaxation is initiated.

In order to predict the life fraction response, an approximation of the stress response at the burnthrough initiation site is necessary. The initial stress of the burnthrough site prior to thermal exposure was calculated using Kirchhoff plate theory. The Kirchhoff plate equations are valid for plates with small thickness to span ratios, but stiff enough to not undergo large deflections. These criteria are generally met for structural panels and Kirchhoff plate theory is widely used for analyzing structural plates. Westergaard [72] developed simplified approximations of bending moments based on Kirchhoff plate theory for simply supported rectangular plates under uniformly distributed load. Using this approximation with gravitational forces as the distributed load, the stress at the plate center can be calculated as

$$\sigma_{RT} = \frac{3\rho g \delta}{4(1+2\alpha)}\left(\frac{d}{\delta}\right)^2 \tag{53}$$

Where d is the shorter length of the plate and α is the aspect ratio of the shorter length to the longer length. For all of the analyses in the research, the plates are of equal sides making α=1. This approximation of the peak stress was derived neglecting the effects of Poisson's ratio. It is expected that Poisson effects will increase the stress at the plate center due to plane stress.

Therefore, this equation is expected to slightly under predict the peak stress calculated through FE analysis.

In order to develop a design equation for the creep relaxation initiation time, a consistent method for measuring this time from a FE model was necessary. As discussed in Section 6.4, stresses at the burnthrough site initially increase as the localized temperature at the site increases. However, since life fraction values do not significantly progress during this time, these stresses are being neglected in the design equations. Because of this, the creep relaxation initiation time was defined as the time at which the burnthrough site stress decreased below the initial stress state calculated by Eq. (53). Using this criteria, the relaxation initiation time from FE simulations of flat plates appears to be a function of both the thermal exposure and room temperature plate stresses. Predictions for the creep relaxation initiation time were calculated using a temperature threshold of 400°C combined with a linear dependence on the room temperature stress. The analytical form for the relaxation initiation time was developed by combining Eq. (52) where T_M is replaced with T_{relax} and Eq. (48) to yield

$$t_{relax} = \frac{D_1}{\sigma_{RT}} t_{T_{relax}} = -\frac{4D_1\delta^2 c_p}{gd^2 h_{eff}} \ln\left[1 - \frac{(T_{relax} - T_0)}{(T_{SS} - T_0)}\right] \tag{54}$$

where T_{relax} is equal to 400°C and h_{eff} is evaluated at the predicted steady state temperature of the plate calculated from Eq. (49). Additionally, the room temperature stress is normalized to the fitting parameter D_1 which has the same units as stress. This temperature corresponds to the stress state at which creep relaxation initiation occurs at exactly 400°C. The use of this temperature threshold also provides a minimum steady state temperature of 400°C at which the burnthrough calculation will predict the occurrence of burnthrough. For predicted steady state temperatures below 400°C, Eq. (54) will provide a time less than zero. Although burnthrough was not observed until temperatures exceeded 500°C, the predicted burnthrough times at temperatures between 400°C and 500°C will be on the order of tens to hundreds of hours as discussed in the subsequent sections which is significantly longer than typical fire exposures. This supports experimental observations that burnthrough was not observed these low of temperatures.

Beyond the creep relaxation initiation time, the life fraction evolution is calculated in same manner as the mechanical FE models. For this calculation, evolution of the plate stress at the burnthrough

site was derived using a simplified creep relaxation approach. Using a constant strain formulation, the stress relaxation behavior due to creep straining of a material was calculated as

$$\frac{1}{E}\frac{d\sigma}{dt} + \dot{\varepsilon}_{creep} = 0 \tag{55}$$

The modified K-R creep model derived in Chapter 4 was initially implemented into the creep relaxation model by taking the time derivative of Eq. (13) and inserting into Eq. (55) such that

$$\frac{1}{E}\frac{d\sigma}{dt} + A\sinh(B\sigma)^n e^{-Q/RT}(1 - t/t_r)^{1/\lambda - 1} = 0 \tag{56}$$

This produces a first order nonlinear ordinary differential equation that has no analytical solution. Because of this, the creep response of the material needs to be simplified to a form where an analytical equation can be obtained. The logical first step to simplifying the creep model is to remove the tertiary creep effects added to the secondary creep rate equation in the modified K-R model. However, the presence of the hyperbolic-sine term within the exponent *n* causes the solution to have no analytical form. To obtain an explicit form of the creep relaxation equation, the creep behavior of the material at temperatures above 500°C was simplified to a traditional power law relationship with an Arrhenius kinetics temperature dependence. Derivation of the power creep properties used for relaxation above 500°C is discussed in the subsequent section. Using this simplified creep law in the creep relaxation equation, a first order nonlinear differential equation is derived from Eq. (55) as

$$\frac{1}{E}\frac{d\sigma}{dt} + G\sigma^h e^{-Q/RT} = 0 \tag{57}$$

This equation has a closed form solution for the stress evolution as a function of time which can be obtained through a separation of variables and algebraic manipulation to be

$$\sigma = \frac{\sigma_i}{\left(GEe^{-Q/RT}(h-1)\sigma_i^{h-1}t+1\right)^{1/h-1}} \tag{58}$$

where for the case of the burnthrough prediction, σ_i is equal to the room temperature stress calculated from Eq. (53). Eq. (55) was derived based on the stress response for a material under constant total strain undergoing only elastic and creep deformations. However, the stress-strain response of the burnthrough initiation site is more complex as seen in the validation modeling of the burnthrough phenomenon from Chapter 6. At the burnthrough initiation site, the total strain in

the material is not constant. Thus, the creep response would not be expected to follow the exact behavior from this simplified creep relaxation model. Additionally, modeling efforts have shown that the stress response is dependent on exposure radius such that larger diameter fires produce lower stress relaxation rates while smaller diameter fires produce higher stress relaxation rate. To account for these increased complexities, two additional calibration factors were added to Eq. (58).

The first calibration factor was added to account for the difference in total strain response between the creep relaxation model and results from FE analysis. Because Eq. (55) is formulated using an initial elastic strain, the first calibration factor was added in replacement of the elastic modulus. The second calibration factor was added to account for the effects of exposure radius.

Figure 75 contains the time dependent stress response from FE models for varying exposure radii. These responses were taken from the simplified radially symmetric exposure models discussed at the start of this chapter. These particular stress responses are for 3.18 mm thick plates exposed to a 70 kW/m^2 peak heat flux. The stress response prior to the uniform exposure creep relaxation time varies widely. Although not shown in this plot, the stress at the burnthrough site for smaller diameter fires can increases during initial heating due to localized thermal expansion at the peak heat flux location and the confinement caused by the remainder of the plate as discussed in previous sections. However, because the temperatures are lower at these times, the life fraction does not progress making the burnthrough time insensitive to these stresses. Because of this, no

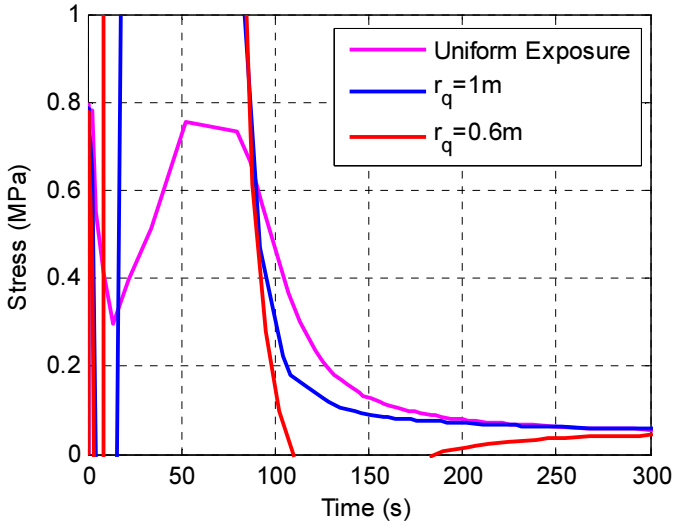

Figure 75. Burnthrough location stress response of plates under exposures with multiple exposure radii.

effort was made to predict the increased stress response at these low temperatures. It can be seen in Figure 75 that the time at which the stresses relax below the room temperature value is relatively unaffected by the exposure radius. This means that the relaxation initiation time prediction from Eq. (54) and the initial room temperature plate stress from Eq. (53) can be utilized for all exposure radii. Because exposure radius does not affect the life fraction evolution before creep relaxation initiation, the calibration factor for the effects of the exposure radius should be applied the first term of the denominator of Eq. (58) such that it only effects the stress relaxation rate. Applying the total strain and exposure radius calibration factors to the stress relaxation model in Eq. (58) yields

$$\sigma = \frac{\sigma_i}{\left[\frac{HGe^{-Q/RT(h-1)\sigma_i^{h-1}}}{f(r_q)}t+1\right]^{1/h-1}} \tag{59}$$

where H, and $f(r_q)$ are fitting parameters for the non-constant strain and localized exposures, respectively.

Using Eq. (59), an explicit formulation for the Larson-Miller parameter and then rupture time can be calculated. Using Eqs. (16) and (59), an explicit equation for the predicted rupture time was calculated as

$$LMP = C_1 \operatorname{atanh}\left[\frac{2}{\sigma_{ul}-\sigma_{ll}}\left(\frac{\sigma_i}{\left[\frac{HGe^{-Q/RT(h-1)\sigma_i^{h-1}}}{f(r_q)}t+1\right]^{1/h-1}} - \frac{\sigma_{ul}+\sigma_{ll}}{2}\right)\right] + C_2 \tag{60}$$

From this point, an explicit formulation for the rupture time as a function of time can be developed by combining Eqs. (15) and (60). To calculate the rupture time, the slope of the life fraction can be taken as the inverse of the instantaneous rupture time. That is

$$\frac{dL_f}{dt} = \frac{1}{t_r} \tag{61}$$

Combining Eqs. (15), (60), and (61) leads to explicit formulation for the time derivative of the life fraction. However, this explicit representation is not in an integrable form. Because of this, the time to burnthrough has to be calculated numerically using a discretized time step. Here, the burnthrough time is calculated from in the same form as Eq. (4). However, the discretized

calculation now becomes a simple calculation because of the explicit form of the slope of the life fraction given by Eq. (61). For the purpose of the design rules, the temperature used in conjunction with the LMP to determine the rupture time was taken as a constant value at the calculated steady state temperature according to Eq. (49). This is because significant life fraction progression does not occur until temperatures in excess of 400°C. Using this, the change in life fraction for each discrete step of the calculation is

$$\Delta L_f = \left\{10^{\frac{LMP}{T_{SS}}-19}\right\}^{-1} \Delta t \tag{62}$$

where the Larson-Miller Parameter is calculated from Eq. (60) and the steady state temperature is calculated from Eq. (49).

7.2.2 Creep Rupture Mechanism Rules Calibration

Because of the complexity of the creep rupture mechanism and the subsequent design rule, several model calibrations needed to be conducted to establish an accurate representation of the time varying life fraction response. The first calibration constant needed is found in Eq. (54) where the room temperature stress was normalized to constant value. This value represents the room temperature stress at which stress relaxation initiation occurs at a plate temperature of 400°C. To calculate the normalization stress constant, a nonlinear fit of creep relaxation initiation times obtained from FE analyses was conducted. In particular the fitting was conducted on models of the square plates exposed to radially symmetric heat flux distributions. This yielded a calibration constant stress value of 0.84 MPa. It is important to note that if using standard units in the calculation of Eq. (54), the normalized stress constant should be implemented in units of Pascals. In order to determine the instantaneous creep response of the material, the equivalent power law creep parameters at burnthrough temperatures needs to be developed. In this research, steady state creep rates measured in the high temperature creep experiments discussed in Chapter 4 were used to develop the power law creep parameters according to

$$\dot{\varepsilon}_{ss} = G\sigma^h e^{-Q/RT} \tag{63}$$

Power law creep parameters were calculated using a non-linear regression analysis of the experimental high temperature steady state creep rates. Results of the analysis are seen in Table 14. It is important to note that the activation energy calculated for the high temperature creep

Table 14. High temperature effective power law creep model parameters.

Parameter	Value
G ($s^{-1}MPa^{-h}$)	$2.91x10^{11}$
h	1.53
Q_{HT} (kJ/mol)	103

mechanism is significantly different than that calculated for the creep strains at lower temperatures. This is expected as the creep mechanisms present at temperatures above 550°C is different than that at lower temperatures [36]. Additionally, Figure 76 contains experimentally measured steady state creep rate as a function of stress compared to the power law creep model. Experimental data seen in Figure 76 is grouped in 10°C increments. As discussed in Chapter 4, experimental temperature measurements were taken from IR images of the rupture site which resulted in experimental temperatures that varied from 500°C to 585°C depending on the target temperature and rupture location. Because of this, experimental temperatures were not identical between tests and similar test temperatures were grouped in Figure 76. Good agreement exists between experimentally obtained steady state creep rates and values obtained from the equivalent power law for stresses down to 1 MPa.

The second set of calibration parameters necessary to implement the creep rupture design equation is in the instantaneous stress response prediction in Eq. (59). As discussed in the previous section,

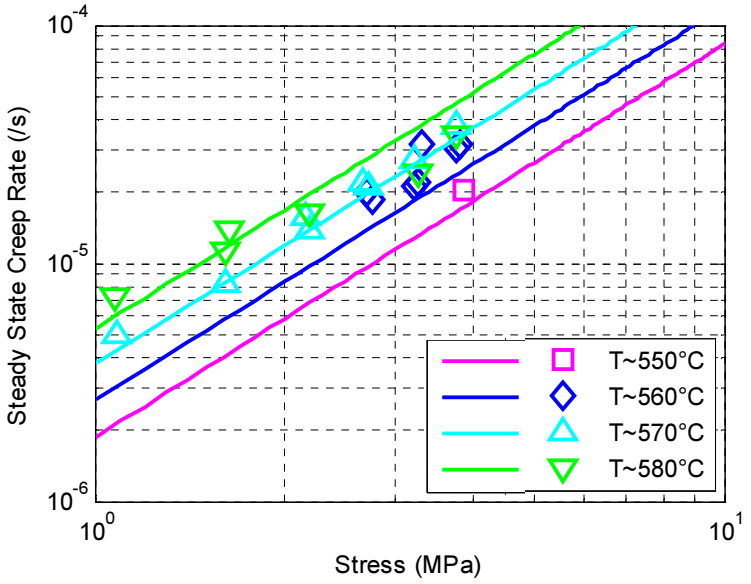

Figure 76. High temperature effective power law steady state creep model results compared to experimentally obtained data.

a constant calibration factor was added to account for the non-constant total strain at the burnthrough site. Additionally, a calibration factor to account for exposure radius effects was added to the stress relaxation equation. A limit analysis of the stress response was conducted to develop the form for the exposure radius calibration factor. Furthermore, the relaxation rate is inversely proportional to the exposure radius and the relaxation rate approaches negative infinity as the exposure diameter becomes small. All of these aspects led to the formulation of an inverse exponential decay calibration factor to account for the effects of exposure radius. To obtain the values for the fitting parameters, a non-linear regression analysis of the time varying stress response at the burnthrough site was conducted using data from all of the flat plate models under a radially symmetric heat flux. Inserting these results into Eq. (59) provided a final form for the creep relaxation response at the burnthrough site as

$$\sigma = \frac{\sigma_i}{\left[\frac{(0.084)Ge^{-Q/RT(h-1)\sigma_i^{h-1}}}{\left(1-e^{-0.257r_q^2}\right)}t+1\right]^{1/h-1}} \tag{64}$$

where r_q is in meters and the fitting parameter 0.084 is in units of MPa^h itself.

7.2.3 Creep Rupture Mechanism Rules Benchmarking

To benchmark the design equations for the creep rupture burnthrough mechanism, each intermediate variable was compared to the FE model results. First, Table 15 contains a comparison of room temperature stresses from Eq. (53) and results from a non-linear static FE analysis. This comparison is for square flat plate geometries with varying spans and thicknesses. For most geometries, the room temperature stress design equation under-predicts the results from the FE analysis by 10-20%. This was expected as Eq. (53) does not account for the effects of Poisson's ratio and, therefore, neglects any plane stress effects. The cases where Eq. (53) does not capture actual behavior is for span to thickness ratios above 500. At these dimensions non-linear geometric effects create relatively large membrane stresses which are not accounted for in the design equation.

Figure 77 contains a comparison of creep relaxation initiation times obtained from FE models and Eq. (54). It can be seen that for peak heat fluxes above 50 kW/m^2, the design equations generally capture the stress relaxation initiation time to within 15%. Below 50 kW/m^2, the design equation fails to capture the asymptotic behavior seen in the FE models. The calculation of steady state

Table 15. Room temperature plate stresses from non-linear FE models and design equations.

Span (m)	Thickness (mm)	Room Temperature Stress (Mpa)		Difference (%)
		Abaqus Model	Design Rule	
0.3	0.79	0.907	0.75	-17
	1.58	0.449	0.38	-16
	3.18	0.223	0.19	-16
	6.35	0.112	0.09	-17
0.61	0.79	2.033	3.11	53
	1.58	1.776	1.55	-13
	3.18	0.898	0.77	-14
	6.35	0.446	0.39	-13
0.91	0.79	3.312	6.92	109
	1.58	2.685	3.46	29
	3.18	2.037	1.72	-16
	6.35	1.007	0.86	-15

temperature at these relatively low heat fluxes according to Eq. (49) is below 500°C where. At temperatures this low, rupture times calculated from the Larson-Miller parameter are generally on the order of several hours to several days at the stresses observed at the burnthrough initiation site.

Figure 78 contains a comparison of the stress response of a 0.61 m wide and 3.18 mm thick plate exposed to uniform heat flux obtained from the FE models and Eqs. (54) and (64). The design equations capture both the creep relaxation initiation time and the creep relaxation rate for all of

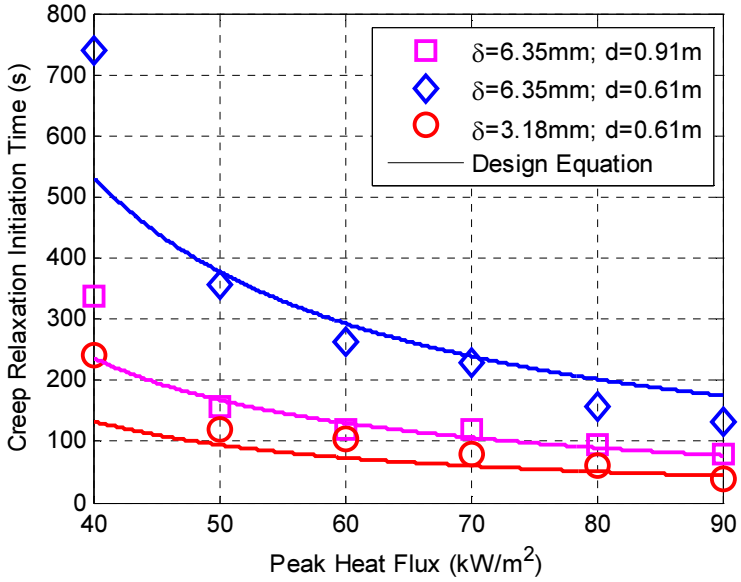

Figure 77. Creep relaxation initiation times obtained from FE models and developed design rules.

the uniform exposures. For each of exposures seen in Figure 78, the instantaneous stress state obtained from the design equations is within 30% of stresses obtained from the mechanical FE models. A comparison of the stress response under a 70 kW/m^2 peak flux with varying exposure radii is seen in Figure 79. As the exposure radius is decreased, the largest errors in the predicted stress response occur due to the errors in the predicted stress relaxation initiation time. Because the stress relaxation rate is high for smaller radii exposures, the error in the instantaneous stress response between the relaxation initiation time from the design equations and FE models briefly increases to nearly 90%. However, this error is only for a relatively short duration.

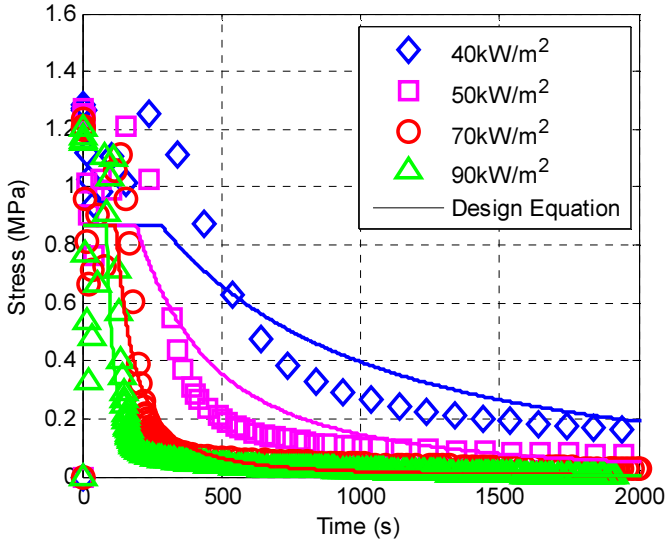

Figure 78. Burnthrough site stress relaxation response from FE model and design rules for multiple peak heat flux uniform exposures.

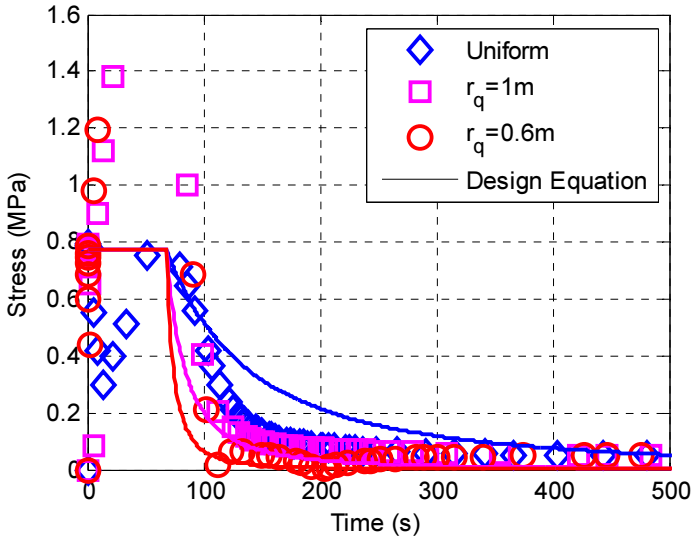

Figure 79. Burnthrough site stress relaxation response from FE model and design rules for 70 kW/m^2 exposure and multiple exposure radii.

A comparison of burnthrough times via the creep rupture mechanism for flat plates is shown in Figures 80 and 81. Rupture times obtained from the design equations are typically conservative up to 70% for all of the flat plate models used to develop the design equations. This under-prediction is generally higher for thicker plates than it is for thinner plate. The difference in rupture time between the FE models and design equations is primarily attributed to the use of the steady state temperature at all times beyond the creep relaxation initiation time. Inherently, the creep relaxation time was generally defined as the time for the burnthrough site to reach 400°C. Steady state temperature predictions at these exposures is generally between 550°C and 600°C. This creates a discrepancy in the calculated instantaneous rupture time between the creep relaxation initiation time and start of the thermal steady state region. For the FE models, the calculated instantaneous rupture time just after the creep relaxation initiation time is large because the temperature is still increasing towards steady state values. The design equations establish much shorter instantaneous creep rupture times during this region. As seen in Figure 80, this creates conservative rupture time predictions from the design equations. This under-prediction is larger for thicker plates because the thermal mass is larger and, thus, the time for the burnthrough site temperature to rise from 400°C to steady state is larger. Like the material melting design equations, the under-prediction of burnthrough times also results minimum peak heat fluxes and minimum exposure radii necessary to achieve burnthrough that are also conservative by 20-40%.

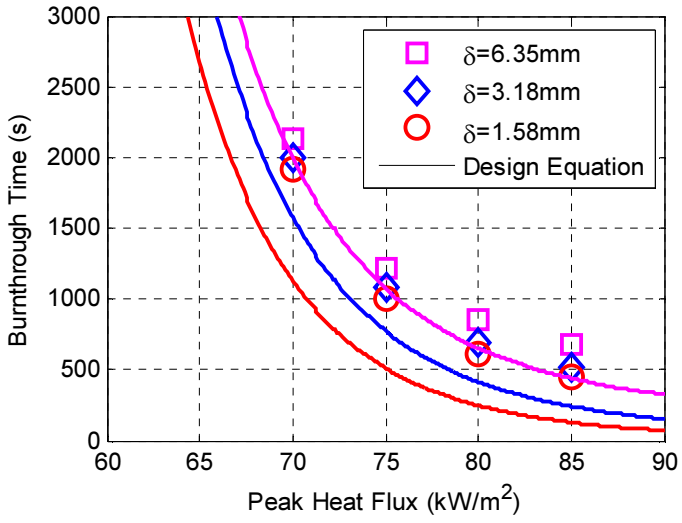

Figure 80. Burnthrough times via the creep rupture mechanism from FE simulation and design equations for multiple thickness plates under uniform exposure.

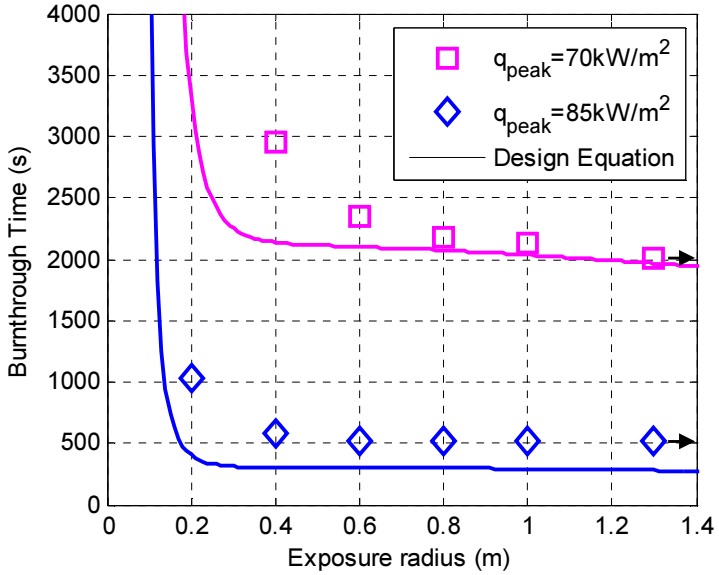

Figure 81. Burnthrough times via the creep rupture mechanism from FE simulation and design equations for 3.18 mm thick plate under multiple peak exposure fluxes and exposure radii.

Just like the melting mechanism model, the creep rupture mechanism model was used to predict the burnthrough times for the stiffened plate described at the beginning of this chapter. In order to achieve the creep rupture burnthrough mechanism, peak heat fluxes between 60 kW/m^2 and 80 kW/m^2 were modeled. Heat fluxes above 80 kW/m^2 resulted in the material melting mechanism occurring before the creep rupture mechanism while heat fluxes below 60 kW/m^2 did not result in burnthrough. The comparison of steady state temperatures at the burnthrough site were shown in Figure 72 in Section 7.1.2 for heat fluxes ranging from 50 kW/m^2 to 100 kW/m^2. As previously discussed, the presence of the stiffeners on the exposed side of the plate resulted in higher temperatures from the thermal FE models when compared to those obtained from the design equations. This resulted in unconservative burnthrough time predictions from the design equations as seen in Figure 82. Burnthrough times obtained from the design equations were generally 20-30% higher than those from the thermo-mechanical FE models. Likewise, the minimum heat flux to obtain burnthrough is also unconservative by 20-30%. Although not studied here, it is hypothesized that an exposure to the unstiffened side of the plate would result in predicted burnthrough times that are 20-30% lower than those developed through equivalent FE modeling. This degree of error generated by temperature errors of 10-15°C further reinforces the need for accurate thermal predictions to determine accurate burnthrough predictions. It also establishes

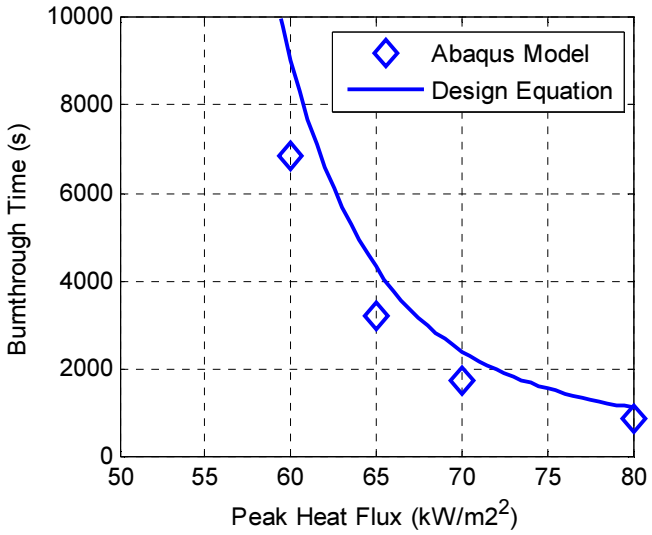

Figure 82. Burnthrough times via the creep rupture mechanism of the stiffened plate exposed to multiple peak heat flux exposures.

how sensitive the occurrence and time to burnthrough are to the temperature response of the burnthrough site.

Lastly, like the material melting mechanism design rules, predictions of burnthrough occurrence and time to burnthrough measured in the experiments discussed in Chapter 2 were conducted using the creep rupture mechanism design rules. The results of this comparison are seen in Table 16. Because the burnthrough site in all of the experiments exceeded 400°C, the creep rupture burnthrough design rules provided a predicted burnthrough time for all of the experiments including those where no burnthrough was observed. With the exception of the smaller exposures, the time to burnthrough calculated from the design rules was conservative by up to 65%. For experiments where burnthrough was not observed, design rule calculations were on the order of a few thousand seconds. Although this is conservative, it was expected that the design equations would provide a burnthrough time at temperatures below those seen in experiments since the design equations provide burnthrough times for all exposures where T_{ss} is above 400°C.

One benefit to the design equation is the ability to study how the two burnthrough mechanisms are effected by the physical and exposure parameters. In both the experimental and numerical research, it was seen that localized exposures (r_q<0.2 m) cause melting burnthrough while larger exposures (r_q>0.5 m) cause rupture burnthrough. Figure 83 contains burnthrough time predictions

Table 16. Comparison of experimentally measured burnthrough times with design equation results for experiments where burnthrough occurred via the creep rupture mechanism.

Thickness (mm)	HRR (kW)	Peak Heat Flux (kW/m²)	Exposure Radius (m)	Time to Rupture (s)	
				Experiment	Design Rule
0.79	70	62.3	0.61	NA*	6282
1.58	40	53.7	0.45	NA	1940
1.58	50	57	0.51	237	375
1.58	60	59.8	0.56	203	204
1.58	70	62.3	0.61	198	123
3.18	50	57	0.51	445	738
3.18	60	59.8	0.56	419	263
3.18	70	62.3	0.61	439	179
6.35	100	68.4	0.61	NA	1129
6.35	120	71.8	0.64	685	586
0.79	70	62.3	0.61	285	110

*Unexposed surface painted with high emissivity paint

from both burnthrough mechanisms for a 3.18 mm thick horizontally oriented plate under a uniform exposure and a localized exposure (r_q=0.1 m). Under the uniform exposure peak heat fluxes above 80kW/m2 cause a melting mechanism burnthrough prediction. However, below 80 kW/m^2 the rupture mechanism is predicted to occur within 2000 s for peak heat fluxes as low as 70 kW/m^2. This leaves an interval from 70 kW/m^2 to 80 kW/m^2 where the creep rupture mechanism is likely to occur. In contrast, the 0.1m exposure seen in Figure 83b causes a melting mechanism above 110 kW/m^2. This increase in required peak heat flux is due to thermal diffusion losses in the plate. More importantly, below 110 kW/m^2, it would require several thousands of

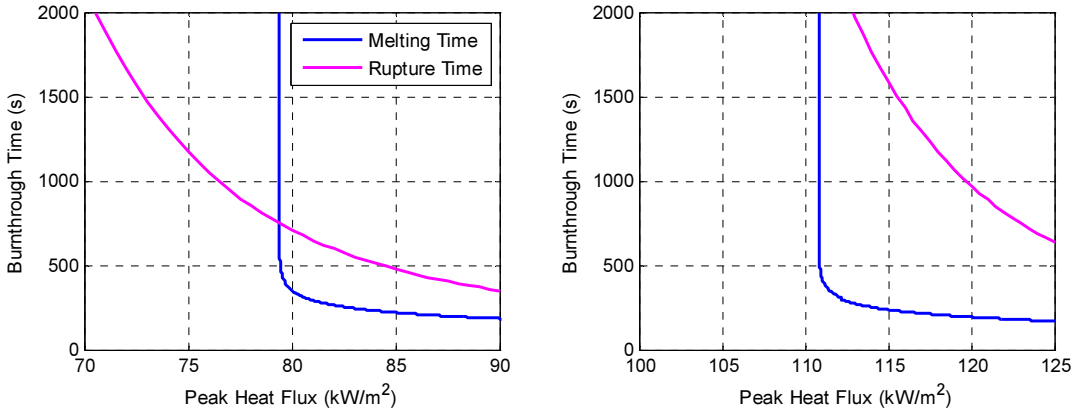

Figure 83. Burnthrough time predictions calculated from the melting and rupture mechanism design rules for multiple radius exposures

seconds for the rupture mechanism to occur which leave nearly no margin where the rupture mechanism can occur within a reasonable fire duration. This behavior is seen in the FE models as well as the experiments as seen in Figure 20 where the localized exposure of the propane jet burner did not cause burnthrough at temperatures in excess of 600°C for 2000 s of exposure.

7.3 Design Rules Conclusions

One motivation behind this research was the ability to implement a more accurate burnthrough model into commercially available fire modeling and structural modeling programs. Although the models developed in the previous chapter have a high fidelity, this comes at a high computation cost. To better implement the burnthrough mechanisms into larger scale models, analytical expressions were developed to calculate rupture times based on structure geometry and thermal exposure. Two separate analytical design rules were developed: first to capture the material melting mechanism and second to capture the material rupture mechanism. This models were developed and calibrated using FE models of flat AA6061-T651 plates with varying thickness and spans under to radially symmetric exposures of varying size and intensity. Once developed, these models were used predict rupture times via both mechanisms for flat and stiffened plates and results were compared to high degrees of freedom FE model results. Additionally, burnthrough time predictions for the experiments discussed in Chapter 2 were obtained and compared to observed values.

The design rule developed for the material melting mechanism utilized the same basic temperature threshold model of 633°C used in FE models. Analytical expressions for the time melting were developed using a lumped capacitance model for plates under a constant exposure. An exponential decay model was developed to account for thermal diffusion losses due to localized exposures. The expressions were calibrated for exposures with peak heat fluxes up to 105 kW/m^2. The developed expressions could predict burnthrough site steady state temperature to within 10°C for larger exposures and within 20°C for smaller exposures. Time to burnthrough via the material melting mechanism calculated from the design rules as generally within 25% of those obtained from FE models and experimental observations.

The design rule developed for the creep rupture mechanism uses the calculation of several intermediate variables. Analytical expressions were developed for the time dependent stress response of the burnthrough site. These expressions were calibrated against the flat plate models

with thickness between 0.79 mm and 6.35 mm and heat fluxes up to 85 kW/m^2. It was found that life fraction evolution did not occur until sufficient temperatures were achieved. Thus, the steady state temperatures calculated from the same equations as the material melting mechanism design rules were used in the creep rupture mechanism design rules. The creep rupture design rules were generally able to predict rupture time within 60% of values obtained from higher fidelity sources. Inaccuracies in both the predicted stress and thermal results contributed to errors in the predicted creep rupture times. Like the FE models discussed in the previous chapter, creep rupture times calculated from the design rules were found to be sensitive to the burnthrough site temperature predictions.

Chapter 8: Research Conclusions and Further Research

This research investigated the fire induced burnthrough of AA6061-T651 aluminum panels through both experimental and analytical methods. Burnthrough experiments were conducted using two different fire sources that produced two different heat flux profiles. The first was a pseudo-premixed propane jet burner that provided localized heat fluxes with high peak values. The second was a propane sand burner that produced larger heat fluxes with lower peak values. Experiments were conducted on plates with thickness ranging from 0.79 mm to 6.35 mm and supported in both and horizontal overhead position and a vertical bulkhead position. IR cameras and digital image correlation were used on select experiments to understand the effect of burnthrough site temperature and provide validation measurements for burnthrough models.

Under the localized exposure of the propane jet burner, temperature in excess of 625°C were necessary to achieve burnthrough and evidence of material melting was observed. Horizontally oriented plates exposed to the larger exposures of the propane sand burner were observed to burnthrough at temperatures as low as 550°C and no evidence of material melting was observed following burnthrough. This led to the development of two separate burnthrough mechanism models.

The first model developed to capture burnthrough predicted the material melting mechanism observed in the localized exposure experiments. This model utilized a simple temperature threshold of 633°C based on material property measurement. The second model developed captured the rupture model observed during the larger exposures. This model was based on the creep rupture behavior of the material at temperatures in excess of 550°C. Creep rupture times were modeled using a Larson-Miller parameter approach with variable stresses and temperatures handled through a Palmgren-Miner rule. This model required the characterization of the creep behavior at temperatures in excess of 550°C as well as a methodology for accurately predicting the thermal response of the material at the burnthrough site.

In order to implement the rupture model, a characterization of the creep rupture behavior of the material was conducted. Uniaxial tensile creep tests were conducted at temperatures ranging from 540°C to 590°C. Creep rupture data from these experiments was combined with literature values to develop a Larson-Miller curve that could capture creep ruptures at stresses ranging from 0.5

MPa up to 200 MPa. This could be used to predict creep ruptures both from burnthrough and larger physical loadings although the model has not been validated at temperatures below 550°C and stresses above 5 MPa. The secondary and tertiary creep response of the material was modeled using a modified Kachanov-Rabotnov creep model. This creep model included a hyperbolic-sine secondary creep rate model. The model was calibrated against creep rate and rupture data obtained from Allen [34]. Finally the creep model was implemented into the commercial finite element code Abaqus through a user CREEP routine.

To increase the accuracy of the thermal model, a small-scale full-field heat flux mapping technique was adapted for use in full-scale live fire experiments. This methodology utilizes an infrared camera to obtain full-field thermal measurements at spatial resolutions up to 1 mm at the scales used in this research. An inverse finite difference heat transfer analysis was used to obtain surface heat fluxes for each pixel of the thermograph. Results from the IR measurement were compared to traditional gauges and found to generally agree within one standard deviation. The primary source of error in the heat flux measurement was error in the estimated convective heat transfer coefficient on the exposed surface. This highlighted the need for more accurate full-field convective heat transfer coefficient data and models to increase the viability of the method. Spatially and temporally discrete heat flux maps generated using this method were implemented into Abaqus through a user FLUX routine. This allowed for integration of experimentally measured heat flux fields into the thermal finite element models used to predict burnthrough.

The models developed during this research for both the observed burnthrough mechanisms were implemented into sequentially coupled thermo-mechanical finite element models in Abaqus via user subroutines. Using full-field heat flux maps, temperature predictions were within 20°C of experimentally observed values for both the thermal transient and steady state regions of exposures from both the propane jet and sand burners. Additionally, deflection predictions from the finite element models were within 10% of experimentally observed values. Utilizing the two mechanisms, high degree of freedom finite element models were able to accurately capture burnthrough occurrence for nearly 95% of experimental conditions tested in this research. Additionally, burnthrough times via the material melting mechanism calculated from the finite element models were predicted within 30% of experimentally measured values. Burnthrough times were within 50% for the creep rupture mechanism. Larger dependencies on the fire heat

release rate were observed in the finite element models than in the burnthrough experiments. To further investigate this, additional experiments are needed utilizing larger diameter fires. Additionally, modeling suggested that plates exposed larger diameter fires are more susceptible to the rupture mechanism at lower temperatures. However, the facilities used during the research limited peak fire heat release rates to between 80 kW and 120 kW.

In order to implement the two burnthrough mechanism models into a design setting, simplified analytical expressions were developed for burnthrough via both of the modeled mechanisms. These design rules were calibrated using square flat plates under radially symmetric heat flux profiles. The material melting mechanism model was implemented into the design rules using the same temperature threshold of 633°C that was utilized in the finite element models. A lumped capacitance analysis was used to develop an expression for burnthrough site temperature. Using a linearization of the boundary conditions, an explicit expression for the time to burnthrough was developed. Losses due to thermal diffusion within the plate for localized exposures was handled through an exponential decay model. The temperature expression for the burnthrough site was able to calculate steady state temperatures within 15°C of finite element model results. Burnthrough times predicted by the design rules for the material melting mechanism were typically conservative by up to 25% compared to results from the finite element models of flat plates.

The expressions developed to capture the creep rupture burnthrough mechanism were more complex than the material melting mechanism. This is because the creep rupture mechanism is dependent on both the thermal and stress response of the burnthrough site. Using the finite element models, effects of plate span and thickness as well as the exposure size and intensity on the stress response was investigated. Using this, expressions for the time-dependent stress response were developed and compared to results from the finite element analysis. The developed expressions were modified from a constant strain creep relaxation model and predicted the stress response within 30% when compared to finite element model results. In modeling the thermal response, the progress towards a rupture state was neglected during much of the thermal transient region as uniaxial creep rupture times the low stresses observed at the burnthrough location are large at temperatures below 500°C. Combining the expressions for the stress and temperature response, burnthrough times via the creep rupture mechanism were predicted to within 50% compared to finite element results for flat plates.

The design rules were also used to predict rupture times via both mechanisms for a hypothetical stiffened plate and the experiments conducted during this research. For the stiffened plate, burnthrough times were less conservative by approximately 15% for the material melting mechanism and as much as 40% for the creep rupture mechanism. This is because the plate was modeled with the stiffened side exposed to the heat source and the presence of the stiffeners increased the temperature. It was expected that predictions from the design rules would be more conservative by similar values for exposures to the unstiffened surface as the presence of the stiffeners would decrease the plate temperature. Design rule predictions of the experimentally observed burnthrough times in this study were within 25% for the experiments where the material melting mechanism was observed. This is on the same order as errors from the finite element simulations suggesting that the design rules capture well the melting mechanism. Design rule results for the creep rupture mechanism were only within 60% of values observed during burnthrough experiments. This error is slightly higher than finite element models suggesting some loss in accuracy due to the simplifications made in the development of the design rules. However, the design rules still exhibit a higher sensitivity to fire heat release rate than observed in the experiments. Again, additional investigation is necessary utilizing thicker plates and larger fires to fully understand the effects of exposure size and intensity on experimentally measured burnthrough.

References

[1] A. International, “Standard E119-14: Standard Test Methods for Fire Tests of Building Construction and Materials.” 2014.

[2] F. Takahashi, A. Abbot, T. Murray, J. T’ien, and S. Olson, “Thermal Response Characteristics of Fire Blanket Materials,” *Fire Mater.*, vol. 38, pp. 609–638, 2014.

[3] M. Feng and Y. C. Wang, “An experimental study of loaded full-scale cold-formed thin-walled steel structural panels under fire conditions,” *Fire Saf. J.*, vol. 40, no. 1, pp. 43–63, Feb. 2005.

[4] I. M. Organization, “A.754(18) Recommendation on Fire Resistance Tests for ‘A’, ‘B’, and ‘F’ Class Divisions.” 1993.

[5] W. G. F. P. Association, “Ignition in Corrugations Ignition of Roof Covering,” *Fire Saf. J.*, vol. 10, pp. 149–154, 1986.

[6] I. D. Bennetts and K. M. Moinuddin, “Aspects of the Design of Fire-Resistant Plasterboard Walls in Fire,” *Electron. J. Struct. Eng.*, vol. 6, pp. 39–48, 2006.

[7] E. Johnsson and J. C. Yang, “Experimental study on tire fire penetration into a motorcoach,” *Fire Mater.*, vol. 38, pp. 63–76, 2014.

[8] H. Webster, G. Geyer, D. Do, J. Wright, and J. Collins, “Full-Scale Air Transport Category Fuelage Burnthrough Tests,” Washington, DC, 1990.

[9] T. R. Marker and C. P. Sarkos, “Full-Scale Test Evaluation of Aircraft Fuel Fire Burn-Through,” *SAMPE J.*, vol. 33, no. 4, pp. 32–39, 1997.

[10] K. D. Tran, “Burn-through Resistance of Fibre/Felt Materials for Aircrat Fuselage Insulation Blankets,” *Fire Mater.*, vol. 38, pp. 63–76, 2002.

[11] J. G. R. Hansen and B. J. Frame, “Flame penetration and burn testing of fire blanket materials,” *Fire an*, no. 32, pp. 457–483, 2008.

[12] B. Klein, “NIST Special Publication 1019-5 Fire Dynamics Simulator (Version 5) User ’ s Guide,” no. Version 5.

[13] K. Mcgrattan and H. Baum, “NIST Special Publication 1018-5 Fire Dynamics Simulator (Version 5) Technical Reference Guide,” no. Version 5.

[14] W. A. Bruce, H. D. Mishler, and J. F. Keifner, “Repair of Pipelines by Direct Deposition of Weld Metal,” 1993.

[15] W. A. Bruce, “Qualification of Procedures for Welding onto In-Service Pipelines,” in *Proceedings of the 4th International Pipeline Conference*, 2002.

[16] M. A. Saeimi-Sadigh, F. Vakili-Tahami, M. Zehsaz, and B. Behjat, “Study of the Burn-Through during In-Service Welding of T Joint Branch Connections,” in *Proceedings of the ASME 2010 10th Biennial Conference on Engineering Systems Design and Analysis*, 2010.

[17] R. D. Felix, W. A. Bruce, and P. L. Threadgill, “Development of Procedures for Hot Tap Welding ont Sour Service Pipelines,” in *Proceedings from the International Arctic Technology Conference*, 1991.

[18] A. H. Daei-Sorkhabi, M. A. Saeimi-Sadign, J. Vakili-Tahami, M. Zehsaz, and B. Behjat, “Study of the Burn-Through During In-Service Welding of T Joint Branch Connections,” in *Proceedings of the ASME 2010 10th Biennial Conference on Engineering Systems Design and Analysis*, 2014.

[19] W. Liu, T. Han, G. Guo, and G. Gu, “The Effect of Pressure on Burnthrough Susceptibility During In-Service Welding,” *Appl. Mech. Mater.*, vol. 121, pp. 2313–2317, 2012.

[20] A. S. Oddy and J. M. J. Mcdill, “Burnthrough Prediction in Pipeline Welding,” *Int. J. Fract.*, vol. 97, pp. 249–261, 1999.

[21] P. N. Sabapathy, M. a Wahab, and M. J. Painter, “Numerical methods to predict failure during the in-service welding of gas pipelines,” *J. Strain Anal. Eng. Des.*, vol. 36, no. 6, pp. 611–619, Jan. 2001.

[22] M. A. Boring, W. Zhang, and W. A. Bruce, “Improved Burnthrough Prediction Model for In-service Welding Applications,” in *Proceedings of International Pipeline Conference*, 2008, pp. 1–11.

[23] H. M. Als and A. Vatani, “Numerical Analysis of the Burn-Through at In-Service Welding of 316 Stainless Steel Pipeline,” *Int. J. Press. Vessel. Pip.*, pp. 49–59, 2013.

[24] M. A. Wahab, P. N. Sabapathy, and M. J. Painter, “The Onset of Pipewall Failure During ‘In-Service’ Welding of Gas Pipelines,” *J. Mater. Process. Technol.*, vol. 168, pp. 414–422, 2005.

[25] D. E. Sikoutris, D. E. Vlachos, V. Kostopoulos, S. Jagger, and S. Ledin, “Fire Burnthrough Response of CFRP Aerostructures. Numerical Investigation and Experimental Verification,” *Appl. Compos. Mater.*, vol. 19, no. 2, pp. 141–159, Feb. 2011.

[26] M. Sutton, W. Wolters, W. Peters, W. Ranson, and S. McNeill, “Determination of Displacements using an Improved Digital Correlation Method,” *Image Vis. Comput.*, vol. 1, no. 3, pp. 133–139, 1983.

[27] M. Riahi and H. Nazari, “Analysis of transient temperature and residual thermal stresses in friction stir welding of aluminum alloy 6061-T6 via numerical simulation,” *Int. J. Adv. Manuf. Technol.*, vol. 55, no. 1–4, pp. 143–152, 2011.

[28] E. Giraud, M. Suery, and M. Coret, “Mechanical behavior of AA6061 aluminum in the semisolid state obtained by partial melting and partial solidification,” *Metall. Mater. Trans. A Phys. Metall. Mater. Sci.*, vol. 41, no. 9, pp. 2257–2268, 2010.

[29] J. Bowyer, A. Luketa, W. Gill, and B. Donaldson, “Aluminum Behavior during Fire Heating : Focus on Deformation,” in *Fire Safety Science - Proceedings of the 10th International Symposium*, 2011, pp. 1151–1164.

[30] F. R. Larson and J. Miller, “A Time-Temperature Relationship for Rupture and Creep Stresses,” *Trans. ASME*, vol. 74, pp. 765–771, 1952.

[31] S. S. Manson and A. M. Haferd, “A Linear Time-Temperature Relationship for Extrapolation of Creep and Stress-Rupture Data,” 1953.

[32] O. D. Sherby and J. E. Dorn, “Creep Correlations in Alpha Solid Solutions of Aluminum,” *Trans. ASME*, vol. 194, 1952.

[33] J. G. Kaufman, *Properties of Aluminum Alloys*. Materials Park, OH, USA: ASM International, 1999.

[34] B. Allen, “Creep and Elevated Temperature Mechanical Properties of 5083 and 6061 Aluminum,” Virginia Polytechnic Institute and State University, 2012.

[35] P. T. Summers, B. Y. Lattimer, S. W. Case, R. L. West, and N. E. Dowling, “Microstructure-based Constitutive Models for Residual Mechanical Behavior of Aluminum Alloys after Fire Exposure,” Virginia Tech, 2014.

[36] H. Frost and M. Ashby, *Deformation-Mechanism Maps*. Elmsford, NY, USA: Pergamon PRess Inc., 1982.

[37] “E139-11: Standard Test Methods for Conducting Creep, Creep-Rupture, and Stress-Rupture Tests of Metallic Materials,” *ASTM Int.*, vol. 03, 2011.

[38] L. M. Kachanov, “Rupture time under creep conditions,” *Int. J. Fract.*, vol. 97, pp. 6–18, 1999.

[39] I. Rabotnov, *Creep Problems in Structural Members*. Amsterdam, Holland: North-Holland Publishing Company, 1969.

[40] J. Maljaars, F. Soetens, and L. Katgerman, “Constitutive Model for Aluminum Alloys Exposed to Fire Conditions,” *Metall. Mater. Trans. A*, vol. 39, no. 4, pp. 778–789, Feb. 2008.

[41] D. O. Hubble and T. E. Diller, “A Hybrid Method for Measuring Heat Flux,” *J. Heat Transfer*, vol. 132, no. 3, p. 031602, 2010.

[42] H. Ingason and U. Wickström, “Measuring incident radiant heat flux using the plate thermometer,” *Fire Saf. J.*, vol. 42, no. 2, pp. 161–166, Mar. 2007.

[43] E. Piccini, S. M. Guo, and T. V. Jones, “The development of a new direct-heat-flux gauge for heat-transfer facilities,” *Meas. Sci. Technol.*, vol. 11, pp. 342–349, 2000.

[44] U. Wickström, “Adiabatic Surface Temperature and the Plate Thermometer for Calculating Heat Transfer and Controlling Fire Resistance Furnaces,” in *Proceedings of the 9th Fire Safety Science Symposium*, 2009, pp. 1227–1238.

[45] M. Monde, H. Arima, and Y. Mitsutake, “Estimation of Surface Temperature and Heat Flux Using Inverse Solution for One-Dimensional Heat Conduction,” *J. Heat Transfer*, vol. 125, no. 2, pp. 213–223, 2003.

[46] H. Molavi, R. K. Rahmani, A. Pourshaghaghy, E. S. Tashnizi, and A. Hakkaki-Fard, “Heat Flux Estimation in a Nonlinear Inverse Heat Conduction Problem With Moving Boundary,” *J. Heat Transfer*, vol. 132, no. 8, p. 081301, 2010.

[47] W. Liu and K. Takase, “Development of measurement technology for surface heat fluxes and temperatures,” *Nucl. Eng. Des.*, vol. 249, pp. 166–171, Aug. 2012.

[48] J. I. Frankel, M. Keyhani, and B. E. Elkins, “Surface Heat Flux Prediction Through Physics-Based Calibration, Part 1: Theory,” *J. Thermophys. Heat Transf.*, vol. 27, no. 2, pp. 189–205, Apr. 2013.

[49] B. S. Elkins, M. Keyhani, and J. I. Frankel, “Surface Heat Flux Prediction Through Physics-Based Calibration, Part 2: Experimental Validation,” *J. Thermophys. Heat Transf.*, vol. 27, no. 2, pp. 206–216, Apr. 2013.

[50] B. Y. Lattimer and U. Sorathia, “Thermal characteristics of fires in a noncombustible corner,” *Fire Saf. J.*, vol. 38, no. 8, pp. 709–745, Dec. 2003.

[51] G. Back, C. L. Beyler, P. Dinenno, and P. Tatem, “Wall Incident Heat Flux Distributions Resulting from an Adjacent Fire,” in *Porceedings of the 4th International Symposium of Fire Safety Science*, 1994, pp. 241–252.

[52] Y. Hasemi, S. Yokobayashi, T. Wakamatsu, and A. Ptchelintsev, “Fire Safety of Building Components Exposed to a Localized Fire - Scope and Experiments on Ceiling/Beam System Exposed to a Localized Fire,” in *ASIAFLAM*, 1995.

[53] P. J. DiNenno (ed.), “SFPE Handbook of Fire Protection Engineering.” National Fire Protection Association, Quincy, MA, 2002.

[54] S. E. Dillon, “Analysis of the ISO 9705 Room/Corner Test: Simulations, Correlations, and Heat Flux Measurements,” University of Maryland, College Park, 1998.

[55] M. Švantner, P. Vacíková, and M. Honner, “IR thermography heat flux measurement in fire safety applications,” *Infrared Phys. Technol.*, vol. 55, no. 4, pp. 292–298, Jul. 2012.

[56] J. Stafford, E. Walsh, and V. Egan, “Characterizing convective heat transfer using infrared thermography and the heated-thin-foil technique,” *Meas. Sci. Technol.*, vol. 20, no. 10, p. 105401, Oct. 2009.

[57] J. Stafford, E. Walsh, and V. Egan, “The effect of global cross flows on the flow field and local heat transfer performance of miniature centrifugal fans,” *Int. J. Heat Mass Transf.*, vol. 55, no. 7–8, pp. 1970–1985, Mar. 2012.

[58] G. M. Carlomagno and G. Cardone, *Infrared thermography for convective heat transfer measurements*, vol. 49, no. 6. 2010.

[59] T. S. O’Donovan, T. Persoons, and D. B. Murray, “High-resolution hot-film measurement of surface heat flux to an impinging jet,” *Meas. Sci. Technol.*, vol. 22, no. 10, p. 105402, Oct. 2011.

[60] S. L. Brown, M. A. Pierson, B. Y. Lattimer, and S. V Ekkad, “Hydrodynamics and Transient Heat Transfer Characteristics in Fluidized and Spouted Beds,” Virginia Polytechnic Institute and State University, 2012.

[61] E. M. Sparrow, R. J. Goldstein, and D. C. Jones, “Natural Convection Mass Transfer Adjacent to Horizontal Plates,” *Int. J. Heat Mass Transf.*, vol. 16, pp. 1025–1035, 1973.

[62] S. W. Churchill and H. H. S. Chu, “Correlating equations for laminar and turbulent free convection from a vertical plate,” *Int. J. Heat Mass Transf.*, vol. 18, no. 11, pp. 1323–1329, Nov. 1975.

[63] H. H. Ku, “Notes on the Use of Propagation of Error Formulas,” *J. Res. Natl. Bur. Stand. - C. Eng. Instrum.*, vol. 70C, no. 4, pp. 263–273, 1966.

[64] H. Nakamura, “Frequency response and spatial resolution of a thin foil for heat transfer measurements using infrared thermography,” *Int. J. Heat Mass Transf.*, vol. 52, no. 21–22, pp. 5040–5045, Oct. 2009.

[65] P. S. Veloo and J. G. Quintiere, “Convective heat transfer coefficient in compartment fires,” *J. Fire Sci.*, vol. 31, no. 5, pp. 410–423, Mar. 2013.

[66] R. Wasson, T. E. Diller, B. Y. Lattimer, and S. T. Huxtable, “Separation of the Heat Transfer Components from Diffusion Flames Impinging onto Ceilings,” Virginia Tech, 2014.

[67] L. Y. Cooper, “Heat Transfer From a Buoyant Plume to an Unconfined Ceiling,” *Trans. ASME*, vol. 104, pp. 446–451, 1982.

[68] G. Heskestad, “Luminous heights of turbulent diffusion flames,” *Fire Saf. J.*, vol. 5, no. 2, pp. 103–108, 1983.

[69] S. Rainieri and G. Pagliarini, “Data filtering applied to infrared thermographic measurements intended for the estimation of local heat transfer coefficient,” *Exp. Therm. Fluid Sci.*, vol. 26, no. 2–4, pp. 109–114, Jun. 2002.

[70] S. Rainieri, F. Bozzoli, and G. Pagliarini, “Wiener filtering technique applied to thermographic data reduction intended for the estimation of plate fins performance,” *Exp. Therm. Fluid Sci.*, vol. 28, no. 2–3, pp. 179–183, Jan. 2004.

[71] *Properties and Selection: Nonferrous Alloys and Special-Purpose Materials*, 10th ed., vol. 2. 1990.

[72] H. M. Westergaard, *Theory of Elasticity and Plasticity*. Cambridge, MA: Harvard University Press, 1952.

[73] “No Title.” [Online]. Available: http://img.nauticexpo.com/images_ne/photo-g/rapid-car-ferry-catamaran-27117-213281.jpg. [Accessed: 05-Aug-2015].

[74] *Steel Constuction Manual*. American Institute of Steel Construction, 2011.

Appendix A: Abaqus User-Subroutines

This appendix contains each of the user-subroutines implemented into the Abaqus framework for this research. All of the Abaqus models and subsequent subroutines utilize the basic unit convention shown in Table A1. All other parameter units were derived from these basic parameter units. For example, this resulted in stresses being defined in terms of Mg/m^2 or kPa and heat fluxes defined in kW/m^2.

Table A1: Basic parameter unit convention utilized in Abaqus models and subroutines

Parameter	Units
time	s
length	m
mass	Mg
Temperature	°C

A.1 USDFLD routine

The following user sub-routine was used to calculate and track the progression of the material life fraction as calculated by Eq (18). This sub-routine will only calculate the life fraction evolution for temperatures above 450°C and stresses below 350 MPa. In order to calculate the life fraction evolution, this subroutine calls out the integration point temperature and von Mises stress values via the Abaqus utility routines.

The subroutine calculates values for 3 separate user state variables for display in post-processing software:

1. STATEV(1): current integration point life fraction. This begins at a value of zero and progresses to a value of 0.995 where it is limited to prevent model instability as it approaches a value of 1.
2. STATEV(2): creep rupture burnthrough state of the current integration point. 0 represents no creep rupture. 1 represents creep rupture.
3. STATEV(3): material melting burnthrough state of the current integration point. 0 represents no material melting. 1 represents material melting

```
      SUBROUTINE USDFLD(FIELD,STATEV,PNEWDT,DIRECT,T,CELENT,
     1 TIME,DTIME,CMNAME,ORNAME,NFIELD,NSTATV,NOEL,NPT,LAYER,
     2 KSPT,KSTEP,KINC,NDI,NSHR,COORD,JMAC,JMATYP,MATLAYO,
```

```
     3 LACCFLA)
C
      INCLUDE 'ABA_PARAM.INC'
C
      CHARACTER*80 CMNAME,ORNAME
      CHARACTER*3  FLGRAY(15)
      DIMENSION FIELD(NFIELD),STATEV(NSTATV),DIRECT(3,3),
     1 T(3,3),TIME(2)
      DIMENSION ARRAY(15),JARRAY(15),JMAC(*),JMATYP(*),COORD(*)
      DOUBLE PRECISION :: TEMP,MISES,SP1,SP3,C1,C2,C3,C4,C5,CONST
C
C  SUBROUTINE WILL UPDATE THE LIFE FRACTION FOR CALCULATION
C  OF THE INSTANTANEOUS CREEP RATE AND RUPTURE LIFE.  SUBROUTINE
C  WILL ALSO UPDATE THE BURNTHROUGH STATUS VARIABLE AND SUBSEQUENT
C  FIELD VARIABLE FOR CONTROLLING MATERIAL PROPERTIES IN
C  BURNED-THROUGH ELEMENTS
C
C  DETERMINE IF ELEMENT IS ALREADY IN BURNTHROUGH STATE (IF SO THE
C  CALCULATION OF THE DAMAGE PARAMETER WILL BE SKIPPED)
C      IF(STATEV(2).GE.1.0) GO TO 10
C
C  CALL NECESSARY INFORMATION FROM MATERIAL POINTS
C
      CALL GETVRM('TEMP',ARRAY,JARRAY,FLGRAY,JRCD,JMAC,
     1 JMATYP,MATLAYO,LACCFLA)
      TEMP = ARRAY(1)
C
      CALL GETVRM('SINV',ARRAY,JARRAY,FLGRAY,JRCD,JMAC,
     1 JMATYP,MATLAYO,LACCFLA)
      MISES = ARRAY(1)
C
C
C  DETERMINE IF ELEMENT STRESS OR TEMPERATURE ARE LOW ENOUGH TO
C  NEGLECT LIFE FRACTION ADVANCEMENT
      IF (TEMP.LE.450.0) GO TO 10
      IF (MISES.GE.350000.0) GO TO 10
C
C  DEFINE MATERIAL PROPERTIES AS NOT BURNTHROUGH AS DEFAULT
    FIELD(1) = 0.0
C
C  CHECK FOR MATERIAL MELTING CRITERIA
      IF (TEMP.GE.632.8) THEN
        STATEV(3) = 1
        FIELD(1) = STATEV(3)
      END IF
C
```

```
C  DEFINE CONSTANTS FOR RUPTURE TIME CALCULATION
      C1 = -8.4868*(10**(2.0))
      C2 = -3.1372
      C3 = 2.489*(10**(-1.0))
      C4 = 5.453*(10**(-1.0))
      C5 = 1.2354*(10**(4.0))
      C6 = -0.3393
      C7 = 19564
C
      CONST = 19.0
C
C  CALCULATE RUPTURE TIME
C
C  CALCULATE LOW STRESS LMP
      LMP = C6*MISES+C7
C
C  CALCULATE HIGH STRESS LMP IF APPLICABLE
      IF (MISES.GE.2962) THEN
        OP = C2+C3*((MISES*(10**(-3.0)))**C4)
        SINHX = (EXP(OP)-EXP(-OP))/2.0
        LMP = C1*SINHX+C5
      END IF
C
      TRUP = 10**(LMP/(TEMP+273)-CONST)
C
C  CALCULATE LIFE FRACTION AND ADD TO EXISTING FRACTION
      STATEV(1) = STATEV(1)+DTIME/TRUP
C
C  COMPARE LIFE FRACTION TO CHECK FOR BURNTHROUGH CRITERIA
      IF(STATEV(1).GE.0.999) THEN
        STATEV(2) = 1
        FIELD(1) = STATEV(2)
      END IF
C
C  SKIP TO HERE IT TEMPERATURE AND STRESS REQUIREMENTS ARE NOT
C  MET FOR BURNTHROUGH CALCULATION
  10  CONTINUE
C
      RETURN
      END
```

A.2 CREEP routine

The following user sub-routine was used to model the secondary and tertiary creep behavior of the AA6061. The instantaneous creep strain increment is calculated according to Eq. (19) in Chapter 4. The creep calculation was implemented using and implicit solver that required the derivative of the creep strain increment with respect to stress and the current amount of creep strain. The stress derivative of the creep strain increment was calculated according to Eq. (20) while the current creep strain derivative was calculated according to Eq. (21).

```
      SUBROUTINE CREEP(DECRA,DESWA,STATEV,SERD,EC,ESW,P,QTILD,
     1 TEMP,DTEMP,PREDEF,DPRED,TIME,DTIME,CMNAME,LEXIMP,LEND,
     2 COORDS,NSTATV,NOEL,NPT,LAYER,KSPT,KSTEP,KINC)
C
      INCLUDE 'ABA_PARAM.INC'
C
      CHARACTER*80 CMNAME
      CHARACTER*3 FLGRAY(15)
      DIMENSION DECRA(5),DESWA(5),STATEV(*),PREDEF(*),DPRED(*),
     1 TIME(2),COORDS(*),EC(2),ESW(2)
      DIMENSION ARRAY(15),JARRAY(15)
      DOUBLE PRECISION :: F,A,B,N,QOVERR,LAMDA,C1,C2,C3,C4,C5,
     1 C6,C7,CONST,SINHBS,DECRSS,LMP,OP,SINHX,TRUP
C
C  SUBROUTINE WILL CALCULATE THE INSTANTANEOUS CREEP STRAIN RATE
C     BASED ON A MODIFIED KACHANOV-RABOTNOV FORM TO INCLUDE
HYPERBOLIC
C  SINUSOIDAL STEADY STATE CREEP STRAIN RATES. RUPTURE TIMES ARE
C  CALCULATED BASED ON THE LARSON-MILLER PARAMTER WITH CONSTANT
C  VALUES CALCULATED THROUGH FITS OF UNIAXIAL TENSILE CREEP TESTS.
C
C  DETERMINE IF ELEMENT TEMPERATURE IS LOW ENOUGH TO IGNORE CREEP
C  STRAIN FOR THIS INCREMENT
      IF(TEMP.LE.150.0) GO TO 10
C
C  DEFINE CONSTANTS FOR STEADY STATE CREEP RATE CALCULATION
      F = STATEV(1)
      A = 2.9784*(10**(11.0))
      B = 0.02825
      N = 2.5003
      QOVERR = 2.5574*(10**(4.0))
      LAMDA = 1.774*(10**(1.0))
C
C  CALCULATE STEADY STATE CREEP RATE VALUE
      SINHBS = (EXP(B*QTILD*(10**-3.0))-EXP(-B*QTILD*(10**-3.0)))/2.0
```

```
      COSHBS = (EXP(B*QTILD*(10**-3.0))+EXP(-B*QTILD*(10**-3.0)))/2.0
      DECRSS = A*(SINHBS**N)*EXP(-QOVERR/(TEMP+273.0))
C
C  DEFINE CONSTANTS FOR INSTANTANEOUS CREEP INCREMENT CALCULATION
      C1 = -8.4868*(10**(2.0))
      C2 = -3.1372
      C3 = 2.489*(10**(-1.0))
      C4 = 5.453*(10**(-1.0))
      C5 = 1.2354*(10**(4.0))
      C6 = -0.3393
      C7 = 19564
C
      CONST = 19.0
C
C  CALCULATE RUPTURE TIME BASED ON LARSON-MILLER PARAMETER
C
      LMP = C6*MISES+C7
      IF (MISES.GE.2962) THEN
        OP = C2+C3*((QTILD*(10**(-3.0)))**C4)
        SINHX = (EXP(OP)-EXP(-OP))/2.0
        LMP = C1*SINHX+C5
      END IF
C
      TRUP = 10**(LMP/(TEMP+273)-CONST)
C
C  LIMIT LIFE FRACTION TO PREVENT INFINITE STRAIN INCREMENT
      IF (F.GE.0.999) THEN
        F = 0.999
      END IF
C
C  ASSIGN CURRENT STRAIN INCREMENT AS WELL AS STRESS
C  AND STRAIN DERIVATIVES
      DECRA(1) = DECRSS*DTIME*(1.0-F)**((1.0/LAMDA)-1.0)
      DECRA(2) = A*B*COSHBX**N*EXP(-QOVERR/(TEMP+273.0))
      DECRA(3) = DTIME/TRUP*(1.0/LAMDA-1.0)*(1.0-F)**((1/LAMDA)-2.0)
     1 *(1-EC(1)/(DECRSS*TRUP*LAMDA))**(LAMDA-1.0)
C
C  CONTINUE HERE IF TEMPERATURE TOO LOW
   10 CONTINUE
      RETURN
      END
```

A.3 FLUX routine

The following Abaqus user sub-routine was used to apply discrete full-field heat flux maps to numerical thermal models. Heat flux maps were generated using IR thermography as discussed in Chapter 5. This sub-routine requires an administrative variables file that contains the following:

1. physical size of the heat flux map in meters
2. the in-plane pixel resolution of the map in pixels
3. the total number of heat flux maps
4. current time of each heat flux map in seconds
5. directory information of heat flux map location

The administrative variables file should be placed in the same directory as the user-subroutine and its absolute directory must be specified within the sub-routine. Additionally, this subroutine requires heat flux map files as specified in the administrative variables files. Heat flux map files should contain only heat flux data with no administrative header.

```
      SUBROUTINE DFLUX(FLUX,SOL,KSTEP,KINC,TIME,NOEL,NPT,COORDS,
     1 JLTYP,TEMP,PRESS,SNAME)
C
C     ALLOCATE SPACE FOR VARIABLES
      INCLUDE 'ABA_PARAM.INC'
C
      DIMENSION FLUX(2), TIME(2), COORDS(3)
      REAL :: PSIZE(2), IND, TRIGGER, P, N, M, X, Z
      REAL :: VFLUX(2), FIELD(4), SPACE(4)
      INTEGER :: PIXELS(2), TSTEP
      REAL, DIMENSION(:), ALLOCATABLE :: TDATA
      REAL, DIMENSION(:,:), ALLOCATABLE :: FARRAY
      CHARACTER*80, DIMENSION(:), ALLOCATABLE :: FLNME
      CHARACTER*80 SNAME
C
C     OPEN ADMINISTRATIVE VARIABLE FILE AND READ NECESSARY
C     INFORMATION BASED ON CURRENT INCREMENT TIME
      OPEN(11,FILE="C:\ActiveDirectory\ADVAR.TXT",
     1 STATUS="OLD",ACTION="READ")
      READ(11,*), PSIZE(1), PSIZE(2)
      READ(11,*), PIXELS(1), PIXELS(2)
      READ(11,*), TSTEP
      ALLOCATE(TDATA(TSTEP))
      ALLOCATE(FLNME(TSTEP))
```

```
      ALLOCATE(FARRAY(1:PIXELS(1),1:PIXELS(2)))
      READ(11,*), TDATA
      READ(11,*), FLNME
      CLOSE(11)
C
C     CALCULATE WHICH HEAT FLUX MAP TO USE BASED ON INCREMENT
C     TIME AND HEAT FLUX MAP TIMES
      P = 0
      IND = 0
      DO WHILE (P.LT.1)
        IF (MOD(TIME(1),TDATA(TSTEP)).GT.TDATA(TSTEP-IND-1)) THEN
          P = TSTEP-IND-1
        END IF
        IND = IND+1
      END DO
C
C     OPEN HEAT FLUX MAP AND IMPORT MAP VALUES
      OPEN(12,FILE=FLNME(P),STATUS="OLD",ACTION="READ")
      DO IND = 1,PIXELS(1),1
        READ(12,*), FARRAY(IND,1:PIXELS(2))
      END DO
      CLOSE(12)
C
C     CALCULATE NEAREST HEAT FLUX MEASUREMENT ABOVE CURRENT NODE
      N = 0
      IND = 0
      DO WHILE (N.LT.1)
        CHECK = IND*PSIZE(1)/(PIXELS(2)-1)-PSIZE(1)/2
C         PRINT*, "LOOP 1 TEST"
        IF (COORDS(1).LE.CHECK) THEN
          N = IND
        END IF
        IF (IND.GE.PIXELS(2)) THEN
          N = IND-1
        END IF
        IND = IND+1
      END DO
C
C     CALCULATE NEAREST HEAT FLUX MEASURMENT LEFT OF CURRENT NODE
      M = 0
      IND = 0
      DO WHILE (M.LT.1)
        CHECK = IND*PSIZE(2)/(PIXELS(1)-1)-PSIZE(2)/2
C         PRINT*, "LOOP 2 TEST"
        IF (COORDS(3).LE.CHECK) THEN
          M = IND
```

```
        END IF
        IF (IND.GE.PIXELS(1)) THEN
          M = IND-1
        END IF
        IND = IND+1

      END DO
C
C     READ NEAREST HEAT FLUX MEASUREMENT VALUES AND LOCATIONS
      FIELD(1)=FARRAY(M,N)
      FIELD(2)=FARRAY(M,N+1)
      FIELD(3)=FARRAY(M+1,N)
      FIELD(4)=FARRAY(M+1,N+1)
      SPACE(1)=(M-1)*PSIZE(2)/(PIXELS(1)-1)-PSIZE(2)/2
      SPACE(2)=(M)*PSIZE(2)/(PIXELS(1)-1)-PSIZE(2)/2
      SPACE(3)=(N-1)*PSIZE(1)/(PIXELS(2)-1)-PSIZE(1)/2
      SPACE(4)=(N)*PSIZE(1)/(PIXELS(2)-1)-PSIZE(1)/2
C
C     CALCULATE HORIZONTAL AND VERTICAL INTERPOLATION
C     FRACTIONS
      X=(SPACE(4)-COORDS(1))/(SPACE(4)-SPACE(3))
      Z=(SPACE(2)-COORDS(3))/(SPACE(2)-SPACE(1))
C     CHECK IF CURRENT NODE IS OUTSIDE OF HEAT FLUX MAP
C     GEOMETRY
      IF (X.LT.0) X = 0
      IF (Z.LT.0) Z = 0
      IF (X.GT.1) X = 1
      IF (Z.GT.1) Z = 1
      X = 1-X
      Z = 1-Z
C     CALCULATE HORIZONTALLY INTERPOLATED HEAT FLUX VALUES
      VFLUX(1)=X*(FIELD(2)-FIELD(1))+FIELD(1)
      VFLUX(2)=X*(FIELD(4)-FIELD(3))+FIELD(3)
C
C     CALCULATE VERTICALLY INTERPOLATED HEAT FLUX VALUE
      FLUX(1)=Z*(VFLUX(2)-VFLUX(1))+VFLUX(1)
C     CHANGE IN HEAT FLUX WITH TEMPERATURE IS 0 FOR DESCRETE
C     MEASUREMENT APPLICATION
          FLUX(2) = 0

      RETURN
      END
```

Appendix B: Creep Rupture Time Data

The below table contains experimentally measured creep rupture times for AA6061-T651 at temperatures above 500°C and below stresses of 5.5MPa. These rupture times were used in conjunction with data from Kaufman [33] and Allen [34] to develop the Larson-Miller curve for predicting creep rupture time in the rupture burnthrough model and the modified Kachanov-Rabotnov creep model.

Table A2. Creep rupture time results for temperatures above 500°C and stresses below 5.5MPa

Temperature (°C)	Stress (MPa)	Rupture Time (s)		Temperature (°C)	Stress (MPa)	Rupture Time (s)
500	5.5	4048		577	1.6	3120
510	4.9	4947		573	1.1	7920
520	4.3	4703		577	2.2	2310
530	3.8	4553		572	2.7	2700
510	5.4	2953		580	3.3	1180
520	5.4	1947		572	3.7	1220
500	4.8	6032		573	3.7	1330
510	4.3	4880		573	3.2	2090
500	5.4	5494		580	0.5	11960
510	4.9	5006		559	3.8	2450
520	4.3	5056		561	3.2	3990
530	3.8	3422		560	2.8	5080
538	3.8	6480		552	3.7	3750
556	3.3	4210		567	2.2	4360
556	3.3	5560		568	1.6	8180
565	2.7	3250		576	1.6	5160
563	2.7	4950		578	1.1	6340
571	2.2	3620				

Appendix C: Permissions

Draft 09/01/2009

(Questions? Concerns? Contact Gail McMillan, Director of the Digital Library and Archives at Virginia Tech's University Libraries: gailmac@vt.edu)

(Please ensure that Javascript is enabled on your browser before using this tool.)

Virginia Tech ETD Fair Use Analysis Results

This is not a replacement for professional legal advice but an effort to assist you in making a sound decision.

Name: Christian Rippe

Description of item under review for fair use: Figure 1. Modern high speed vessel constructed using aluminum hull and superstructure [1].

Report generated on: 08-05-2015 at : 11:12:16

Based on the information you provided:

Factor 1

Your consideration of the purpose and character of your use of the copyright work weighs: ***in favor of fair use***

Factor 2

Your consideration of the nature of the copyrighted work you used weighs: ***in favor of fair use***

Factor 3

Your consideration of the amount and substantiality of your use of the copyrighted work weighs: ***in favor of fair use***

Factor 4

Your consideration of the effect or potential effect on the market after your use of the copyrighted work weighs: ***in favor of fair use***

Based on the information you provided, your use of the copyrighted work weighs: *in favor of fair use*